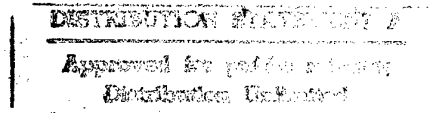


0207

INTERACTION OF REGIONAL AND TELESEISMIC WAVES WITH 3-D EARTH STRUCTURE

Brian L.N. Kennett

Australian National University
Research School of Earth Sciences
Canberra ACT 0200
AUSTRALIA



1997 April 16

Final Technical Report
Grant AFOSR-F49620-94-1-0022

1995 November 15 - 1997 April 14

AFSC
and is
-12

Approved for public release.

REPORT DOCUMENTATION PAGE

Form Approved
OMB No. 0704-0188

Public reporting burden for this collection of information is estimated to average 1 hour per response, including the time for reviewing instructions, searching existing data sources, gathering and maintaining the data needed, and completing and reviewing the collection of information. Send comments regarding this burden estimate or any other aspect of this collection of information, including suggestions for reducing this burden, to Washington Headquarters Services, Directorate for Information Operations and Reports, 1215 Jefferson Davis Highway, Suite 1204, Arlington, VA 22202-4302, and to the Office of Management and Budget, Paperwork Reduction Project (0704-0188), Washington, DC 20503.

1. AGENCY USE ONLY (Leave blank) 2. REPORT DATE 1997 April 16 3. REPORT TYPE AND DATES COVERED Final Technical Report 1995 Nov 15-1997 Apr 14

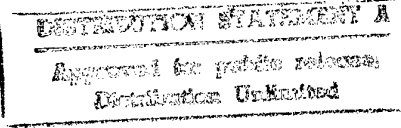
4. TITLE AND SUBTITLE Interaction of regional and teleseismic waves with 3-D earth structure 5. FUNDING NUMBERS

6. AUTHOR(S) B.L.N. Kennett

7. PERFORMING ORGANIZATION NAME(S) AND ADDRESS(ES) Research School of Earth Sciences Australian National University Canberra ACT 0200 Australia 8. PERFORMING ORGANIZATION REPORT NUMBER

9. SPONSORING/MONITORING AGENCY NAME(S) AND ADDRESS(ES) AFOSR/NL, 110 Duncan Avenue Suite B115, Bolling AFB DC 20332-0001 10. SPONSORING/MONITORING AGENCY REPORT NUMBER

11. SUPPLEMENTARY NOTES

12a. DISTRIBUTION/AVAILABILITY STATEMENT 12b. DISTRIBUTION CODE


13. ABSTRACT (Maximum 200 words)

This report describes a range of studies which have been directed at improved delineation of structure at regional scales which can be used in calibrating seismic information from regional or teleseismic sources.

The first two sections describe the development of fine-scale three-dimensional models for the crust and lithosphere incorporating a broad class of seismic information and the extension of such procedures to include anisotropy. The next part develops a new theoretical approach which should allow direct computation of surface wave fields in 3-D models.

The final section presents a regionalized model for the upper mantle based on tectonic characteristics derived using teleseismic information which provides a representation of the upper mantle for the whole globe.

DTIC QUALITY INSPECTED 2

14. SUBJECT TERMS 15. NUMBER OF PAGES
 Seismic Waves, Earth Structure

16. PRICE CODE

17. SECURITY CLASSIFICATION OF REPORT 18. SECURITY CLASSIFICATION OF THIS PAGE 19. SECURITY CLASSIFICATION OF ABSTRACT 20. LIMITATION OF ABSTRACT

NSN 7540-01-280-5500

Standard Form 298 (Rev. 2-89)
Prescribed by ANSI Std. Z39-18
298-102

19970604 136

INTRODUCTION:

This final technical report comprises five sections representing different facets of work undertaken at the Research School of Earth Sciences, Australian National University on the problems of seismic wave propagation and inference about three-dimensional structure from regional to teleseismic scales.

Part I: Upper mantle beneath Australia from portable array deployments.

R. van der Hilst & B.L.N. Kennett

This contribution brings together the range of studies which have been made on the crustal and upper mantle structure beneath Australia exploiting portable station deployments, notably the SKIPPY array. A detailed three-dimensional model of shear wave speed has now been produced for two-thirds of the continent and the oceanic zone to the east, in less than four years from the commencement of field recording.

The integration of receiver based studies including P wave delay-time tomography and crustal receiver functions with the model derived from surface wave inversion provides an excellent characterisation of a continent. Such a representation can be used to calibrate both regional and teleseismic information.

Part II: Upper mantle heterogeneities in the Indian Ocean from waveform inversion.

E. Debayle & J.J. Lévêque

This section represents work begun at the University of Strasbourg in France and completed at the Australian National University. The application of joint inversion of Rayleigh and Love wave trains to extract information on both velocity heterogeneity and the pattern of upper mantle anisotropy is of particular interest in a continental setting. A comparable inversion is underway for the SKIPPY data across the Australian continent.

Part III: Guided waves in 3-dimensional structures

B.L.N. Kennett

Current treatments of surface wave propagation in three-dimensionally varying media depend on perturbation techniques. For 2-D models it is possible to make a full development which describes the evolution of the wavefield in terms of coupling between the surface wave modes of a reference model. The extension to 3-D models requires simultaneous consideration of mode-coupling and transfer between plane wave components so that phenomena such as surface wave refraction can be described. The theory is quite complex but for periods in the range 25-100 seconds should provide a suitable basis for a computational development using a limited number of modes.

Part IV: A regionalized upper-mantle (RUM) model.

O. Gudmundsson & M. Sambridge

Models of three-dimensional structure in the upper-mantle derived from conventional travel-time tomography have coverage restricted to the vicinity of seismic sources and receivers. However, we can extend the information by representing the major features around the globe using a relatively detailed tectonic regionalization and then undertaking an inversion for the best fitting upper mantle for each such tectonic class. The resulting model provides a means of estimating the properties of the upper mantle e.g. teleseismic residuals even in zones which have not yet been characterised. Such a procedure can therefore provide a first step towards the calibration of paths to compensate for three-dimensional structure in the process of event location.

Part I: Upper mantle beneath Australia from portable array deployments.

Upper mantle structure beneath Australia from portable array deployments

R.D. van der Hilst^{1,2} & B.L.N. Kennett¹

¹ *Research School of Earth Sciences, The Australian National University,
Canberra ACT 0200, Australia*

² *Department of Earth, Atmospheric & Planetary Sciences, Massachusetts Institute of Technology,
Rm 54-514, Cambridge MA 02139, USA*

SUMMARY

The distribution of earthquakes at regional distances around Australia is particularly favourable for these natural events to be used as probes into the seismic structure of the lithosphere and upper mantle. The distribution of permanent seismic stations is too sparse for detailed continent-wide seismic imaging and most information used in our studies has come from deployments of portable seismic recorders.

Such portable instruments were initially used in northern Australia to define the radial variations in P and S velocity and attenuation using a combination of short-period and broadband observations, and to investigate seismic anisotropy from shear-wave splitting observed in refracted S waves propagating through the upper mantle.

The whole Australian continent has now been covered in the SKIPPY experiment from 1993-1996 in which a sequence of deployments of up to 12 recorders at a time have been used to synthesise a continental scale array of broad-band instruments. The major objectives of this project are to delineate the three-dimensional structure of the Australian lithosphere and underlying mantle by tomographic inversions for lateral variations in seismic wavespeed and site specific studies to map crustal thickness (receiver functions) and seismic anisotropy (shear wave splitting).

Surface wave studies have begun to reveal the three-dimensional variations in shear wave structure beneath the continent by exploiting the records from

portable broadband stations. Dense data coverage enables the imaging of wavespeed variations on length scales of 250 km and larger beneath most of central and eastern Australia.

Results of the waveform inversion suggest that the eastern edge of the Proterozoic shields of central Australia is a complex three-dimensional surface which does not have a simple relation to the conventional Tasman Line marking the separation of Precambrian and Phanerozoic outcrop. In the shallow lithosphere (80 km depth) the most pronounced lateral contrast in seismic wave speed occurs significantly further east than the conventional Tasman Line. However, in northern Australia the eastern boundary of exposed Precambrian basement coincides with a transition from moderately high wavespeeds to fast wave propagation that is particularly prominent at a depth of about 140 km. At larger depth still (200 km) the wavespeed gradient seems to occur significantly further west (near the western margin of the Eromanga basin). Beneath most of eastern Australia the fast seismic 'lid' does not extend to depths larger than about 100 km, and there is a pronounced low velocity zone between about 100 and 200 km depth. The surface wave data do not indicate a slow wavespeed channel beneath central Australia. Instead, the fast lid extends to a depth of at least 250 km, and locally to depths in excess of 350 km. The north Australian craton is seismically well defined but does not seem to continue into the Kimberley block. In the shallow lithosphere, the region influenced by the late Palaeozoic Alice Springs orogeny (Amadeus basin and Musgrave block) is marked by significantly slower seismic wave propagation than the Proterozoic cratons to the north and south.

Analysis of data from individual stations has produced a set of shear velocity profiles for the crust and uppermost mantle beneath SKIPPY stations which provide a useful complement to the information at depth from the surface wave studies. The crust-mantle boundary is deep (38-44 km) and mostly transitional in character along the axis of the eastern fold belt, but is relatively sharp and shallower (30-36 km) near the boundary between Precambrian and Phanerozoic outcrop. Shear wave splitting results from the portable stations are beginning to reveal a complex pattern of seismic anisotropy that requires further analysis of both body and surface wave data.

1 INTRODUCTION

The surficial geology of the Australian continent is composed of an assemblage of crustal blocks that can be broadly grouped into the Precambrian western and central cratons and the Phanerozoic eastern province (figure 1A). Structural differences in the mantle beneath the Precambrian shield and eastern Australia have previously been inferred from limited observations of surface wave dispersion (cf. Muirhead & Drummond, 1991; Denham, 1991), and teleseismic travel-time residuals (Drummond et al., 1989). These results have been confirmed and extended in recent studies using deployments of portable broad-band instruments across the whole continent (the SKIPPY experiment, Van der Hilst et al., 1994), and it is now possible to derive three-dimensional models of the P and S wavespeeds beneath the Australasian region to depths of 400 km or more.

The extensive earthquake activity in the seismic belt that runs through Indonesia, New Guinea and its offshore islands, Vanuatu, Fiji and the Tonga-Kermadec zone provides a wide range of natural sources which can be used to constrain seismic structure in the lithosphere, asthenosphere, and the transition zone beneath. There is a rather limited number of high-quality, permanent seismological stations in Australia so that for high resolution studies of seismic structure these observatories need to be supplemented by the installation of portable recorders (figure 1B).

Building on the experience from array deployments in northern Australia the Research School of Earth Sciences (RSES) started in 1993 a nationwide observational seismology project, the SKIPPY experiment, which uses a sequence of array deployments to synthesise a continental scale array of broad-band instruments. Major objectives of this project are to exploit different classes of seismological data for the delineation of the three-dimensional structure of the Australian lithosphere and underlying mantle by tomographic inversions for lateral variations in seismic wavespeed and site specific studies to extract crustal information through the construction of receiver functions, and seismic anisotropy from analysis of shear wave splitting.

For instruments in northern Australia, refracted arrivals for both P and S waves from the upper mantle can be used to determine upper mantle structure. At greater distances from the sources multiple S arrivals and surface waves provide a powerful probe for three-dimensional structure using information on many crossing propagation paths. For this class of arrival the energy is largely directed horizontally and the waveforms are most sensitive to S wave velocities. The information from regional earthquakes can be supplemented with the arrival times for teleseismic waves in delay-time tomography for P arrivals where the paths through the mantle are relatively steep. In addition, information from distant events can be used to constrain crustal and upper mantle structure through the analysis of converted waves and reverberations.

The combination of many different classes of seismological information has begun to reveal the complex nature of lithospheric and mantle structure and to shed light on the way in which the Australian continent may have been assembled. In this paper we briefly

review results of the array experiments in northern Australia, from both short-period and broadband instruments, and present the latest results from the SKIPPY project for the continent as a whole.

2 P AND S VELOCITY PROFILES IN THE UPPER MANTLE

The events to the north of Australia provide a convenient set of energy sources for studies of the upper mantle and it has proved possible to constrain the major features of the mantle velocity profile as well as the attenuation distribution with depth for both P and S waves.

2.1 Short-period studies

Much of the information on mantle structure has come from deployments of portable instruments with short-period seismometers. Hales, Muirhead & Rynn (1980) carried out a travel time analysis for Indonesian earthquakes that occurred at a variety of depths and were recorded at a number of portable stations in northern Australia. The resulting model is rather complex with many small discontinuities and low velocity zones, which may reflect the mapping of three-dimensional structure into a one-dimensional profile. A subsequent re-interpretation by Leven (1985), using comparisons between observed and synthetic seismograms, leads to somewhat simplified structure but retains a prominent velocity contrast near 210 km depth.

In the period 1985-1987, RSES carried out a sequence of experiments using short-period vertical seismometers in northern Australia (figure 1B) to record the natural seismicity in the Indonesia/New Guinea region. Many of the results were summarised by Dey et al (1993) who present composite record sections of upper mantle arrivals that show significant variation in P wave velocity structure between paths for events along the Flores arc, studied by Bowman & Kennett (1991), and paths to events in New Guinea. The shallow structure has to be inferred, but the P velocity structure is well constrained from above the base of the lithosphere near 210 km down to below the 410 km discontinuity. The interpretation confirms the need for a P velocity contrast near 210 km depth. For S waves the corresponding record sections show a clear arrival associated with the lithosphere which cannot easily be traced beyond 2000 km but no branches associated with greater depth.

2.2 Broad-band studies

Modern broadband seismometers provide a faithful rendition of ground motion over a wide range of frequency and allow the full exploitation of both P and S body waves. A broadband sensor has been operated by RSES at the Warramunga array in Northern Australia since late in 1988 (station code WRA); this facility, was upgraded in 1994 by IRIS at a nearby site (WRAB). Over a period of years it has been possible to build up record sections covering the range of interest for the upper mantle by using events in

the Indonesia/New Guinea earthquake belt. The records from the permanent station have been augmented by portable broadband stations deployed at distances of up to 300 km from WRA. The surface conditions in this region are such that good results can be obtained for SV waves on radial component records after rotation to the great circle path: the high surface velocities lead to little contamination by converted P waves. This represents a considerable benefit over previous S wave studies of the upper mantle which have been restricted to SH waves (Gudmundsson, Kennett & Goody, 1994).

The SKIPPY experiment (Van der Hilst et al., 1994) has emplaced a number of portable broadband instruments in northern Australia at a suitable distance range to complement the observations at the Warramunga array. Figure 2 shows a composite record section covering the P and S wave components returned from the upper mantle for events in New Guinea recorded at SKIPPY stations in Queensland. This section has been constructed from unfiltered vertical component records from five shallow events and clearly displays the benefit of broadband recording. The onset of the S waves shows high frequency behaviour (greater than 1 Hz) out to 2000 km, but beyond this distance the S wave arrivals have a significantly lower frequency (0.2 Hz at 3000 km) and this is also seen for later arrivals at shorter distance. For P waves the loss of higher frequencies is less pronounced. An enlargement of the S wave arrivals for both the radial and tangential components is displayed in figure 3 using unfiltered broadband records.

The change in frequency content for S waves returned from greater depth has been analysed by Gudmundsson, Kennett & Goody (1994) to determine the attenuation structure with depth under northern Australia. The slope of the spectral ratio between P and S wave arrivals on the same record has been used to determine the differential attenuation between P and S. This differential information can be interpreted with a knowledge of the velocity structure and requires strong attenuation of S waves in the asthenosphere between 210 km and the 410 km. In a parallel analysis Kennett, Gudmundsson & Tong (1994) have used the composite record sections, together with the earlier information from the short period studies, to build velocity profiles for P and S. These velocity models have been refined by comparison of observed and synthetic seismograms including the influence of attenuation (figure 4). An advantage of this study is that both P and S velocity profiles are determined for the same events and so the P/S velocity ratio can be well determined, which is particularly useful for studies of mantle composition. The depth variation of the P/S velocity ratio is in good general agreement with the results for the shield areas of north America obtained by combining the P velocity profile of LeFevre & Helmberger (1989) with the S wave structure of Grand & Helmberger (1984).

Comparison of the radial and tangential components of the S wavefield at WRA indicates that for the arrivals from the upper mantle discontinuities there is a systematically earlier arrival on the SH component by more than a second. These indications of seismic anisotropy for the refracted S wave arrivals have been analysed by Tong, Gudmundsson & Kennett (1994) who have determined the direction of fast

propagation and time shift between the S components by correlation analysis. The nature of the observed anisotropy is such that it cannot be explained by structure local to the receivers. A level of anisotropy of the order of 1 percent in both the lithosphere and the asthenosphere beneath would explain the data quite well.

3 THREE-DIMENSIONAL STRUCTURE

The favourable position of the Australian continent relative to world seismicity can be exploited in a number of ways to obtain information on the three-dimensional seismic structure in the mantle. This can be done by means of tomographic techniques that rely on the number of high-quality crossing paths produced by many source-receiver pairs or by site specific studies that aim to define the subsurface structure beneath individual stations by minimizing the influence of structure elsewhere. These applications provide complimentary information about Earth's structure, which are being merged to obtain a more complete description of the Australian mantle.

The configuration of the seismicity around the Australian continent is very favourable for tomographic methods since with a suitable distribution of receivers a dense and even data coverage of the continent can be achieved. RSES has just completed a three and a half year field program to install some 60 portable broadband stations across the entire Australian continent (see figure 1B). This project uses a set of up to 12 portable instruments which occupy sites for at least 5 months at a time before being moved to a new location, so that a full continental array can be synthesised (van der Hilst et al 1994, Kennett & van der Hilst 1996). The mobility of the arrays have led to the name SKIPPY (nickname for kangaroo) for the whole project. The deployments commenced in May 1993 with 8 stations in Queensland and the coverage of the whole continent was completed at the end of September 1996. The data set from the SKIPPY stations is supplemented by records of suitable events from the permanent broadband stations. In addition to providing data from sites not occupied by SKIPPY stations, the records from the observatory instruments are important in constraining upper mantle structure from fundamental mode surface wave since at frequencies less than 10 mHz they are often of better quality than the records of the portable stations.

3.1 Surface wave studies

The records from the broadband stations have been used in a number of different studies. A major objective is the delineation of lithospheric and mantle structure using waveform tomography for the shear wave and surface wave portion of the seismogram. So far the analysis has been based on the partitioned waveform inversion technique introduced by Nolet (1990). A nonlinear optimisation is used to find a stratified model which gives the best fit to an observed seismogram, which should represent the average structure along the great circle between source and receiver. The assemblage of path averages are then used in a linear inversion to recover the three-dimensional shear wave

structure. The tomographic inversion of the linear constraints on the three-dimensional velocity structure uses a block structure of approximately equal area in latitude and longitude coupled into a set of mostly triangular basis functions in the vertical direction. Both model norm and gradient damping are used to achieve a balance between data fit and smoothness of the model. The details of the partitioned waveform inversion method are given by Nolet (1990), and its application to Australian data is presented by Zielhuis & Van der Hilst (1996).

The non-linear waveform technique assumes the independent propagation of individual modes along a great circle path. The neglect of inter-mode coupling may prevent the reliable imaging of deep mantle structure and we therefore restrict the present discussion to the upper mantle. Since we do not account for out-of-plane scattering we do not make use of high-frequency fundamental mode surface waves that are sensitive to large wavespeed variations in the shallow lithosphere (such as variations in crustal thickness).

The effective use of the non-linear inversion scheme for the individual paths requires synthetic seismograms that are close to the observed waveforms, and in turn this requires a reference model that is close to the averaged 1D velocity model for the wave path. Care has to be taken to account for the best averaged crustal model for the path in a region which covers both continental and oceanic lithosphere. A partial compensation for crustal thickness variations is made by using different mode files for source, propagation path, and receiver structure (Zielhuis & Nolet, 1994b, Kennett 1995). The influence of heterogeneity is rather different for the fundamental and higher modes. For instance, at frequencies higher than about 30 mHz the fundamental modes are sensitive to variations in crustal structure in general and the ocean-continent transition in particular. The higher modes are more sensitive to structure at larger depth and are less influenced by scattering due to strong heterogeneity in the shallow lithosphere and can thus be interpreted to higher frequency. The waveform matching was, therefore, restricted to frequencies of up to 25 mHz for the fundamental mode and 50 mHz for a time window comprising covering the range of phase velocities expected for the higher modes. The use of higher modes, which are well excited by the deep earthquakes in the region (Tonga, New Hebrides, Java), improves resolution of structure in depth. However, the influence of the heterogeneity in structure means that it is not always possible to fit both the fundamental mode and higher mode windows with the same structure. In future studies this linearization problem will be remedied by using wavespeed profiles and associated mode files of reference models that are constructed specifically for the region.

Zielhuis & Van der Hilst (1996) discussed results of the application of this partitioned waveform inversion scheme to the data from stations in eastern Australia (arrays SK1, SK2, and BAS, Figure 1B). These data are consistent with a pronounced change from slow shear wave propagation beneath the Coral and Tasman Seas and the coastal regions of continental Australia to very fast wave propagation beneath central Australia. The

thickness of the high wavespeed lid increases from about 80-100 km in easternmost Australia to at least 250 km beneath the central shields. The transition is rather sharp in north Queensland but is manifest as a multiple boundary further south. Based on these data Zielhuis & Van der Hilst argued that the conventional Tasman line (figure 1B) marking the limits of Precambrian outcrop, may roughly coincide with a contrast in seismic wave speed in the north, but that high wavespeed lithosphere extends east of the Precambrian basement further to the south. However, the data used in this earlier study does not constrain the southernmost part of the region around the Tasman Line, nor does it reliably image possible lateral variations in wavespeed in the upper mantle beneath central Australia.

The model presented here is based on waveform data from the permanent observatories in the region and from 45 SKIPPY stations covering the eastern and central parts of the Australian continent (arrays SK1,SK2,SK3,SK4 and BAS in Figure 1B). Low-noise records were selected for regional earthquakes for which a Centroid Moment Tensor (CMT) is available from Harvard University. The total number of seismograms used in the construction of the three-dimensional shear velocity mode is approximately 1350 from about 360 earthquakes. Good wave path coverage is achieved for eastern and central Australia as shown in figure 5 which enables the extension of the results for eastern Australia by Zielhuis & Van der Hilst (1996).

Results of the inversion for three-dimensional variations in shear wavespeed are presented in figure 6 for depths of 80, 140, 200 and 300 km. On wavelengths of 1000 km and larger the observations are in good agreement with inferences from global inversion of Rayleigh wave phase velocities (e.g., Trampert & Woodhouse 1995), but the data coverage provided by the SKIPPY arrays allows the study of continental structure in much more detail. The resolution length is about 300 km for most of the area discussed here.

A striking feature in the images of mantle structure to about 200 km depth is the large difference in shear wavespeed between the part of Australia east of 140°E and the rest of the continent (Figures 6A,B). The wavespeed gradients are predominantly in west-east direction and exhibit peak-to-peak amplitude variations of up to 10 per cent relative to the reference model used for the display. The patterns generally match geological trends observed at the surface. Beneath easternmost Australia and the adjacent oceanic regions the shear wave speed is relatively low, whereas fast wave propagation marks the central and western part of the continent. The boundary between these regions is well defined at 80 and 140 km depth. The transition from low to high velocities seems to be rather sharp in northern Queensland (near 15°S, 142°E) and lies close to the Tasman Line, the presumed eastern edge of the Precambrian shields based on geological outcrop, gravity and magnetic data (Figure 1B). Further to the south the transition from slower to faster wavespeeds appears to be somewhat more complex and may occur over at least two zones of rapid increase in wavespeed. The southern part of the Eromanga basin and the region associated with the Lachlan fold belt is characterized by wavespeeds that are

intermediate to that in the coastal regions and the central shields (figure 6B). The nature of these wavespeed transitions and, in particular, the complex wavespeed structure near the Broken Hill block (-32°S , 140°E) will be discussed in more detail in a separate paper (Kennett & Van der Hilst, in preparation). We remark that south of 130°S , the velocity contrast associated with the boundary between Phanerozoic and Proterozoic basement is significantly better constrained than in the study by Zielhuis & Van der Hilst (1996).

Along the eastern seaboard of the Australian continent there is a pronounced low velocity zone between 100 and 200 km in depth (figure 6); the minimum wavespeed seems to occur at a depth of 140 km. This low velocity zone was recognised in earlier surface wave dispersion studies (see Muirhead & Drummond 1991 for a review) but a striking feature in our 3-D models is the level of lateral variation in the character of the zone. The low velocity zone is interrupted near 30°S , 150°E beneath the New England fold belt and the higher velocities in this region seem to be almost continuous from the surface to the transition zone. The main zones of lowered velocities correlate quite well with recent volcanism and high heat flow. The low speed anomalies appear to extend to greater depth beneath the Coral Sea and beneath southeastern corner of Australia. Zielhuis & Van der Hilst (1996) discuss the upper mantle structure beneath easternmost Australia in more detail.

In the upper 200 km beneath central Australia shear wavespeed is high, but the images suggest significant lateral variations that begin to delineate the major crustal elements. The zone of high wavespeed in the central north (Figures 6A-C) coincides with the lateral extent of the North Australian craton, and the high wavespeeds in the central south coincide with the Gawler craton and the Eucla block (Figures 6A,B). At 80 km depth, the region associated with the Alice Springs orogeny - in particular the Amadeus basin and the Musgrave block - is characterized by slower shear wave propagation than in the adjacent shields (Figure 6A). The images suggest that the north Australia craton extends northward into western Papua New Guinea and eastern Indonesia (from Timor to Irian Jaya). Interestingly, the Kimberley block, near 15°S , 125°E is delineated by slower wave propagation than the shield further to the east, which suggests that the Kimberley basin is not underlain by the same basement as the Proterozoic North Australia craton. The change to slower wave propagation occurs across the Ord basin and the Halls Creek shear zone. The high wavespeeds mapped in the south west may well be related to the Archæan cratons but they are not yet well localized owing to insufficient path coverage.

The amplitude of wavespeed variability is diminished below 200 km depth but significant contrasts remain. At 200 km depth (Figure 6C) the images reveal again a difference between the wavespeeds in eastern and central Australia. The eastern edge of the high wave speeds that characterize the regions of Proterozoic basement seems to coincide with the southeastern margin of the Mt. Isa inlier (20°S , 140°E) and the western boundary of the Eromanga basin and extend approximately along the 140°E meridian down the eastern side of the Gawler craton (Figure 1A).

At depths larger than 300 km (Figure 6D) the general trends in the anomalies is

markedly different than in the shallower upper mantle (Figures 6A-C). The predominant orientation of the gradients is no longer west-east, although even at these large depths the strongest low wavespeed anomalies are located in the east, that is, beneath the Coral Sea and, in particular, the Tasman Sea. Between 300 and 400 km depth there are prominent high wavespeeds beneath the eastern part of the continent, in a broad band extending from 20°S, 143°E south to around 35°. We have previously noted the high velocities beneath the New England fold belt near 30°S, 152°. These anomalies (discussed in more detail by Zielhuis & Van der Hilst 1996) are robust features of the solution and are confirmed by a simple differential technique applied to a small number of high-quality Rayleigh wave data (Passier et al. 1997). The high wavespeeds beneath the western parts of the Musgrave blocks and the Officer basin may be real, but we can not be confident in the mapping of this structure until data from the SKIPPY arrays in West Australia have been analyzed. For the deeper part of the upper mantle, the images display several 'streaks' that may result from a combination of uneven sampling, effects of source mislocation, or arise from the neglect of inter-mode coupling for the higher mode packet. This will be subject to further study.

Vertical sections through the three-dimensional shear wavespeed model for the upper mantle (figure 7) provide further insight into the character of the lithosphere in different regimes. For the purpose of the present paper we loosely associate the "lithosphere" with a zone of elevated shear velocity compared with the asthenosphere beneath. The locations of the cross sections are given in Figure 1A.

A section from the Coral Sea across the eastern margin of the Australian continent into the Proterozoic shield (figure 7A) displays the large contrast in lithosphere thickness between the oceanic and continental shield regions. Beneath the Coral Sea a negative gradient in shear velocity starts at a depth of about 50 km, beneath the coastal region of easternmost Australia the lithosphere thickness is about 100 km, and reduced shear wavespeeds do not start until a depth of about 250 km beneath the central Proterozoic cratons (Figure 7A). The virtual absence of a high wavespeed lid near 145°E coincides with the region of Neogene volcanism in the Queensland volcanic province, which may suggest that part of the continental lithosphere has been eroded by thermal processes.

The east-west cross section at 24°S (Figure 7B) reveals a similar contrast in lithosphere thickness between eastern Australia and the central shields. The high wavespeeds associated with the seismological lithosphere are detected to depths exceeding 300 km beneath West Australia (130°E). The image clearly reveals the low velocity zone extending beneath eastern Australia (east of 140°E) that separates thin high wavespeed lid from the deeper zone of high wavespeed anomalies between 300 and 400 km depth. This cross section intersects the volcanic province at approximately 150°E.

The seismic structure shallower than 80 km may be contaminated by variations in crustal structure that are not adequately accounted for by our approach, but the cross sections clearly reveal a pronounced wavespeed anomaly in the region associated with

the Alice Springs orogeny and the eastern part of the Canning basin (125°-135°E). At 30°S the model reveals the large lateral variations in wavespeed near the Broken Hill block, i.e. across the southern part of the Tasman Line. At this latitude the seismically defined lithosphere is about 200 to 250 km thick beneath most of the Proterozoic shields (between 125° and 140°E), and possibly even thicker beneath the Archæan cratons further west. The latter observation is, however, tentative because data coverage is not sufficient to constrain the structures in the southwestern part of the continent.

The map views (Figures 6A-C) and the vertical sections (Figures 7A-C) clearly delineate the transition from thin lithosphere beneath the Phanerozoic of eastern Australia to the thick Proterozoic shields of central Australia. Locally, in particular south of 25°S, the transition is complex and may comprise multiple boundaries and basement types.

The north-south cross sections (Figures 7D-F) further illustrate the pronounced differences in character of the high wavespeed lid between east Australia on the one hand and the central and western parts of the continent on the other. The thickest lid is located beneath the western part of the Officer basin (at about 25°S, 129°E) (Figure 7D), that is near the boundary of the Proterozoic and Archæan shields. The observation of such a thick high wavespeed lid in the western part of the continent, and the absence of a strong negative velocity gradient in shear velocity beneath the lid is in good agreement with the path average shear wave profile by Gaherty & Jordan (1995). At 129°E (Figure 7D) the sudden increase in wavespeed at about 35°S marks the ocean-continent transition in the great Australian Bight, and the deep high wavespeeds north of 10°S are probably related to subduction beneath eastern Indonesia. The cross section at 143°E (Figure 7E) displays the intermediate thickness of the lithosphere in the region where the transition from the coastal region to the central shields is gradual. The rapid lateral variations near 30°S coincide with the boundary between the Murray and Eromanga basins (i.e., parts of the Broken Hill block, the Lachlan fold belt, and the Darling basin). This section also illustrates the deep anomaly near 22°S in Queensland. Figure 7F displays the deep low wavespeed anomaly beneath the Tasman sea region, the low velocity zone beneath easternmost Australia, and the deep high wavespeed anomaly beneath the New England fold belt.

These significant results have been derived from the analysis of data from only part of the SKIPPY project. More detail on lithospheric and mantle structure beneath the western part of Australian region will be revealed as the data from the last two SKIPPY deployments are incorporated into the inversion for three-dimensional structure.

3.2 P wave tomography

An additional source of information on three-dimensional structure comes from P wave tomography using the residuals of observed arrival times of P phases compared with the predictions from a suitable reference model. The residuals reflect the integrated influence of wavespeed variations in the Earth's interior along the propagation path

from source to receiver. With sufficient crossing paths, the travel time information can be used to reconstruct the three-dimensional variations in seismic wavespeed.

In order to produce a homogeneous set of travel time residuals the arrival times determined from the SKIPPY records are incorporated in the data processing scheme of the U.S. Geological Survey's National Earthquake Information Center (NEIC). In this way, the SKIPPY data help constrain the hypocentres of earthquakes in the Australasian region, and in return are made to be consistent with the global data set assembled by Engdahl, Van der Hilst & Buland (1997).

Travel time residuals from the SKIPPY project were first used by Widiyantoro & Van der Hilst (1996) in their tomographic study of the complex subduction beneath the Indonesian region. Their three-dimensional mantle model was generated by embedding a high-resolution representation of regional structure in a somewhat lower resolution cellular model for the rest of the mantle. By this means contamination of the regional structure by features outside the region of interest can be minimised. The inversions for the Indonesian region incorporated phase data from the SKIPPY records in Queensland and permanent stations in Australia and reveal the thick lithosphere under northern part of central Australia.

With more phase picks now available from later SKIPPY deployments (SK1, SK2, SK3, and BAS), in addition to data from the network of short-period permanent stations, the P wave tomography has been extended to cover most of the continent, with resolution in the eastern part significantly better than in the west. Figure 8 displays the lateral variation in P wavespeed relative to the *ak135* reference model at a depth of approximately 150 km beneath the Australian region. The image reveals the lateral contrast between high and low wavespeeds in northern Queensland which is prominent in the shear wave structure inferred from the waveform analysis described above. The resolution of structure in oceanic regions is, of course, poor because of lack of station coverage.

Much of the information used to construct the P wave velocity model comes from arrivals travelling rather steeply in the mantle so that vertical resolution is limited. Nevertheless the strong contrast in the seismic signature of the lithosphere between western and central Australia and the eastern seaboard are clearly revealed. As in the shear wave images the zone of higher wavespeeds extends further east than the conventional Tasman Line but thicker lithosphere lies mostly to the west of 140°E. There are some significant differences in the P and S wavespeed models, for instance beneath the New England fold belt. These differences may largely be due to variations in data coverage and resolution, but upon further analysis they may also yield new information about the physical nature of the anomalies, as for example whether their origin is thermal or compositional.

3.3 Receiver based studies

Along with their use in tomographic studies, the even distribution of portable broadband stations across Australia can also be exploited to provide a range of information on the structure beneath each of the stations.

3.3.1 Receiver function analysis

For each of the broadband stations in the SKIPPY deployments, data from distant seismic events are being processed to extract a receiver function which is sensitive to the structure in the crust and the uppermost mantle and particularly the character of major seismic interfaces such as the Moho. The analysis uses the P wave onset and its immediate coda. The radial and vertical components of the record share the same source time function, so that the dependence on the radiation from the source can be largely eliminated by deconvolving the waveform segment of the radial horizontal component, lying along the great-circle path from the source, with the corresponding segment of the vertical component (Langston 1979). The deconvolved radial receiver function then emphasises the influence of near receiver structure and can be inverted in the time domain for a 1-D shear wave velocity model of the crust and uppermost mantle (see e.g. Ammon et al. 1990). A major contribution to the receiver function comes from conversions between P and S waves. The timing and amplitude of such arrivals provide constraints on the properties of major interfaces such as the crust-mantle boundary and internal boundaries within the crust. For example, a sharp crust/mantle boundary produces a converted phase with about 5 s separation from P.

The inversion of the receiver functions to recover crustal and uppermost mantle structure is widely recognised to be sensitive to the starting model if a conventional linearisation scheme is employed (see e.g. Ammon et al. 1990). However, such difficulties can be overcome by employing an inversion scheme based on a Genetic Algorithm (Shibutani et al. 1996). This approach makes use of a "cloud" or "population" of models to minimise the dependence on a starting model; a set of biological analogues are used to produce new generations of models from previous generations with preferential development of models with a good fit between observed and theoretical receiver functions. The approach provides a good sampling of the model space and enables the estimation of the shear wavespeed distribution in the crust along with an indication of the ratio between P and S wavespeeds. Many models with an acceptable fit to data are generated during the inversion and a stable crustal model is produced by employing a weighted average of the best 1000 models encountered in the development of the genetic algorithm. The weighting is based on the inverse of the misfit for each model so that the best fitting models have the greatest influence.

At each station a stacked receiver function was constructed from teleseismic observations. For each event, the receiver function was low-pass filtered to eliminate frequencies above 1 Hz in order to minimize the influence of small scale heterogeneities. Subsequently, the receiver functions from 6 – 18 teleseismic events at each station

were stacked together for a set of ranges of backazimuths. The weighting used in the stacking emphasizes receiver functions with higher signal-to-noise ratios and those whose backazimuth and incident angle were closer to the mean for the set of events.

The radial component of the stacked receiver function was then inverted for a 1-D velocity model beneath each station. In the Genetic Algorithm inversion, the crust and uppermost mantle down to 60 km was modelled with six major layers: a sediment layer, basement layer, upper crust, middle crust, lower crust and uppermost mantle. The model parameters in each layer are the thickness, the S wave velocity at the upper boundary, the S wave velocity at the lower boundary and the velocity ratio between P and S waves (V_P/V_S). The S wave velocity for each layer is constructed by linearly connecting the values at the upper and lower boundaries, to give a sequence of constant velocity gradient segments separated by velocity discontinuities.

The results of the receiver function inversion for the stations SB06 and SA07 are shown in figure 9. All 10,000 models searched in the Genetic Algorithm inversion for S velocity are shown as the light gray shaded area and superimposed on this the best 1,000 models are shown with darker gray tones, where the darkness is logarithmically proportional to the number of the models. The best fitting model for each site is shown as a black line. However a more useful and stable result is provided by the averaged model generated by weighting the best 1,000 models by the inverse of their misfit values. This averaged model is shown in white for S velocity and in a solid line for the V_P/V_S ratio. The lower panel in figure 9 compares the waveforms of the stacked receiver function to synthetics calculated for the averaged models. The fit to the major phases is good, and this will be true of most of the best 1,000 models. The zone of darker gray in the upper part of figure 9 can therefore be thought of as an indicator of the constraint on the crust and upper mantle structure. Both SB06 and SA07 have surficial sediment with very low velocities so that P-to-S converted phases and reverberations (1 – 3 s) originating in the sediment layer are larger than the direct P phase which arrives at zero time.

The analysis for crustal structure has been completed for all the SKIPPY stations in the SK1 and SK2 arrays in eastern Australia and is in progress for the permanent stations and the later SKIPPY arrays. The parametrisation of the model at each station is via a sequence of velocity gradients and discontinuities; sensitivity analysis indicates that the dependence on phase conversions enhances the resolution of boundaries at the expense of the gradients. Nevertheless, all the models have been derived by the same procedure and we can make direct comparisons and extract a wide range of information on crustal structure and uppermost mantle structure across eastern Australia. In the few places where direct comparisons can be made, e.g. ZB12, there is a very good concordance between the character of the S velocity structure from the receiver function inversion and the previous P velocity model from refraction studies.

Figures 10, 11 and 12 summarise the properties of the crustal models at each of the SKIPPY stations in eastern Australia in terms of the major subdivisions of the crust:

the upper crust (fig 10), middle/lower crust (fig 11) and the crust-mantle boundary and uppermost mantle velocities (fig 12). In each map we indicate the thickness of the layer, the corresponding crustal velocities and the character of the boundary. A sharp boundary is associated with a clear converted phase in the receiver function waveform whereas the expression of a transitional zone is more subtle. The nature of the boundaries are classified into the categories: SHARP (≤ 1 km), THIN (≤ 4 km), TRANSITIONAL OR INTERMEDIATE (≤ 10 km), and BROAD (> 10 km). The depth of the crustal boundaries was estimated at each station; for a transitional zone the lower boundary was selected.

The information from the receiver function inversion provides a major supplement to the previous results from isolated refraction and reflection experiments and in the crustal thickness map in figure 12 the earlier information (from Collins 1991, indicated by crosses) has been combined with the present results. The crust-mantle boundary is deep (38 – 44 km) and mostly transitional in character along the axis of the fold belt zone in the east (from stations: ZB12, SB09 to SA05, SA03). A relatively sharp Moho is found at a shallower depth (30 – 36 km) at the western edge of the study area close to the boundary between Phanerozoic and Precambrian exposure.

A major advantage of the receiver function approach is that it provides good constraints on shear velocities in the crust and uppermost mantle, which are not well resolved by the partitioned waveform inversion of the S wave and surface wave portions of the seismogram. The 3-D models are most reliable from 60 km down, whereas the receiver function analysis is most effective above 60 km. There is a good agreement between the results from the waveform tomography and the receiver function analysis at 60 km depth.

3.3.2 SKS splitting

In addition to mapping isotropic variations in shear wavespeed, the SKIPPY project has also enabled us to investigate continental azimuthal anisotropy on an unparalleled scale. From observations of shear wave splitting of the seismic core phase SKS, the angle of fast polarisation direction (ϕ) and the time difference between fast and slow SKS waves (dt) has been extracted for many of the SKIPPY stations and a number of permanent stations, see Clitheroe & Van der Hilst (1997, this issue). The broad-band data demonstrate that SKS splitting is manifested at different frequencies. At a frequency of about 1 Hz, dt is 0.3–0.6 s, and ϕ parallels pre-existing crustal fabric. At lower frequencies ϕ varies across the continent: ϕ is inconsistent with present-day plate motion direction, but can probably be explained by predominant mineral orientation in the sub-crustal lithosphere. The resemblance between the location of the assumed eastern boundary of the central cratons and the spatial pattern of ϕ in the east of Australia may suggest that shear wave splitting carries information about either the deep structure of the mountain belts formed during the Palaeozoic accretion of terranes onto the central cratons or

about asthenospheric flow around the undulating eastern edge of the deep cratonic keel.

4 CONCLUSION

Over the last decade there has been a significant increase in knowledge of the P and S wave velocities in the mantle, particularly beneath northern Australia. The current generation of three-dimensional studies based on the use of portable seismometers have the potential to dramatically increase the level of understanding of mantle structure beneath the Australian region and in particular the contrast between eastern and western Australia.

ACKNOWLEDGMENTS

The study of mantle structure beneath Australia has involved many members of the Seismology Group at the Research School of Earth Sciences both in the field and in subsequent analysis. We would like to thank Doug Christie, John Grant, Armando Arcidiaco, Tony Percival, Gus Angus and Jan Hulse for their efforts in the field in often trying and uncomfortable conditions. Alet Zielhuis, Roger Bowman, Phil Cummins, Oli Gudmundsson, Cheng Tong, Geoff Clitheroe and Jan Weekes have all contributed to the analysis of data from the portable stations. Takuo Shibutani is gratefully acknowledged for his work on the receiver function analysis.

References

- Ammon, C.J., G.E. Randall, and G. Zandt, 1990. On the nonuniqueness of receiver function inversions, *J. Geophys. Res.*, **95**, 15,303-15,318,
- Bowman J.R. & Kennett B.L.N., 1990. An investigation of the upper mantle beneath northwestern Australia using a hybrid seismic array, *Geophys. J. Int.*, **101**, 411-424.
- Clitheroe G. & van der Hilst R.D., 1997. Complex anisotropy in the Australian lithosphere from shear-wave splitting in broad-band SKS records *this issue*
- Collins, C.D.N., 1991. The nature of the crust-mantle boundary under Australia from seismic evidence, *The Australian Lithosphere*, B. J. Drummond (ed.), Geol. Soc. Aust., Spec. Publ. **17**, 67-80.
- Denham D., 1991. Shear wave crustal models for the Australian Continent, *The Australian Lithosphere*, B. J. Drummond (ed.), Geol. Soc. Aust., Spec. Publ. **17**, 59-66
- Dey S.C., Kennett B.L.N., Bowman J.R., & Goody A., 1993. Variations in upper mantle structure under northern Australia, *Geophys. J. Int.*, **114**, 304-310.
- Engdahl, E.R., Van der Hilst, R.D., & Buland, S.P., 1997. Updated global hypocentres by event relocation including depth phases, *Bull. Seism. Soc. Am.* (submitted).
- Gaherty, J. & Jordan. T.H., 1995. Lehmann discontinuity as the base of an anisotropic layer beneath continents, *Science*, **268**, 1468-1471
- Grand S. & Helmberger D.V. 1984. Upper mantle shear structure of North America, *Geophys. J. R. astr. Soc.*, **76**, 399-438.

- Gudmundsson O., Kennett B.L.N. & Goody A., 1994. Broadband observations of upper mantle seismic phases in northern Australia and the attenuation structure in the upper mantle. *Phys. Earth Planet Inter.*, **84**, 207-226.
- Hales A.L., Muirhead K.J. & Rynn J.W., 1980. A compressional velocity distribution for the upper mantle, *Tectonophys.*, **63**, 309-348.
- Kennett B.L.N. & R.D. van der Hilst., 1996. Using a synthetic continental array to study the Earth's interior, *J. Phys. Earth*, **44**, 669-674.
- Kennett B.L.N., Gudmundsson O., & Tong C., 1994. The upper-mantle S and P velocity structure beneath northern Australia from broad-band observations, *Phys. Earth Planet. Inter.*, **86**, 85-98.
- Kennett B.L.N., Engdahl E.R. & Buland R., 1995. Constraints on seismic velocities in the Earth from travel times, *Geophys J Int*, **122**, 108-124.
- Langston, C.A., 1979. Structure under Mount Rainier, Washington, inferred from teleseismic body waves, *J. Geophys. Res.*, **84**, 4749-4762.
- LeFevre L.V. & Helmberger D.V., 1989. Upper mantle P velocity structure of the Australian shield, *J. geophys. Res.*, **94**, 17749-17765.
- Leven J.H., 1985. The application of synthetic seismograms in the interpretation of the upper mantle P-wave velocity structure in northern Australia, *Phys. Earth Planet. Int.*, **38**, 9-27.
- Muirhead K.J. & Drummond B.J., 1991. The seismic structure of the lithosphere under Australia and its implications for continental plate tectonics, in *The Australian Lithosphere*, B. J. Drummond (ed.), Geol. Soc. Aust., Spec. Publ. **17**, 23-40.
- Nolet G., 1990. Partitioned waveform inversion and two-dimensional structure under the Network of Autonomously Recording Seismographs, *J. geophys. Res.*, **95**, 8499-
- Nolet G., Grand S. & Kennett B.L.N., 1994. Seismic heterogeneity in the Upper Mantle, *J. Geophys. Res.*, **99**, 23753-23766.
- Shibutani T., Sambridge M. & Kennett B.L.N., 1996. Genetic algorithm inversion for receiver functions with application to crust and uppermost mantle structure beneath Eastern Australia, *Geophys. Res. Lett.*,
- Tong C., Gudmundsson O. & Kennett B.L.N., 1994. Shear wave splitting in refracted waves returned from the upper mantle transition zone beneath northern Australia, *J. geophys. Res.*, **99**, 15783-15797.
- Trampert, J., & Woodhouse, J.H., 1995. Global phase velocity maps of Love and Rayleigh waves between 40 and 150 seconds, *Geophys. J. Int.*, **122**, 675-690.
- Van der Hilst R., Kennett B., Christie D. & Grant J., 1994. Project SKIPPY explores the mantle and lithosphere beneath Australia, *EOS*, **75**, 177,180,181
- Widiyantoro S. & Van der Hilst R.D., 1996 The slab of subducted lithosphere beneath the Sunda arc, Indonesia *Science*, **271**, 1566-1570.
- Zielhuis A. & Van der Hilst R.D., 1996. Mantle structure beneath the eastern Australian region from Partitioned Waveform Inversion, *Geophys. J. Int*, **127**, 1-16.

Figure 1. (A) Map of the crustal elements and tectonic units referred to in the text, together with the lines of the sections in figure 7. [Key: Ar - Arunta Block, Am - Amadeus Basin, BH - Broken Hill Block, Ca - Canning Basin, Da - Darling Basin, Er - Eromanga Basin, Eu - Eucla Basin, Ga - Gawler Block, HC - Halls Creek Belt, Ki - Kimberley Block, La - Lachlan Fold Belt, MI - Mt Isa Block, Mu - Musgrave Block, NE - New England Fold Belt, Or - Ord Basin, Of - Officer Basin]. (B) Configuration of portable seismic recording stations 1985-1996. Short-period stations are indicated by open triangles. Portable broadband stations are marked by solid symbols. Permanent stations with high fidelity recording are indicated by a double circle and station name. The approximate location of boundary between Precambrian outcrop in western and central Australia and the Phanerozoic east is indicated by a shaded line.

Figure 2. A composite record section of unfiltered broadband seismograms for five New Guinea events recorded at SKIPPY stations in Queensland. The section is constructed from the vertical component for each path and covers the P and SV waves returned from the upper mantle. The travel time curves are for an event at 25 km depth in the *ak135* reference model (Kennett, Engdahl & Buland 1995)

Figure 3. Enlargement of the S wave arrivals for composite record sections of unfiltered broadband seismograms for five New Guinea events recorded at SKIPPY stations in Queensland. Sections are shown for both the radial (*R*) and tangential components (*T*) constructed for each path. The travel time curves are for an event at 25 km depth in the *ak135* reference model (Kennett, Engdahl & Buland 1995)

Figure 4. P and S velocity and attenuation structure for the upper mantle beneath northern Australia determined from a combination of short-period and broadband observations

Figure 5. Wavepath coverage available for the SKIPPY experiment in eastern and central Australia. (a) wave paths exploited by Zielhuis & Van der Hilst (1996); (b) wave path coverage use in this study.

Figure 6. Three-dimensional shear wavespeed model derived from partitioned waveform inversion from the SKIPPY experiment in eastern and central Australia. Map views at (a) 80 km, (b) 140 km, (c) 200 km, and (d) 300 km depth. Based on the path coverage (Figure 5B) the wavespeed anomalies are reliably imaged east of about 125°E.

Figure 7. Vertical cross-sections through the three-dimensional shear wavespeed derived from partitioned waveform inversion from the SKIPPY experiment in eastern and central Australia. Cross sections at (a) 16°S, (b), 24°S, and (c) 30°S, and north-south sections at (d) 129°E, (e) 143°E, and (f) 151°E

Figure 8. Cross-section through the 3D model of the P wave velocities in the Australian region for the depth interval from 160-220 km

Figure 9. Genetic algorithm inversion of a receiver function to determine S wave structure and the V_P/V_S ratio. All 10,000 models searched in the GA inversion are shown as the light gray shaded area. The best 1,000 models are shown with darker gray shaded area. The darkness is logarithmically proportional to the number of the models as shown by the scale bar. The best model and the averaged model are shown by the black solid line and the white solid line, respectively. For the V_P/V_S ratio, the solid line indicates the averaged model.

Figure 10. Summary of velocity and thickness information for the upper crust in eastern Australia

Figure 11. Summary of velocity and thickness information for the middle and lower crust in eastern Australia

Figure 12. The depth of the crust-mantle boundary beneath eastern Australia, and the S wave velocity and V_P/V_S ratio at the top of the mantle. The nature of the crust-mantle boundary is classified into four categories : SHARP (≤ 1 km), THIN (≤ 4 km), INTERMEDIATE (≤ 10 km), and BROAD (> 10 km). The crosses indicate the locations for which the crustal structure has been obtained previously from refraction surveys [Collins, 1991]. These data were incorporated into the contouring.

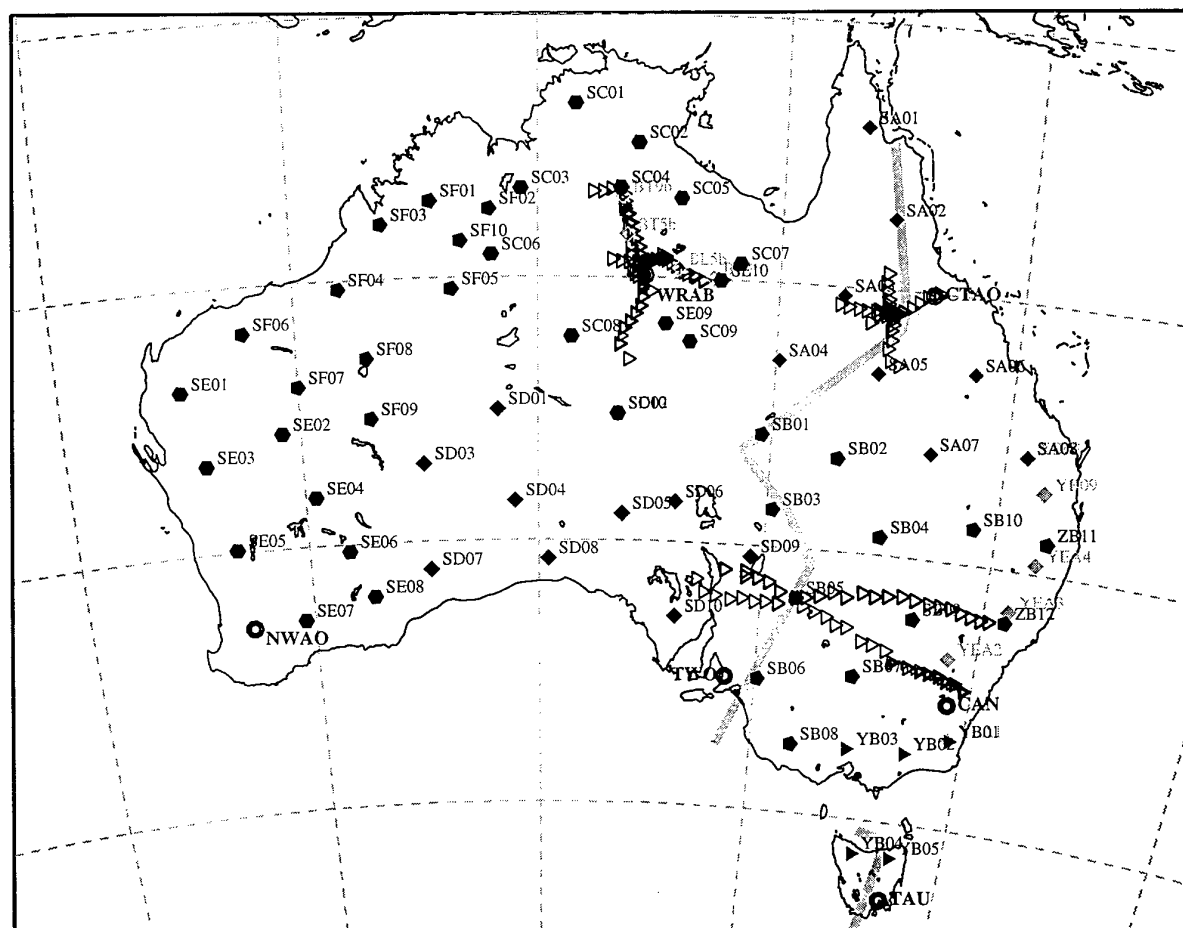
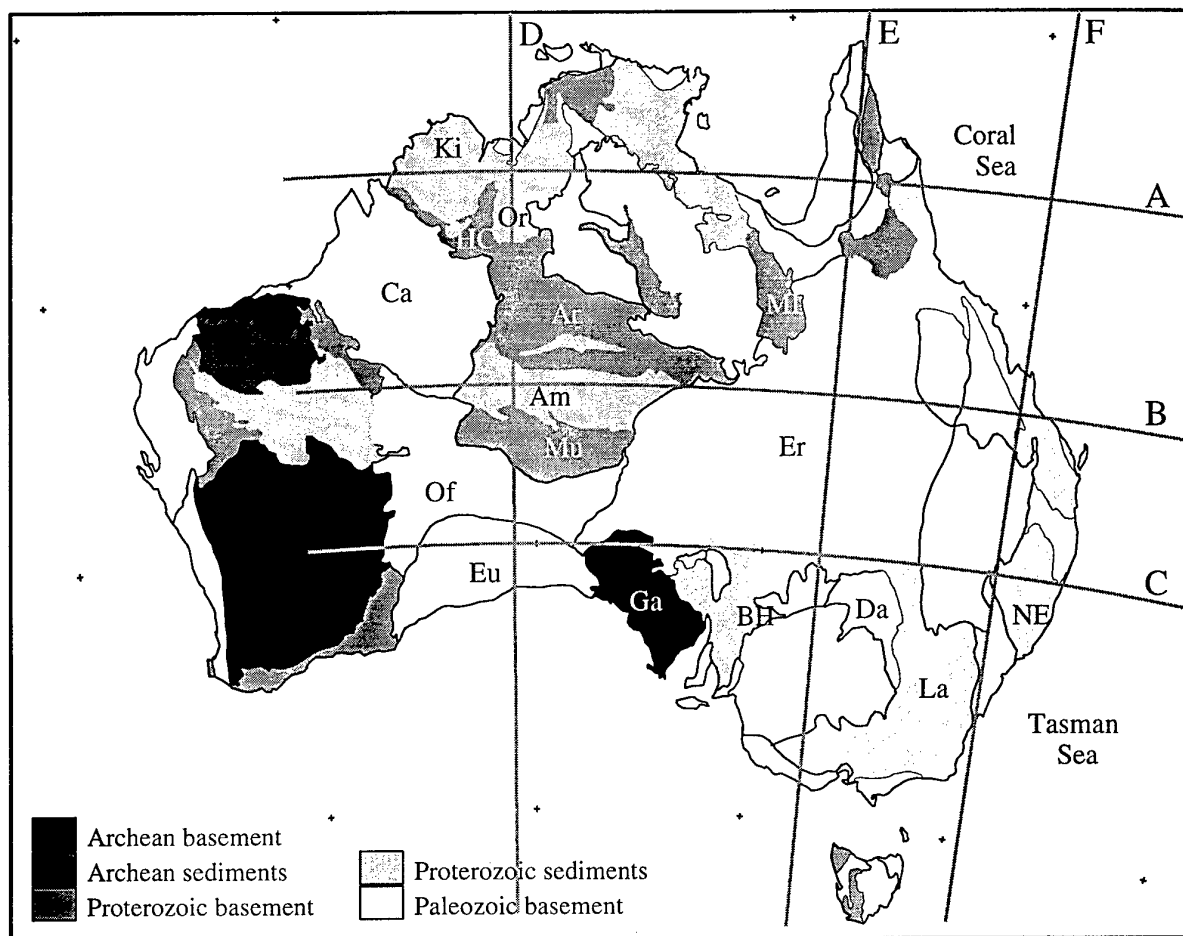


Fig 1

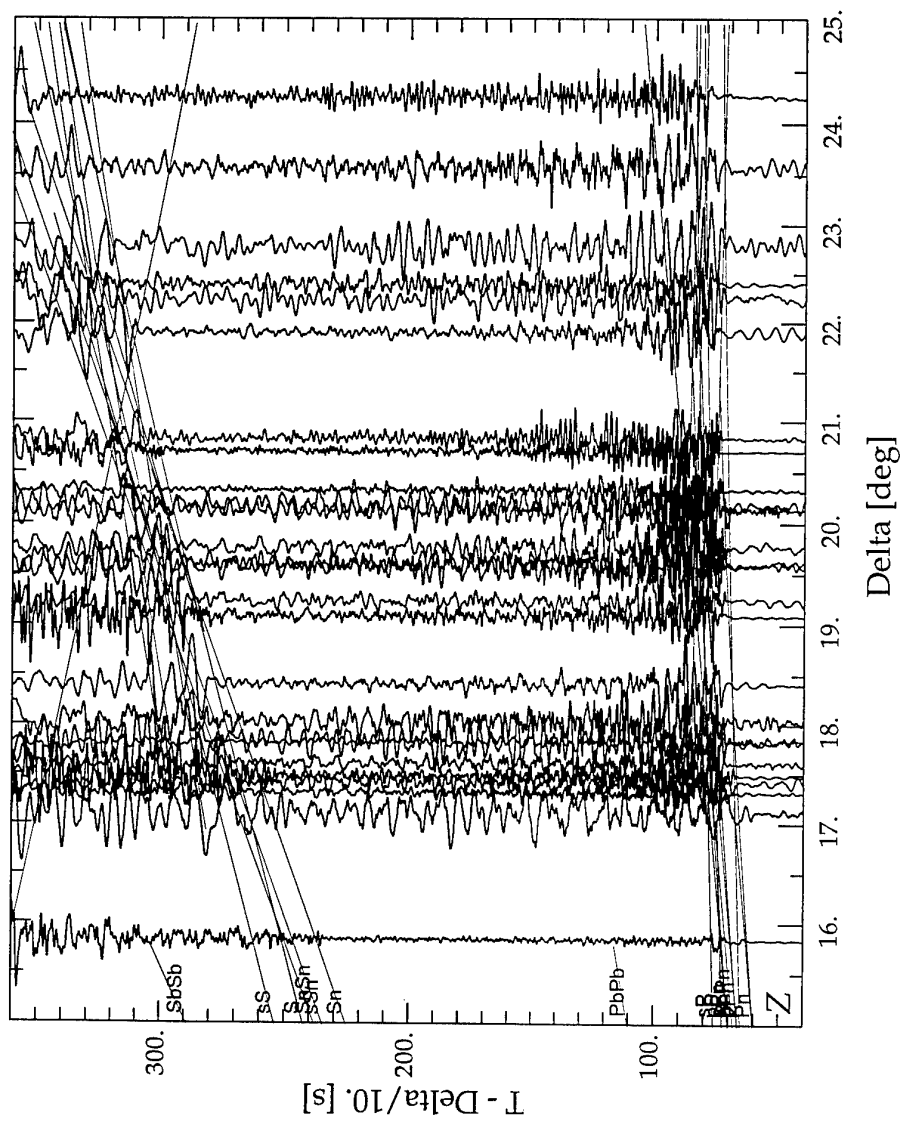


Fig 2.

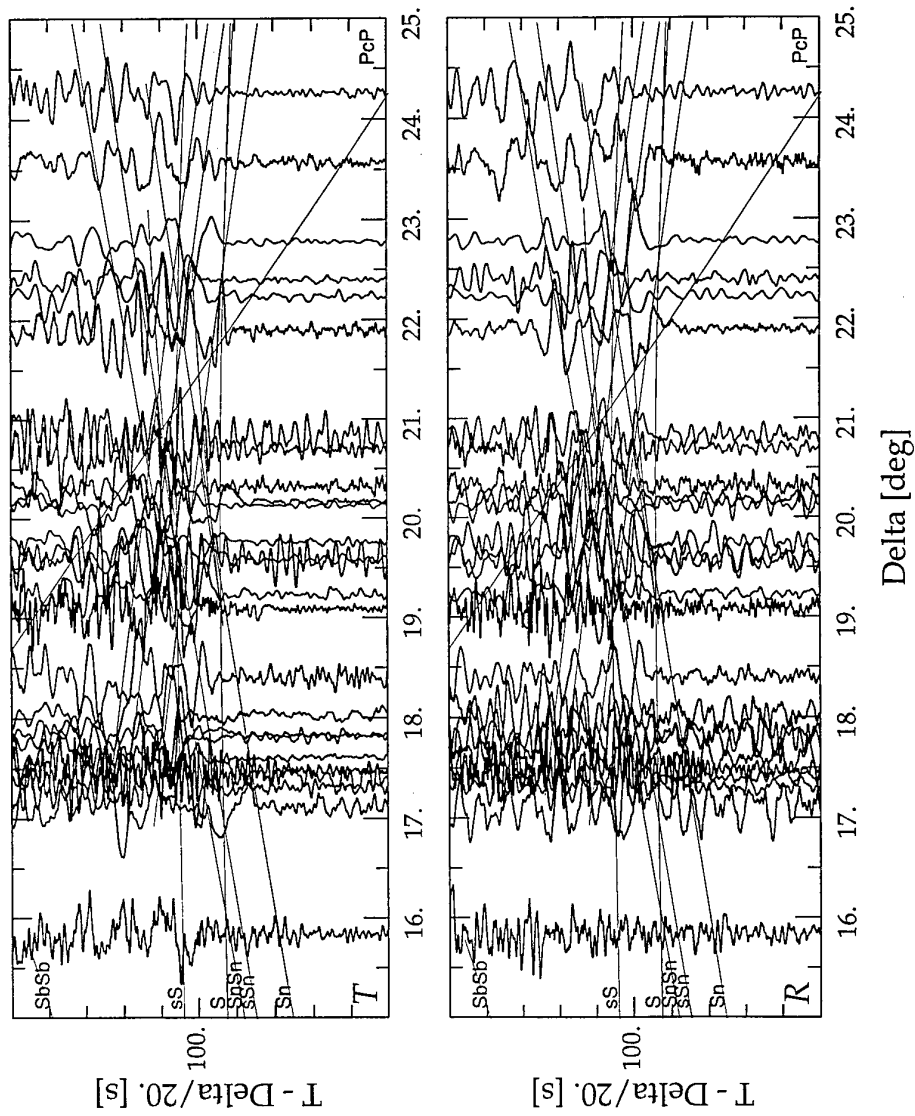


Fig 3

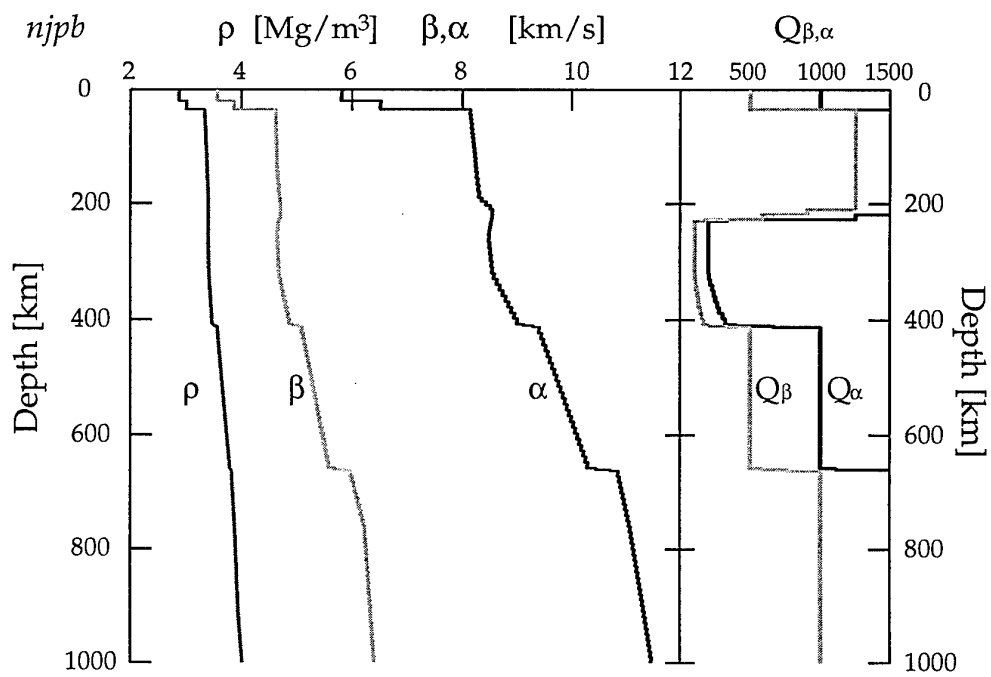


fig 4

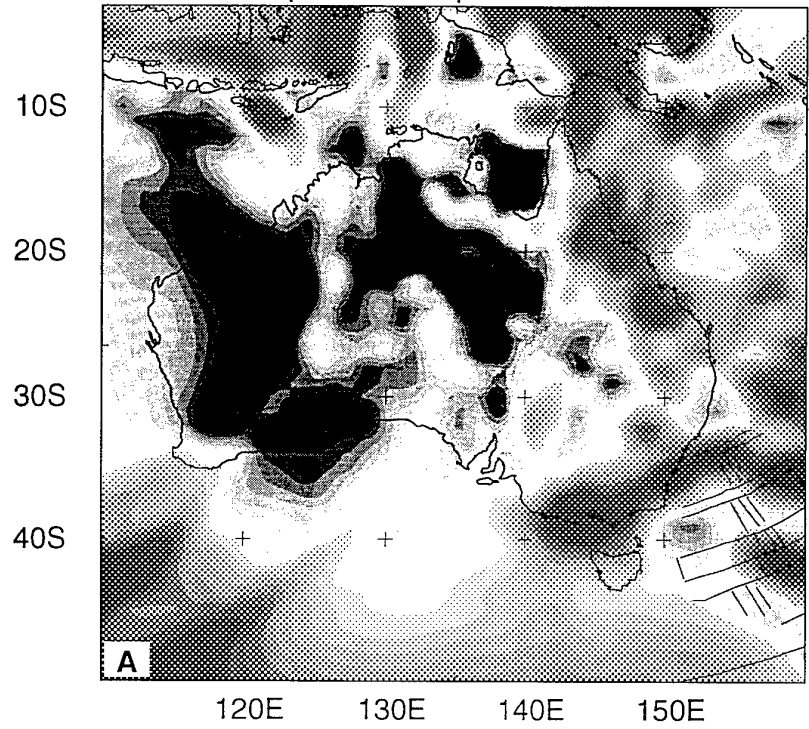
fig 5. ps



Fig 6

Van der Hilst & Garnero (AGU 1994) (Monograph 1997)

Shear-wave speed at a depth of 80 km



Shear-wave speed at a depth of 140 km

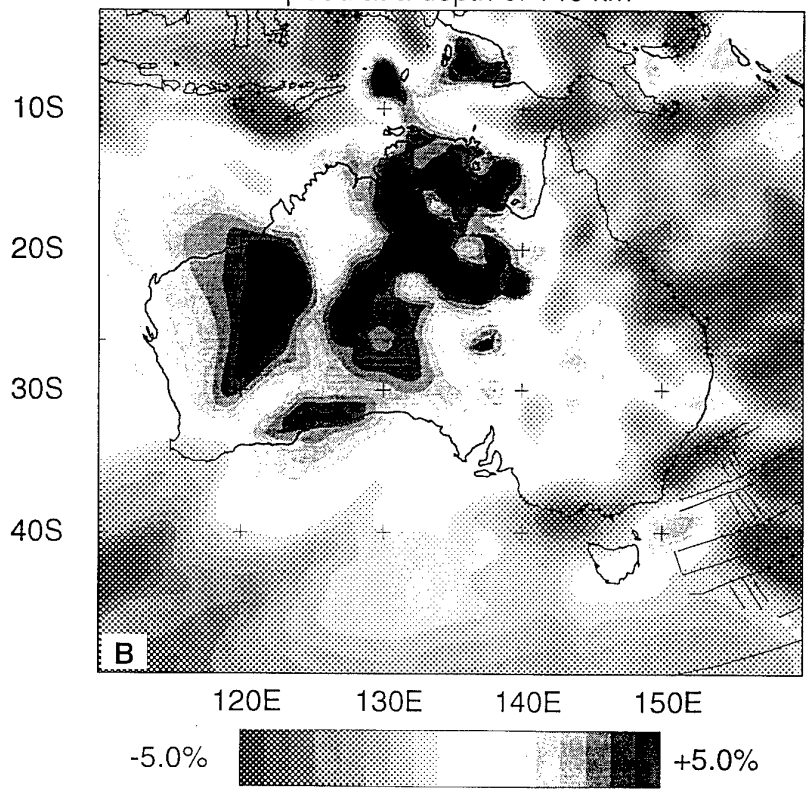
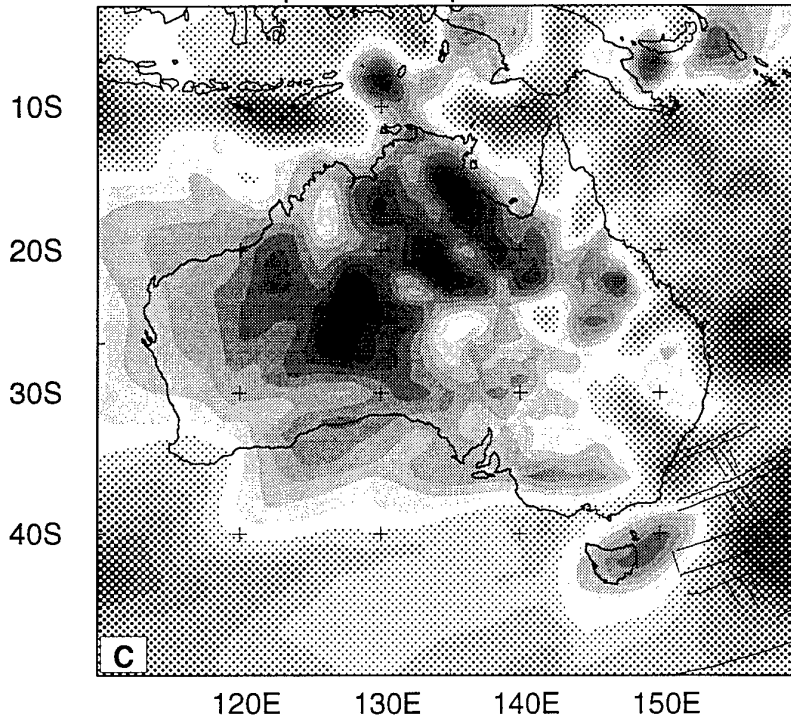


fig 6 (cont).

Van der Hilst & Kennett (AGU Geodynamics Monograph 1997)

Shear-wave speed at a depth of 200 km



Shear-wave speed at a depth of 300 km

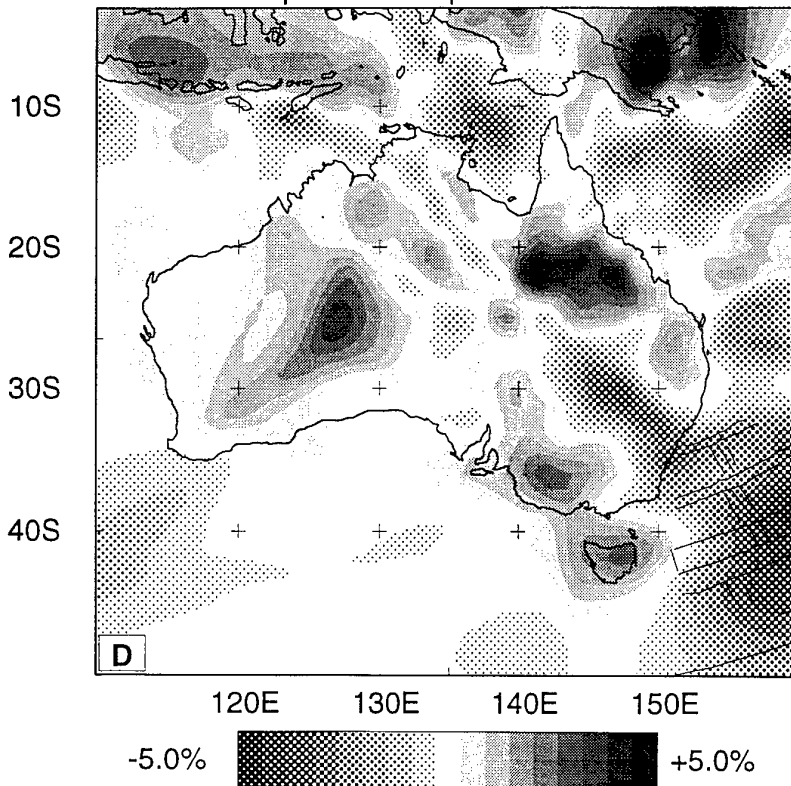
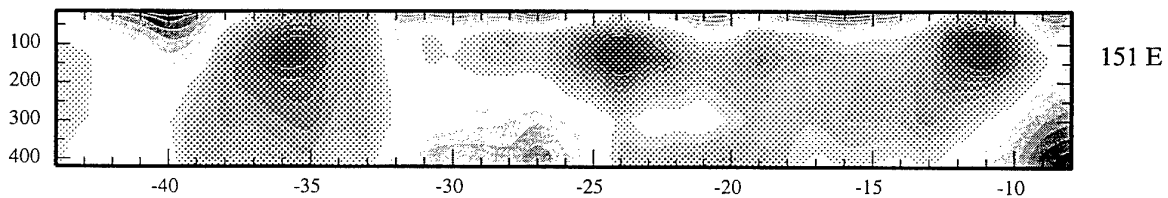
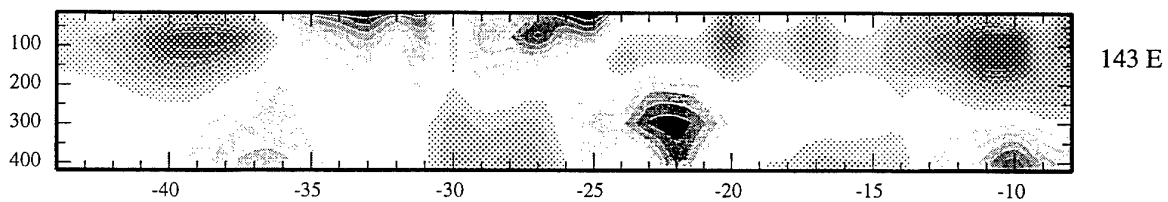
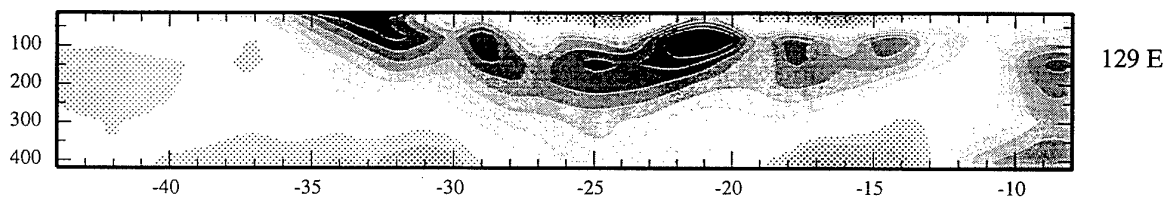
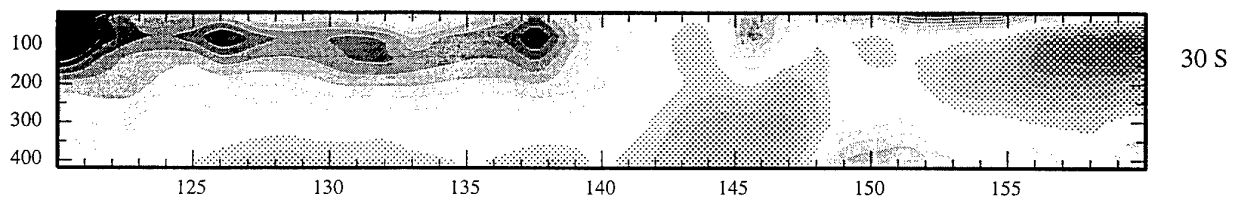
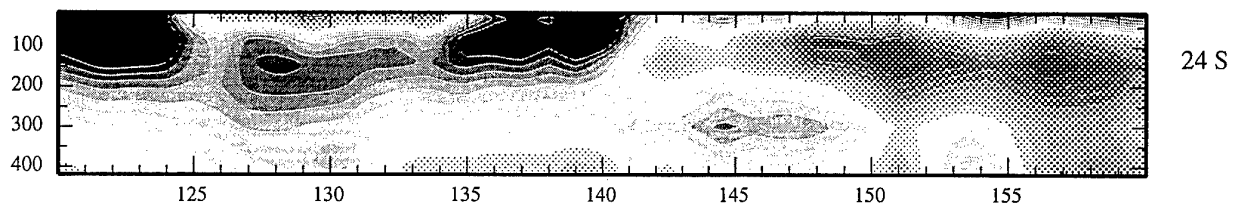
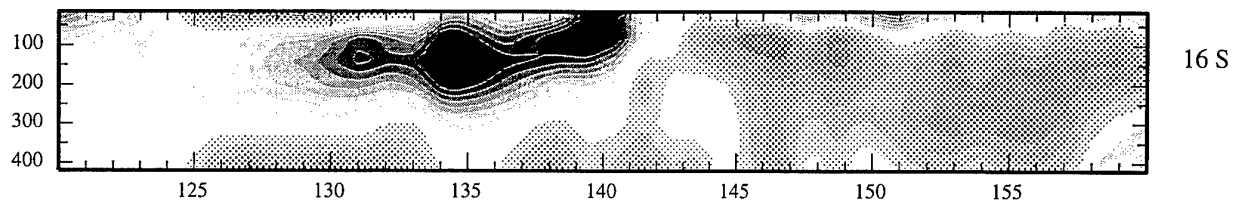


Fig 7



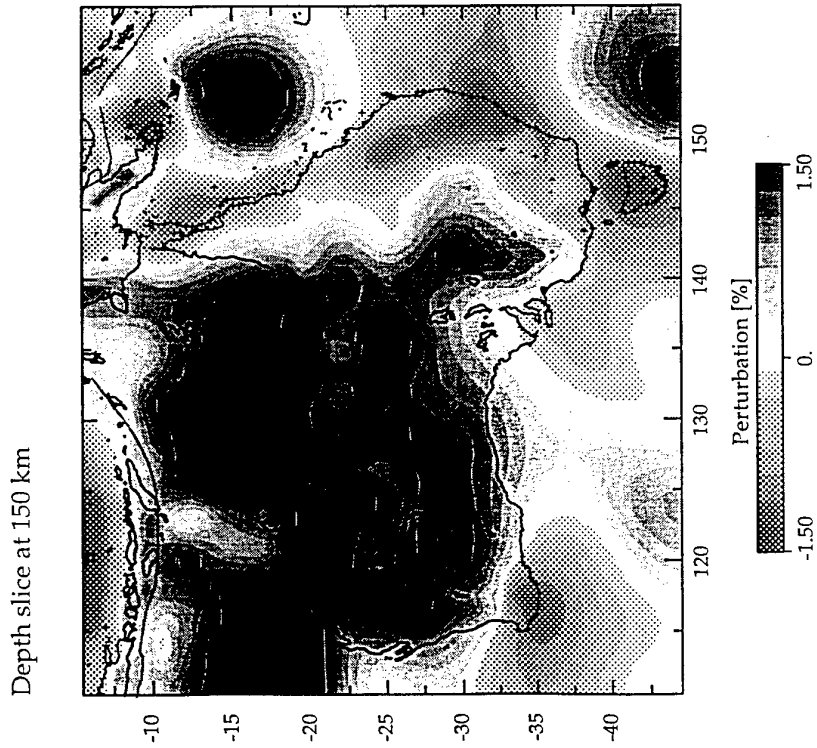


fig 8

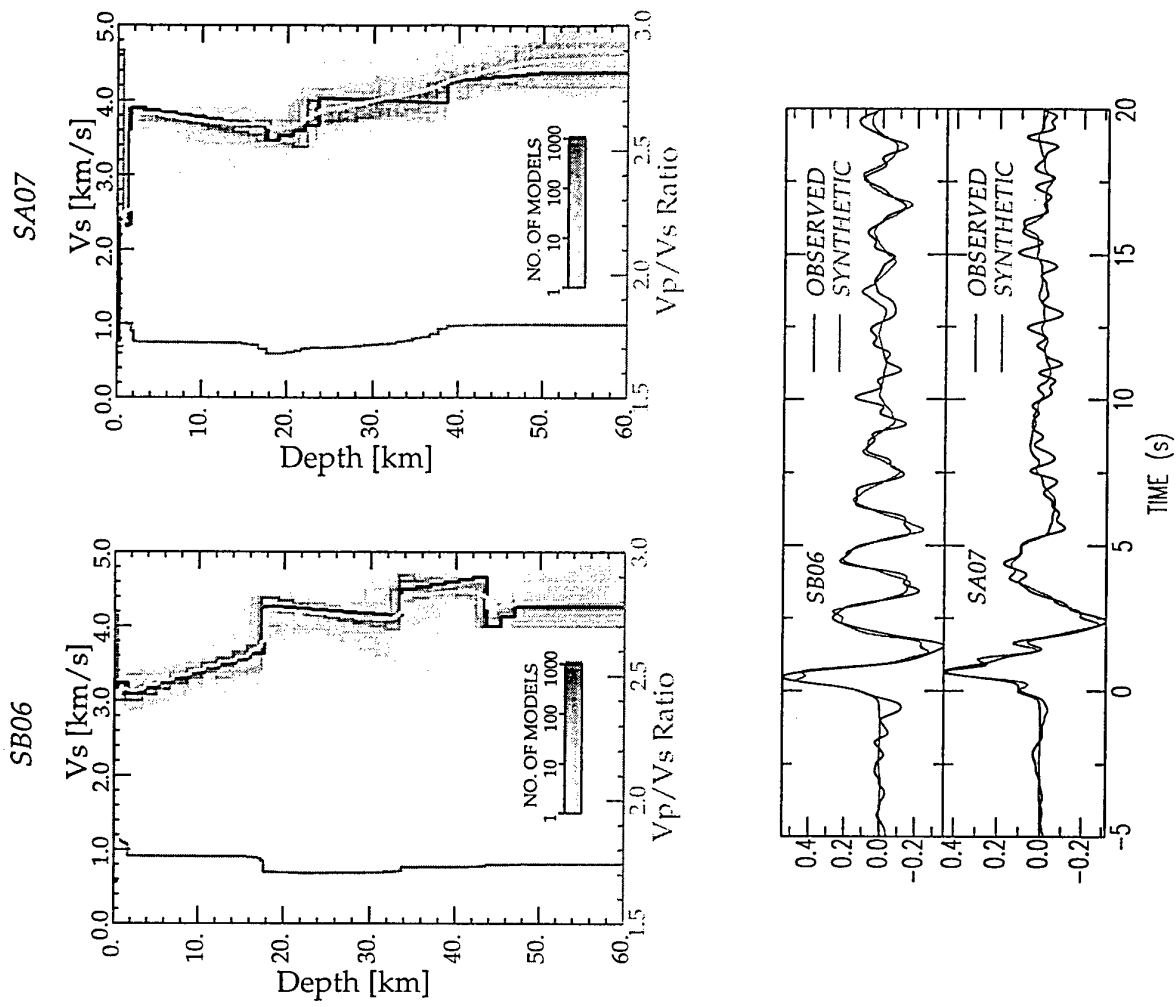


fig 9

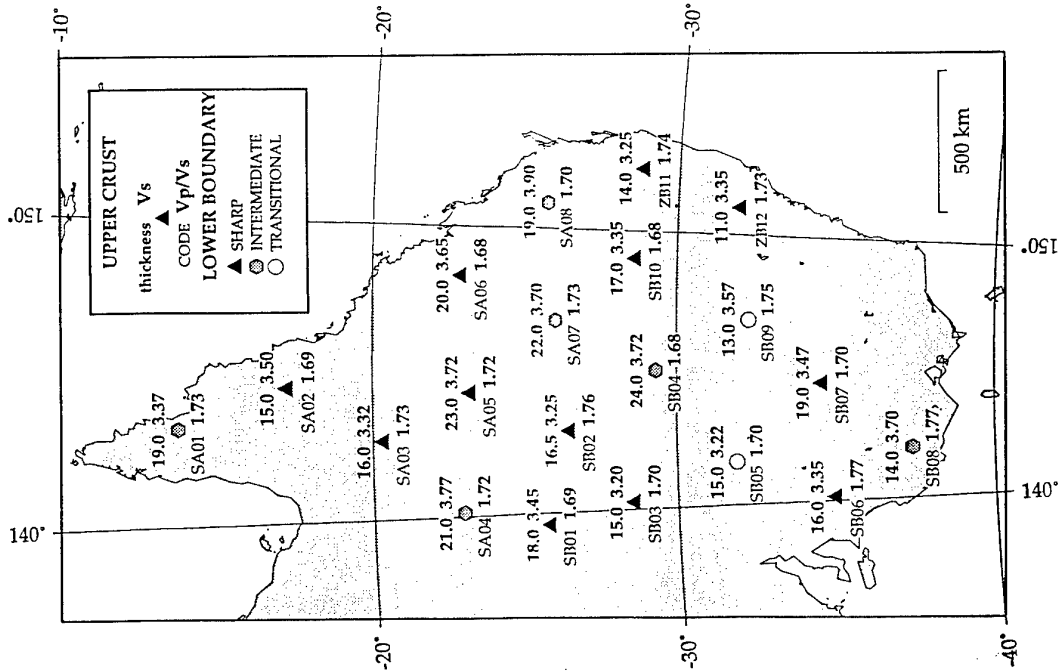


fig 10.

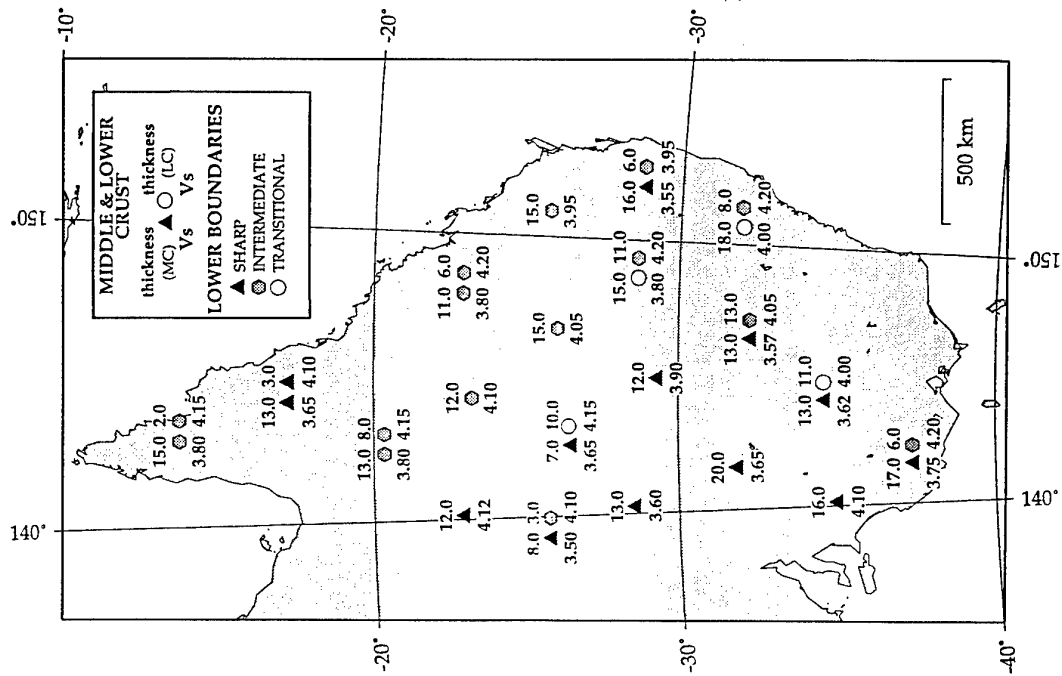


fig 11.

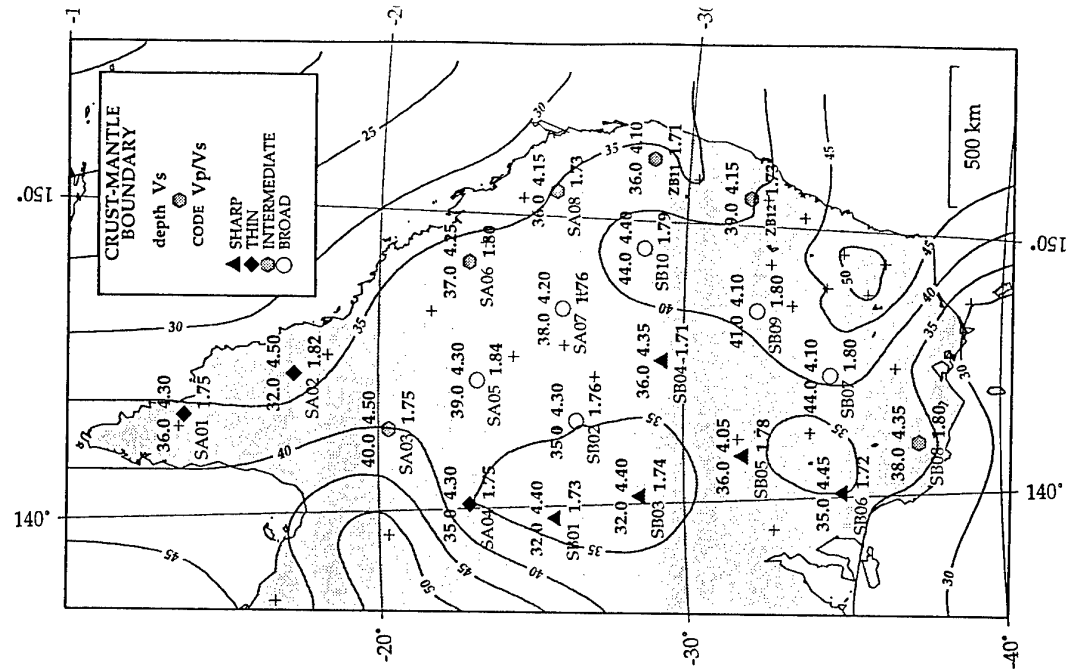


fig 12.

Part II: Upper mantle heterogeneities in the Indian Ocean from waveform inversion.

Upper mantle heterogeneities in the Indian Ocean from waveform inversion

Debayle E.¹ and Lévêque J.J.

Institut de Physique du Globe de Strasbourg, (CNRS and Université Louis Pasteur), France

Abstract. A waveform inversion method is applied to 156 Love and Rayleigh wave seismograms to build up a 3-D model of the shear velocity in the upper mantle beneath the Indian Ocean. The first step of the method consists in finding, for each path, a radially stratified upper mantle model compatible with the Love and Rayleigh wave seismograms relative to that path. The fundamental mode and few higher modes are modelled in the waveform inversion. In a second step, the models related to the different paths are used in a tomographic inversion to map the 3-D upper mantle structure. The 3-D velocity model has a lateral resolution of 1000 km. No significant velocity anomalies are found below 300 km, although the resolution is still good. Continental roots are confined to the upper 300 km and low velocities below mid-oceanic ridges to the upper 250 km, depending on their spreading rates. At shallow depths (< 80 km), we find a positive velocity anomaly beneath the West Indian ridge near the Rodriguez triple junction, where gravimetric and bathymetric data indicate a reduced volcanic activity. At greater depth (around 200 km), a low velocity signature is found beneath the hot-spot of Réunion-Mauritius islands and the Central Indian ridge. It could reflect a real connection between the two structures.

1. Introduction

During the past 15 years, long period surface waves have been commonly used to image the structure of the upper mantle. Due to the increasing amount of digital data, the lateral dimensions of structural features that can be resolved in global S velocity models have progressively decreased from 5000 km [Woodhouse and Dziewonski, 1984] to around 1000 km [Zhang and Tanimoto, 1993]. In regional studies, lateral resolution can now reach locally 250 km in regions where a dense coverage is available [Zielhuis and van der Hilst, 1996]. In the Indian Ocean, the previous regional studies [Montagner, 1986a;b; Roult *et al.*, 1987; Montagner and Jobert, 1988] have a lateral resolution limited to 2000 km, due to the poor distribution of stations. These latter studies, based on the analysis of fundamental mode dispersion curves, show a good correlation of the deep structure with surface tectonics down to about 100 km depth, except in the Central part of the Southeast Indian Ridge. In addition, Montagner [1986a;b] and Montagner and Jobert [1988] find a slow structure shifted eastward of the Central Indian ridge below 100 km depth.

In this paper, we present a 3-D S-velocity model for

the upper mantle in the Indian Ocean with improved lateral and depth resolution. The model is obtained from a larger dataset than in previous studies and a different methodological approach. New data recorded on Géoscope stations DRV, CRZ and HYB allow us to improve the lateral resolution to 1000 km with a more homogeneous path coverage. Instead of analysing dispersion curves, we use a waveform inversion method designed to match directly surface-wave seismograms, possibly including several higher modes. It is based on the waveform inversion technique of *Cara and Lévêque* [1987] adapted to process simultaneously a set of seismograms with close epicenters, recorded at a single station. In this approach called "multi-seismogram technique", the epicenters of a given cluster must be close enough so that we can consider the waves travel the same path and can be explained with a single model. The inverted model, compatible with all the observed seismograms available for that path, can be interpreted as the average Earth's structure beneath the path. A regionalization of the models obtained for the different paths leads to tomographic images of the upper mantle.

2. Data Selection

We use Love and Rayleigh wave long-period seismograms at 11 stations in the Indian Ocean, for earthquakes occurring from 1988 to 1994. The selected events have magnitudes ranging from 4.8 to 7.2 Msz and the corresponding seismograms are inverted using observables covering the 20-300 s period range. Most of these earthquakes are shallow events located on mid-oceanic ridges of the Indian Ocean. The few deep earthquakes we use are located in the Indonesian subduction zone. We have discarded seismograms with a poor signal-to-noise ratio or for which the initial phase at the source was not stable with respect to small perturbations of the path azimuth. Finally, we keep only the paths for which at least one Rayleigh wave and one Love wave seismograms can be inverted simultaneously. For some paths, up to 4 seismograms (2R+2L) have been inverted simultaneously. The whole set of data consists of 156 seismograms related to 71 different paths. For 11 of these paths, higher modes are taken into account up to the fifth overtone for Rayleigh waves. Love wave higher modes are included in the inversion for 53 paths. The path coverage is shown on Fig.1a.

Fig.1a

3. Method

3.1. The Waveform Fitting

One important problem in a waveform inversion technique is the highly non-linear dependence of the recorded signal on the model parameters. The originality of the method developed by *Cara and Lévêque* [1987], compared with other waveform inversion techniques [e.g. *Nolet*, 1990], is the introduction of secondary observables, built up from the seismograms, having only a

slightly non-linear dependence upon the model parameters, allowing for an inversion with a classical non-linear scheme. In the multi-seismogram approach used here, the secondary observables are computed for all seismograms related to a same path, and then inverted using the same scheme as in *Cara and L  v  que* [1987].

Using several seismograms simultaneously in one inversion reduces the influence of errors on fixed parameters, such as focal mechanism or focal depth, and allows to use simultaneously data containing non-redundant information on the mantle structure. For example, we can invert simultaneously data from shallow and deep earthquakes as in *Stutzmann and Montagner* [1993], or data from Love and Rayleigh waves.

In most cases, Love and Rayleigh waves are not compatible with a single isotropic structure. We address this Love/Rayleigh discrepancy by inverting for the S-wave anisotropic parameter ξ as defined in *Takeuchi and Saito* [1972] for a transversely isotropic medium. We also invert for the shear wave velocity β_v , the attenuation factor Q_β^{-1} and for M_0 , the scalar seismic moment of the source, to ensure an adequate scaling of the signal. In this paper, we present and discuss results on β_v only. Significant anisotropy is found in the upper 250-300 km, but the trade-off between β_v and ξ is found very small. Results on anisotropy and Q_β^{-1} will be discussed in a separate paper.

The a priori information used in this study is similar to the one used in *L  v  que et al.* [1991]: the a priori β_v model in particular is a smoothly depth-varying isotropic model in the mantle with a crustal structure adapted for each path. The a priori standard-deviations are fixed to 0.05 km/s for β_v and 0.03 for ξ according to the expected variation range for these parameters in the Indian Ocean. The vertical correlation length is fixed to 50 km and the uncertainty on the data to 10 % for amplitude data, and 5 % for phase data.

3.2. Regionalization of Shear Velocities

The average β_v models are obtained for each path shown in Fig.1a. A regionalization of these models is performed using the continuous regionalization algorithm of *Montagner* [1986a]. To constrain the lateral smoothness of the model and according to our path coverage, we use gaussian functions with length of 1000 km as correlation functions. The a priori standard deviation which controls the amplitude of heterogeneities in the inverted model is set to 0.10 km/s. This value allows velocity contrasts in the final model as large as 15 %, in agreement with velocity contrasts observed in previous oceanic studies [e.g. *Montagner*, 1986a;b or *Nishimura and Forsyth* 1989].

The S-velocity map at 50 km depth and an East-West cross section at latitude 20  S are shown on Fig.1, together with the corresponding a posteriori error maps (Fig.1a,b). Dark blue areas indicate an a posteriori error close to the a priori error (0.1 km/s), indicating a total lack of resolution. This unresolved area is limited

to the outer zone of the map. In most part of the Indian Ocean, and at least down to 300 km depth, the error is less than 0.05 km/s, indicating a very good resolution. Below 300 km depth (Fig.1b), we still observe locally an error smaller than 0.05 km/s in two regions, one located below the Central Indian ridge ($60^{\circ}E$), and the other one around $110^{\circ}E$. They correspond to areas where the paths associated to deep events in the eastern part of the Indonesian subduction zone cross the latitude $20^{\circ}S$. This is a direct consequence of the increased resolution for these paths, as compared with paths where no higher mode data were available.

At 50 km depth (Fig.1c), S-velocities are strongly correlated to surface tectonics. Low velocities are associated with mid-oceanic ridges. Old oceanic basins display high velocities. Two unexpected features however show up in the well resolved area: a positive anomaly beneath the West Indian ridge, near the Rodriguez triple junction, and high velocities beneath the Carlsberg ridge. On the cross-section at latitude $20^{\circ}S$ (Fig.1d), fast S-velocities are found down to 250 km below Africa and down to 300 km below Australia. The low velocity signature of the Central Indian ridge does not extend beyond 250 km depth. This is probably a reliable feature in the model since the resolution is good in this area (Fig.1a). Below 300 km, the amplitude of the anomalies remains small everywhere. Note also that the low velocity beneath the island of Madagascar can be an artefact due to a poor knowledge of the crustal structure in this region; this negative anomaly does not extend deeper than 50 km.

Figure 2 displays the velocity maps at increasing depths, showing that features observed on the $20^{\circ}S$ cross-section are more general. The correlation with surface tectonics is still very clear at 88 and 140 km depth. At 88 km, a positive velocity contrast is present beneath the West Indian ridge near the Rodriguez triple junction. At 140 km depth, this positive contrast disappears and the slow signature of the West Indian ridge itself vanishes while it remains beneath the two other ridges. At 190 km depth, low velocities beneath mid-oceanic ridges and the Indonesian arc nearly disappear. At this depth, the largest negative anomaly is centered on the Central Indian ridge, close to Mauritius and La Réunion islands. High velocities are still present beneath continents, and a north-south positive anomaly connects the Australian continent to Antarctica. At 268 km, the low velocity signature of the ridge completely vanishes, but the high velocity pattern is similar to that found at 190 km depth, although if attenuated.

Figure 2

4. Discussion

The depth extent of the seismic anomalies we have found (Fig.1d,2c) is slightly shallower than in most other surface wave studies of the Indian Ocean [e.g. *Montagner and Tanimoto*, 1991]. These observations agree with a more recent global S-velocity model [*J. Woodhouse and J. Trampert*, submitted to Earth Planet.

Sci. Lett., 1996] and support the idea developed in *Ricard et al.* [1996] that most seismological observations are compatible with the 3-SMAC "geodynamical" model where upper mantle anomalies are no deeper than 300 km. However, in our model, the low-velocity signature beneath mid-oceanic ridges is apparent down to 200 km in the most part of the Indian Ocean (Fig. 2c,d), a greater value than in 3-SMAC where ridge anomalies are present in the first 100 km only.

Despite the enhanced lateral resolution of our study, no eastward shift is observed at any depth beneath the Central Indian ridge: we find low velocities in the Central Indian basin at 190 km depth as in *Montagner* [1986a;b] or *Montagner and Jobert* [1988] but the strongest velocity anomaly is well centered beneath the Central Indian ridge (Fig.2). Another feature, more classical [e.g. *Montagner and Tanimoto*, 1991], of our model is the correlation between the low velocity signature of oceanic ridges and their spreading rates.

At shallow depths, we find a positive anomaly that does not appear in previous 3D S-velocity models beneath the West Indian ridge near the Rodriguez triple junction, suggesting a relatively cold mantle in that part of the ridge (Fig.1c,2a). This can be related to recent bathymetric [*Mendel and Sauter*, 1996] and gravimetric [*Rommevaux et al.*, submitted to Marine Geophys. Res., 1996] results that conclude to a weak volcanic activity between the fracture zone of Melville (around 60°E) and the Rodriguez triple junction. It could also help explaining the high phase velocities obtained at this location by *Roult et al.* [1987] for Rayleigh waves at periods 61s and 102s. Another interesting new feature is the deep low velocity anomaly that persists to 190 km depth beneath the Central Indian ridge, and spreads toward the hot-spot of Réunion-Mauritius islands. This westward spreading is also apparent on the cross-section (Fig.1d) and at shallower depth (88 and 140 km, Fig.2a,b) beneath the Mascareignes plateau. Due to a lack of lateral resolution, this low velocity anomaly could be the coalescence of two distinct anomalies beneath the hot-spot of Réunion-Mauritius islands and beneath the Central Indian ridge. Another possible interpretation is to associate this low velocity signature with the hot-spot trace between the Central Indian ridge and Mauritius island. The well-known Australian-Antarctic discordance appears clearly on our maps at all depths as a structure abnormally fast for a ridge (Fig.2). This result is in agreement with those of *Forsyth et al.* [1987], who found high S velocities down to 150 km depth, and *Kuo et al.* [1996] who favour a deep asthenospheric origin of the AAD from considerations on the geoid. The oceanic plateaus, which are one of the striking characteristics of the Indian Ocean, do not systematically correspond to clear velocity anomalies. This may be due to the fact that some of these structures (e.g. Ninety-east and Broken ridges) are much narrower than the lateral resolution or, where the plateau structure is larger (Kerguelen), to the poor path coverage near the border of our maps.

Acknowledgments.

We thank IRIS and G  oscope teams for providing seismological data, and J.P. Montagner for providing us his continuous regionalisation algorithm. The figures have been made with the GMT software.

References

- Cara, M., and J.J. L  v  que, Waveform inversion using secondary observables, *Geophys. Res. Lett.*, *14*, 1046-1049, 1987.
- Forsyth, D. W., R. L. Ehrenbard and S. Chapin, Anomalous upper mantle beneath the Australian-Antarctic discordance, *Earth Planet. Sci. Lett.*, *84*, 471-478, 1987.
- Kuo, B. Y., C. H. Chen, and Y. S. Zhang, A fast velocity anomaly to the west of the Australian-Antarctic Discordance, *Geophys. Res. Lett.*, *23*, 2239-2242, 1996.
- L  v  que, J.J., M. Cara, and D. Rouland, Waveform inversion of surface wave data: test of a new tool for systematic investigation of upper mantle structures, *Geophys. J. Int.*, *104*, 565-581, 1991.
- Mendel, V. and D. Sauter, Seamount volcanism at the super slow-spreading southwest Indian Ridge between 57  E and 70  E, *Geology*, *in press*, 1996.
- Montagner, J.P., Regional three-dimensional structures using long-period surface waves, *Ann. Geophys.*, *4*, 283-294, 1986a.
- Montagner, J.P., Three-dimensional structure of the Indian Ocean inferred from long-period surface waves, *Geophys. Res. Lett.*, *13*, 315-318, 1986b.
- Montagner, J.P., and N. Jobert, Vectorial tomography, 2, Application to the Indian Ocean, *Geophys. J. R. astr. Soc.*, *94*, 309-344, 1988.
- Montagner, J.P., and T. Tanimoto, Global upper mantle tomography of seismic velocities and anisotropies, *J. Geophys. Res.*, *96*, 20337-20351, 1991.
- Nishimura, C. E., and D. W. Forsyth, The anisotropic structure of the upper mantle in the Pacific, *Geophys. J.*, *96*, 203-229, 1989.
- Nolet, G., Partitioned waveform inversion and two dimensional structure under the network of autonomously recording seismographs, *J. Geophys. Res.*, *95*, 8499-8512, 1990.
- Ricard, Y., H.C. Nataf, and J.P. Montagner, The three-dimensional seismological model a priori constrained: Confrontation with Seismic Data, *J. Geophys. Res.*, *101*, 8457-8472, 1995.
- Roult, G., D. Rouland, and J.P. Montagner, Velocity distribution in the Indian Ocean and Indonesian region inferred from G  oscope records, *Geophys. Res. Lett.*, *14*, 343-346, 1987.
- Stutzmann, E., and J.P. Montagner, An inverse technique for retrieving higher mode phase velocity and mantle structure, *Geophys. J. Int.*, *113*, 669-683, 1993.
- Takeuchi, H., and M. Saito, Seismic surface waves, in *Methods in Computational Physics*, *11*, edited by B. A. Bolt, pp.217-295, Academic Press, New-York, 1972.
- Woodhouse, J. H., and A. M. Dziewonski, Mapping the upper mantle: Three dimensional modelling of Earth structure by inversion of seismic waveform, *J. Geophys. Res.*, *89*, 5953-5986, 1984.
- Zhang, Y. S. and T. Tanimoto, High-resolution global upper

mantle structure and plate tectonics, *J. Geophys. Res.*, **98**, 9793-9823, 1993.

Zielhuis, A. and R. D. van der Hilst, Upper-mantle shear velocity beneath eastern Australia from inversion of waveforms from SKIPPY portable arrays, *Geophys. J. Int.*, **127**, 1-16, 1996.

E. Debayle, Research School of Earth Sciences, Australian National University, Canberra ACT 0200, Australia (e-mail: eric@rses.anu.edu.au)

J.J. L  v  que, Institut de Physique du Globe de Strasbourg 5 rue Ren   Descartes, 67084 Strasbourg Cedex, France (e-mail: leveque@sismo.u-strasbg.fr)

(Received June 6, 1996; revised December 12, 1996; accepted December 13, 1996.)

¹Now at Research School of Earth Sciences, Australian National University, Canberra, ACT 0200, Australia.

Figure 1. a) A posteriori error map (in km/s) at 50 km depth and path coverage. b) vertical East-West cross-section at $20^{\circ}S$ in the 3-D error model. c) Map of lateral perturbations in percent (with respect to the value V_{ref} indicated on the map) for the S-velocity at 50 km depth. d) vertical East-West cross-section at $20^{\circ}S$ in the 3-D S-velocity model. The oceanic ridges of the Indian Ocean are plotted in green on the maps.

Figure 1. a) A posteriori error map (in km/s) at 50 km depth and path coverage. b) vertical East-West cross-section at $20^{\circ}S$ in the 3-D error model. c) Map of lateral perturbations in percent (with respect to the value V_{ref} indicated on the map) for the S-velocity at 50 km depth. d) vertical East-West cross-section at $20^{\circ}S$ in the 3-D S-velocity model. The oceanic ridges of the Indian Ocean are plotted in green on the maps.

Figure 2. Maps of lateral perturbations for the S-velocity in the Indian Ocean at increasing depths. The variations are given in percents with respect to the value V_{ref} indicated on each map a) depth 88 km. b) depth 140 km. c) depth 190 km. d) depth 268 km.

Figure 2. Maps of lateral perturbations for the S-velocity in the Indian Ocean at increasing depths. The variations are given in percents with respect to the value V_{ref} indicated on each map a) depth 88 km. b) depth 140 km. c) depth 190 km. d) depth 268 km.

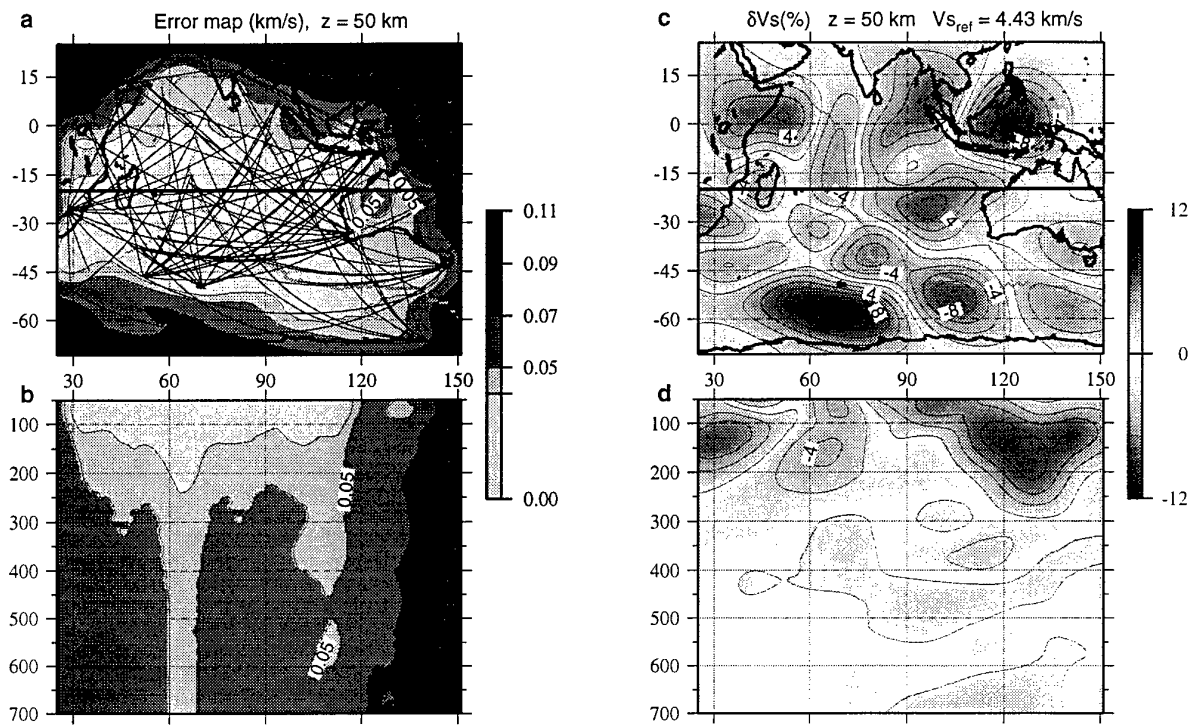


Figure 1

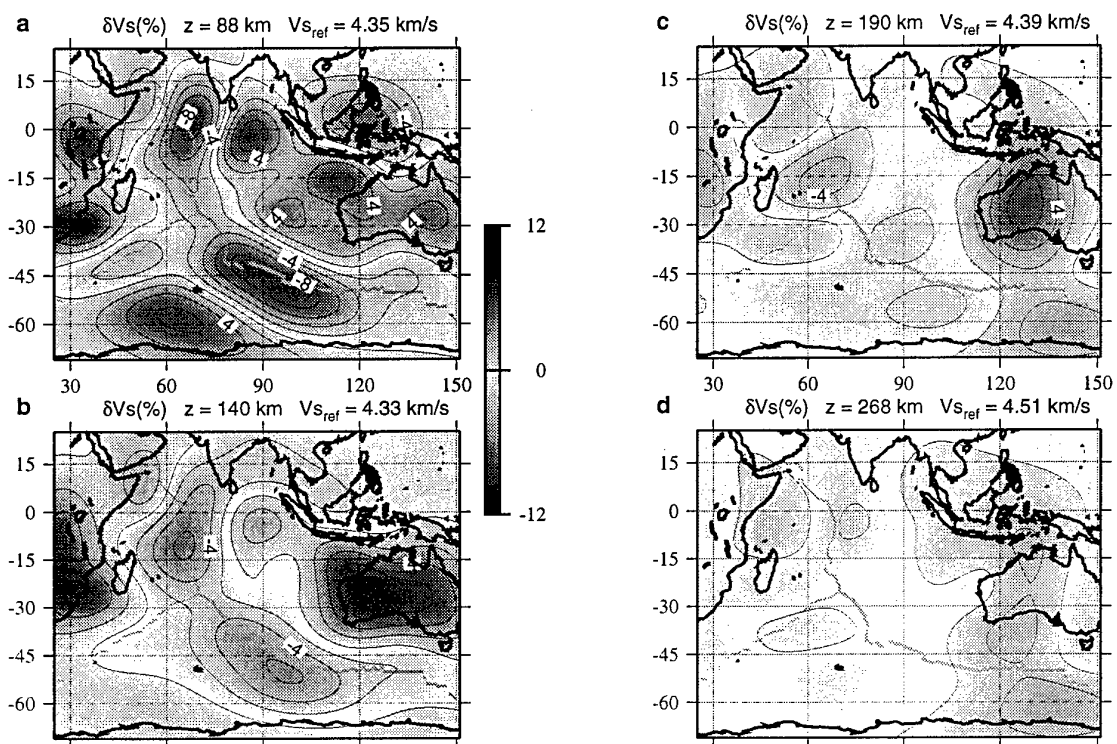


Figure 2

Part III: Guided waves in 3-dimensional structures

Guided waves in 3-dimensional structures

B.L.N. Kennett

Research School of Earth Sciences, Australian National University, Canberra ACT 0200, Australia

SUMMARY

A new formulation for the propagation of surface waves in three-dimensionally varying media is developed in terms of modal interactions. For anisotropic models, with allowance for attenuation, the treatment leads to a set of coupled partial differential equations for the weight functions for different modal contributions. A variety of assumptions can be made about the nature of the modal field: a single set of reference modes, a set of local modes for the structure beneath a point, or a set of local modes for a laterally varying reference structure. Each modal contribution is represented locally as an angular spectrum of plane waves and the influence of three-dimensional structure is included by allowing coupling between different modal branches and propagation directions. The representation of the guided wave field requires the inclusion of a full set of modes, so that, even for isotropic models, both Love and Rayleigh modes appear as different polarisation states of the modal spectrum. The coupling equations describe the interaction between the different polarisations induced by the presence of the three-dimensional structure.

The level of lateral variation within the three-dimensional model is not required to be small. Horizontal refraction or reflection of the surface wave field can be included by allowing for transfer between modes travelling in different directions. Approximate forms of the coupled equation system can be employed when the level of heterogeneity is small, for example the coupling between the fundamental mode and higher modes can often be neglected, or forward propagation can be emphasised by restricting the range of angular interaction.

Key words: surface waves, 3-D structure, anisotropy

2 B.L.N. Kennett

1 INTRODUCTION

Surface waves form a very prominent part of the recorded seismogram and in consequence it is desirable to be able to describe the behaviour of this part of the seismic wavefield as it interacts with three-dimensional structure.

Most studies of surface wave propagation in heterogeneous media have started from the properties of a stratified medium. For slowly varying layered media, Woodhouse (1974) showed that the dispersion and trajectory of an individual mode could be described by using ray theory where the local phase velocity and the depth dependence of the displacement match that of a stratified medium with the structure beneath a point on the ray path. In this adiabatic mode description there is no interaction between different modes, though the patterns of propagation can vary according to the nature of the modal dispersion. Woodhouse & Wong (1986) extended the ray approach to include longer period normal modes with a partial allowance for amplitude effects along the ray path.

More complex structure can be included in a normal mode description by allowing for coupling between modes. Such coupling between neighbouring multiplets along a mode branch has been considered by a number of authors (see e.g. Park 1987, Romanowicz 1987, Tsuboi & Geller 1989). The computational requirements for including coupling between normal-mode branches are more severe but Yu & Park (1993) have included the effects of anisotropy at long periods with limited cross-branch coupling.

Tanimoto (1990) discussed the influence of significant lateral variations in phase velocity for fundamental mode Love and Rayleigh waves propagating from the Whittier Narrows earthquake to stations in Northern California. His work was based on an approximate representation of the surface waves using a finite difference representation of the phase behaviour.

A more complete analysis requires the inclusion of coupling between mode branches. For 2-D structures Kennett (1984) introduced a description of the wavefield in terms of the modes of a fixed reference structure, and Maupin & Kennett (1987) analysed the influence of the truncation of modal expansions. Maupin (1988) introduced an alternative treatment for 2-D structures in which the expansion of the wavefield was made in terms of the local modes of the structure, with an allowance for coupling induced by the gradients in material properties. Maupin (1992) extended the coupled mode treatment to handle ducted three-dimensional surface propagation along 2-D structures. A partial extension of Maupin's (1988) results to the 3-D case was made by Tromp (1994) who concentrated on mode conversions occurring along a given surface wave trajectory.

An approximate formulation for 3-D problems has been presented by Snieder (1986a,b), Snieder & Nole (1987) using a scattering development based on a first-order Born approximation using the modes of a fixed reference structure. This approach is able to account for changes in the direction of surface waves as well as inter-mode coupling induced by heterogeneity. The use of first-order scattering theory restricts the validity

of the approximation to situations where the perturbation to the reference wavefield induced by the presence of heterogeneity is small. This approach is therefore suitable for localised moderate heterogeneity or to very weak heterogeneity extending over a broad area.

An alternative approach for the 3-D case has been suggested by Bostock (1992) for the restricted situation where the pattern of heterogeneity can be represented in terms of radial variation about a source point modulated by an angular spectrum. The structure of the resulting coupled equations for the modal coefficients is very similar to that in Kennett's (1984) treatment of 2-dimensional problems.

Here we present a new formulation of the propagation of surface waves in three-dimensionally varying media which leads to a set of coupled partial differential equations for the weight functions for different modal contributions in an anisotropic model, including the effects of attenuation. The basic equations can then be used with a variety of different assumptions about the nature of the modal field e.g. the use of a single set of reference modes as in the 2-D work of Kennett (1984), local modes as employed by Maupin (1988, 1992), or a set of local modes for a laterally varying reference structure. Each modal contribution is represented locally as an angular spectrum of plane waves and the influence of the three-dimensional structure is included by allowing coupling between different modal branches and propagation directions. The representation of the guided wave field requires the inclusion of the full set of modes, so that, even for isotropic models, both Love and Rayleigh modes appear as different polarisation states of the modal spectrum. The coupling equations describe the interaction between the different polarisations induced by the presence of the three-dimensional structure.

The level of lateral variation within the three-dimensional model is not restricted to be small and horizontal refraction or reflection of the surface wave field is included by allowing for transfer between modes travelling in different directions. When the level of heterogeneity is small the complexity of the coupled equation system can be reduced by suitable approximations. For example, interactions between the fundamental modes and higher modes can be neglected, or the range of angular interaction can be restricted to emphasise forward propagation.

2 MODAL EVOLUTION EQUATIONS

The methods developed by Kennett (1984) and Maupin (1988, 1992) were based on writing the equations of motion and stress-strain relations for seismic waves in a form where a single horizontal coordinate is given a preferred status. A set of coupled partial differential equations can be constructed, for the components of displacement and the traction in the preferred direction. Derivatives with respect to the preferred coordinate are restricted to first order only and can be separated from the remaining terms in which derivatives with respect to the other spatial coordinates and time appear. This approach is well suited to models in which the structure is two-dimensional. Kennett

(1984) has shown how some measure of three-dimensional effects can be included under the assumption that the propagation path is not significantly perturbed from the direct path from source to receiver. However, this type of approach cannot readily be extended to general three-dimensional variation in structure.

For surface waves in a three-dimensionally varying structure we have to be able to describe processes in which the direction of propagation of the wavefield varies spatially. We therefore need a representation of seismic wave propagation in which the action of the gradient in the horizontal plane is emphasised. A suitable form of equations can be found which depend only on first order derivatives of displacement and traction with respect to the horizontal spatial coordinates, and for which only the vertical derivatives of the seismic parameters are required. There is some resemblance between these equations for the three-dimensional case and those previously derived for the two-dimensional situation by Kennett (1984) which can be used to guide a development in which the displacement and traction fields for the guided waves are represented as a sum of modal contributions with spatially varying weighting coefficients.

2.1 Coupled equations for displacement and horizontal tractions

We work in a cartesian coordinate system with the $x_3(z)$ coordinate directed downwards and will emphasise propagation in the horizontal plane by introducing the horizontal coordinate \mathbf{x}_1 and horizontal gradient ∇_1 with components

$$\mathbf{x}_1 = \begin{pmatrix} x_1 \\ x_2 \end{pmatrix}, \quad \nabla_1 = \begin{pmatrix} \partial/\partial x_1 \\ \partial/\partial x_2 \end{pmatrix}. \quad (2.1.1)$$

We will employ roman subscripts i, j, k, l for unrestricted coordinates and greek subscripts when attention is restricted to the horizontal coordinates, e.g.

$$(\mathbf{x}_1)_\alpha = x_\alpha, \quad (\nabla_1)_\alpha = \partial_\alpha, \quad \alpha = 1, 2 \quad (2.1.2)$$

where we have written ∂_1 for $\partial/\partial x_1$. We use the convention of summation over repeated greek suffices and over the suffices i, j, k, l .

We consider a seismic wavefield with displacement \mathbf{u} , stress tensor τ_{ij} and elastic moduli c_{ijkl} . We will concentrate on time-harmonic wavefields with angular frequency ω , and can allow for attenuation by adopting complex moduli at each frequency.

Following Woodhouse (1974) we introduce the elastic moduli matrices C_{ij} such that

$$(C_{ij})_{kl} = c_{klij} = c_{kjli}. \quad (2.1.3)$$

Then the stress-strain relation

$$\tau_{ij} = c_{ijkl} \partial_k u_l, \quad (2.1.4)$$

can be written in terms of traction vectors τ_i with components $(\tau_i)_j = \tau_{ij}$, in the form

$$\tau_i = C_{ij} \partial_j \mathbf{u}. \quad (2.1.5)$$

When we separate out the dependence of the tractions on the horizontal coordinates we obtain

$$\tau_\alpha = C_{\alpha\beta}\partial_\beta \mathbf{u} + C_{\alpha 3}\partial_3 \mathbf{u}, \quad (2.1.6)$$

$$\tau_3 = C_{3\beta}\partial_\beta \mathbf{u} + C_{33}\partial_3 \mathbf{u}. \quad (2.1.7)$$

The equation of motion, in the absence of sources, can be written as

$$\partial_\alpha \tau_\alpha + \partial_3 \tau_3 = -\rho \omega^2 \mathbf{u}. \quad (2.1.8)$$

If we isolate horizontal derivatives on the left hand side

$$\partial_1 \tau_1 + \partial_2 \tau_2 = \partial_\alpha \tau_\alpha = -\rho \omega^2 \mathbf{u} - \partial_3 \tau_3, \quad (2.1.9)$$

and we can express τ_3 in terms of displacement derivatives using (2.1.7) above.

Our aim is to keep all derivatives with respect to the horizontal coordinates on the left hand side of the equations so that we need to find expressions for $\partial_1 \mathbf{u}$, $\partial_2 \mathbf{u}$. From the definitions of the tractions τ_1 , τ_2 we have

$$C_{11}\partial_1 \mathbf{u} + C_{12}\partial_2 \mathbf{u} = \tau_1 - C_{13}\partial_3 \mathbf{u}, \quad (2.1.10)$$

$$C_{21}\partial_1 \mathbf{u} + C_{22}\partial_2 \mathbf{u} = \tau_2 - C_{23}\partial_3 \mathbf{u}. \quad (2.1.11)$$

We can write these two equations in a matrix form

$$\begin{pmatrix} C_{11} & C_{12} \\ C_{21} & C_{22} \end{pmatrix} \begin{pmatrix} \partial_1 \mathbf{u} \\ \partial_2 \mathbf{u} \end{pmatrix} = \begin{pmatrix} \tau_1 - C_{13}\partial_3 \mathbf{u} \\ \tau_2 - C_{23}\partial_3 \mathbf{u} \end{pmatrix}, \quad (2.1.12)$$

and then can recover suitable expressions for $\partial_1 \mathbf{u}$, $\partial_2 \mathbf{u}$ by inverting the matrix of moduli terms, which can be achieved using results for partitioned matrices. We define

$$Q_1 = I_3 - C_{12}C_{22}^{-1}C_{21}C_{11}^{-1}, \quad (2.1.13)$$

$$Q_2 = I_3 - C_{21}C_{11}^{-1}C_{12}C_{22}^{-1}, \quad (2.1.14)$$

where I_3 is the 3×3 identity matrix. Then we can write the required inverse in the form

$$\begin{pmatrix} C_{11} & C_{12} \\ C_{21} & C_{22} \end{pmatrix}^{-1} = \begin{pmatrix} C_{11}^{-1}Q_1^{-1} & -C_{11}^{-1}C_{12}C_{22}^{-1}Q_2^{-1} \\ -C_{22}^{-1}C_{21}C_{11}^{-1}Q_1^{-1} & C_{22}^{-1}Q_2^{-1} \end{pmatrix}, \quad (2.1.15)$$

This representation allows the inverse to be constructed using C_{11}^{-1} , C_{22}^{-1} and the combinations $C_{21}C_{11}^{-1}$, $C_{12}C_{22}^{-1}$.

The horizontal derivatives of the displacement can thus be extracted as

$$\partial_1 \mathbf{u} = -V_{13}\partial_3 \mathbf{u} + C_{11}^{-1}Q_1^{-1}\tau_1 - C_{11}^{-1}C_{12}C_{22}^{-1}Q_2^{-1}\tau_2, \quad (2.1.16)$$

$$\partial_2 \mathbf{u} = -V_{23}\partial_3 \mathbf{u} - C_{22}^{-1}C_{21}C_{11}^{-1}Q_1^{-1}\tau_1 + C_{22}^{-1}Q_2^{-1}\tau_2, \quad (2.1.17)$$

where

$$V_{13} = C_{11}^{-1}[Q_1^{-1}C_{13} - C_{12}C_{22}^{-1}Q_2^{-1}C_{23}], \quad (2.1.18)$$

$$V_{23} = C_{22}^{-1}[Q_2^{-1}C_{23} - C_{21}C_{11}^{-1}Q_1^{-1}C_{13}]. \quad (2.1.19)$$

We can derive an evolution equation for the horizontal tractions from the equation of motion in the form (2.1.9) if we can represent the vertical traction τ_3 in terms of τ_1 and τ_2 . From the definition of the traction vector

$$\tau_3 = C_{31}\partial_1 \mathbf{u} + C_{32}\partial_2 \mathbf{u} + C_{33}\partial_3 \mathbf{u}. \quad (2.1.20)$$

On substituting for the horizontal derivatives of the displacement field from (2.1.16), (2.1.17) we obtain the vertical traction in the form

$$\begin{aligned} \tau_3 = & (C_{33} - C_{31}V_{13} - C_{32}V_{23})\partial_3 \mathbf{u} \\ & + (C_{31} - C_{32}C_{22}^{-1}C_{21})C_{11}^{-1}Q_1^{-1}\tau_1 + (C_{32} - C_{31}C_{11}^{-1}C_{12})C_{22}^{-1}Q_2^{-1}\tau_2. \end{aligned} \quad (2.1.21)$$

The horizontal divergence of the traction field can therefore be expressed in a form in which only x_3 derivatives act on the material properties

$$\begin{aligned} \partial_1 \tau_1 + \partial_2 \tau_2 = & -\rho \omega^2 \mathbf{u} - \partial_3 [(C_{33} - C_{31}V_{13} - C_{32}V_{23})\partial_3 \mathbf{u}] \\ & - \partial_3 [(C_{31} - C_{32}C_{22}^{-1}C_{21})C_{11}^{-1}Q_1^{-1}\tau_1] \\ & - \partial_3 [(C_{32} - C_{31}C_{11}^{-1}C_{12})C_{22}^{-1}Q_2^{-1}\tau_2]. \end{aligned} \quad (2.1.22)$$

The set of equations (2.1.16), (2.1.17) for the horizontal gradients of the displacement vector and (2.1.22) for the divergence of the horizontal traction constitute the coupled equations we are seeking for the horizontal evolution of the displacement and traction fields. No horizontal derivatives of seismic parameters appear on the right hand side of these equations, the presence of vertical derivatives mean that the equations must be viewed in a distributional sense in the presence of any material interfaces.

We can rewrite the equations in a form which displays the derivatives with respect to x_3 explicitly:

$$\begin{aligned} \partial_1 \mathbf{u} &= \mathcal{A}_{1u}^1 \partial_3 \mathbf{u} + \mathcal{A}_{1\tau}^1 \tau_1 + \mathcal{A}_{1\tau}^2 \tau_2, \\ \partial_2 \mathbf{u} &= \mathcal{A}_{2u}^2 \partial_3 \mathbf{u} + \mathcal{A}_{2\tau}^1 \tau_1 + \mathcal{A}_{2\tau}^2 \tau_2, \end{aligned} \quad (2.1.23)$$

$$\partial_1 \tau_1 + \partial_2 \tau_2 = -\rho \omega^2 \mathbf{u} - \partial_3 [\mathcal{A}_{1\tau}^1 \tau_1 + \mathcal{A}_{1\tau}^2 \tau_2],$$

in terms of a set of operators

$$\begin{aligned} \mathcal{A}_{1u}^1 &= -V_{13}, \\ \mathcal{A}_{2u}^2 &= -V_{23}, \\ \mathcal{A}_{1\tau}^1 &= C_{11}^{-1}Q_1^{-1}, \\ \mathcal{A}_{1\tau}^2 &= -C_{11}^{-1}C_{12}C_{22}^{-1}Q_2^{-1}, \\ \mathcal{A}_{2\tau}^1 &= -C_{22}^{-1}C_{21}C_{11}^{-1}Q_1^{-1}, \\ \mathcal{A}_{2\tau}^2 &= C_{22}^{-1}Q_2^{-1}, \\ \mathcal{A}_{\tau u} &= (C_{33} - C_{31}V_{13} - C_{32}V_{23}), \\ \mathcal{A}_{1\tau}^1 &= (C_{31} - C_{32}C_{22}^{-1}C_{21})C_{11}^{-1}Q_1^{-1}, \\ \mathcal{A}_{1\tau}^2 &= (C_{32} - C_{31}C_{11}^{-1}C_{12})C_{22}^{-1}Q_2^{-1}. \end{aligned} \quad (2.1.24)$$

The matrices Q_1 , Q_2 have been defined in (2.1.13), (2.1.14) and V_{13} , V_{23} in (2.1.18), (2.1.19). In this formulation

$$\tau_3 = -\mathcal{A}_{\tau u} \partial_3 \mathbf{u} - \mathcal{A}_{1\tau}^1 \tau_1 - \mathcal{A}_{1\tau}^2 \tau_2. \quad (2.1.25)$$

We can make a explicit allowance for the presence of material discontinuities by introducing an interfacial force term. Consider the case of an inclined interface specified by the equation $x_3 = h_\mu(\mathbf{x}_\perp)$, across the boundary the normal component of traction must be continuous and so

$$[\mathbf{t}_\mu]_{\mu^+}^{\mu^-} = [\tau_3 - \partial_\alpha h_\mu \tau_\alpha]_{\mu^+}^{\mu^-} / [1 + \partial_\alpha h_\mu \partial_\alpha h_\mu] = 0. \quad (2.1.26)$$

The continuity condition is therefore equivalent to a jump in the traction τ_3 ,

$$[\tau_3]_{\mu^+}^{\mu^-} = [\partial_\alpha h_\mu \tau_\alpha]_{\mu^+}^{\mu^-}. \quad (2.1.27)$$

This traction discontinuity can alternatively be viewed as a localised volume force \mathbf{f} situated at the material interface

$$\mathbf{f} = [\partial_\alpha h_\mu \tau_\alpha]_{\mu^+}^{\mu^-} \delta(x_3 - h_\mu(\mathbf{x}_\perp)). \quad (2.1.28)$$

We can represent the coupled equations (2.1.23), together with the continuity conditions in the compact form

$$\partial_\alpha \mathbf{u} = \mathcal{A}_{\alpha u}^\alpha \mathbf{u} + \mathcal{A}_{u\tau}^{\alpha\beta} \tau_\beta, \quad (2.1.29)$$

$$\begin{aligned} \partial_\alpha \tau_\alpha &= -\rho \omega^2 \mathbf{u} - \partial_3 [\mathcal{A}_{\tau u} \partial_3 \mathbf{u}] - \partial_3 [\mathcal{A}_{\tau\tau}^\alpha \tau_\alpha] \\ &\quad + \sum_\mu [\partial_\alpha h_\mu \tau_\alpha]_{\mu^+}^{\mu^-} \delta(x_3 - h_\mu(\mathbf{x}_\perp)), \end{aligned} \quad (2.1.30)$$

together with the continuity of displacement at any interface.

2.2 Modal expansions

In principle, we can reduce the dependence of the coupled equations for displacement and horizontal traction (2.1.29), (2.1.30) from three dimensions to two by projecting the vertical (x_3) dependence onto an orthogonal set of eigenfunctions. Thus we propose a representation of the displacement field as a sum of modal contributions with horizontally varying coefficients for each frequency ω e.g.

$$\mathbf{u} = \sum_J \sum_\theta c_{J\theta}(\mathbf{x}_\perp) \mathbf{u}_J^\theta(\mathbf{k}_{J\theta}, \mathbf{x}_3) e^{i\mathbf{k}_{J\theta} \cdot \mathbf{x}_\perp}, \quad (2.2.1)$$

where J is a mode-branch index and θ represents an angular spectrum of local plane waves for each mode index. $\mathbf{u}_J^\theta(\mathbf{k}_{J\theta}, \mathbf{x}_3)$ is the eigenfunction for the J th mode with horizontal wavenumber $\mathbf{k}_{J\theta}$. Associated with the displacement (2.2.1) there would be a corresponding traction field

$$\tau_\perp = \sum_J \sum_\theta c_{J\theta}(\mathbf{x}_\perp) \tau_{\perp J}^\theta(\mathbf{k}_{J\theta}, \mathbf{x}_3) e^{i\mathbf{k}_{J\theta} \cdot \mathbf{x}_\perp}, \quad (2.2.2)$$

The particular form of representation used in (2.2.1), (2.2.2) would be appropriate to a single set of reference modes for the entire region of interest and would be the three-dimensional analogue of the expansion used by Kennett (1984). Such a constant reference structure is likely to be helpful when the velocity model can be visualised as a set of perturbations (not necessarily small) from the reference structure. When the structural model includes systematic slow gradients in the seismic parameters, an

alternative choice for the modal representation would be to use local modes, as in the work of Maupin (1988) and Tromp (1994), where the eigenfunctions are constructed for the one-dimensional model in the vertical column below each point. In such a coupled local-mode expansion the eigenfunctions are position dependent and the phase terms include the cumulative phase history for each modal and angular component. A further possibility is to follow the procedure sketched in the Appendix to Kennett (1984) and work with the local modes of a reference medium which is a smoothed version of the actual structure. Such an approach combines some of the merits of the local mode and reference structure approaches and can be applied to models with velocity gradients and significant local variations.

In order to include all these three types of modal representation in the subsequent analysis we will adopt a generic form for the modal representation of the displacement as

$$\mathbf{u} = \sum_q c_q(\mathbf{x}_\perp) \mathbf{u}_q^\epsilon(\mathbf{k}_q, \mathbf{x}_3) e_q(\mathbf{k}_q, \mathbf{x}_\perp), \quad (2.2.3)$$

where we have used a single index q covering both the mode order and the angular spectrum, and e_q represents the phase contribution. We will also use the index r in a similar way. The tractions corresponding to (2.2.3) will be written as

$$\tau = \sum_q c_q(\mathbf{x}_\perp) \tau_q^\epsilon(\mathbf{k}_q, \mathbf{x}_3) e_q(\mathbf{k}_q, \mathbf{x}_\perp), \quad (2.2.4)$$

We will always represent summation over the mode index q , r explicitly but will continue to use the convention of implicit summation over repeated suffices α, β for coordinates.

On substituting the modal representations (2.2.2), (2.2.3) into the horizontal evolution equations (2.1.29), (2.1.30) we find

$$\partial_\alpha \left(\sum_q c_q \mathbf{u}_q^\epsilon e_q \right) = \sum_q \left(\mathcal{A}_{uu}^\alpha \partial_3 \mathbf{u}_q^\epsilon + \mathcal{A}_{u\tau}^{\alpha\beta} \tau_{q\beta}^\epsilon \right) c_q e_q, \quad (2.2.5)$$

$$\begin{aligned} \partial_\alpha \left(\sum_q c_q \tau_q^\epsilon e_q \right) &= \sum_q \left(-\rho \omega^2 \mathbf{u}_q^\epsilon - \partial_3 [\mathcal{A}_{\tau u} \partial_3 \mathbf{u}_q^\epsilon] - \partial_3 [\mathcal{A}_{\tau\tau}^\alpha \tau_{q\alpha}^\epsilon] \right) c_q e_q \\ &\quad + \sum_{q, \mu} [\partial_\alpha h_\mu \tau_{q\alpha}^\epsilon]_{\mu^+}^{\mu^-} \delta(x_3 - h_\mu(\mathbf{x}_\perp)) c_q e_q, \end{aligned} \quad (2.2.6)$$

where we have allowed for the possible presence of sloping interfaces. Consider the terms on the left hand side of (2.2.5), (2.2.6) e.g.

$$\partial_\alpha \left(\sum_q c_q \mathbf{u}_q^\epsilon e_q \right) = \sum_q \partial_\alpha (\mathbf{u}_q^\epsilon) c_q e_q + \sum_q \mathbf{u}_q^\epsilon \partial_\alpha (c_q e_q). \quad (2.2.7)$$

The horizontal derivatives of the eigenfunctions \mathbf{u}_q^ϵ will appear for a local mode treatment or where a smoothly varying reference medium is being employed, but will not be present in the case of a constant reference medium.

We now introduce the dual modes $\mathbf{u}_q^{\epsilon*}$, $\tau_q^{\epsilon*}$ associated with the wavenumber $-\mathbf{k}_q$ which appear in the orthogonality condition between different modes derived in Appendix B. We define

$$\mathbf{u}_r^{\#} = \mathbf{u}_r^e(-\mathbf{k}_r, \mathbf{x}_\perp, x_3, \omega). \quad (2.2.8)$$

These dual modes were used implicitly by Kennett (1984) and explicitly by Maupin (1992) in a study of surface wave guiding in a two-dimensional structure.

We operate on the displacement equation (2.2.5) with the horizontal traction for the dual mode

$$\begin{aligned} & \sum_q \partial_\alpha \mathbf{u}_q^e \cdot \tau_{r\alpha}^{\#} c_q e_q + \sum_q \mathbf{u}_q^e \cdot \tau_{r\alpha}^{\#} \partial_\alpha (c_q e_q) \\ &= \sum_q \left(\tau_{r\alpha}^{\#} \cdot \mathcal{A}_{uu}^{\alpha\beta} \partial_\beta \mathbf{u}_q^e + \tau_{r\alpha}^{\#} \cdot \mathcal{A}_{ut}^{\alpha\beta} \tau_{q\alpha}^e \right) c_q e_q, \end{aligned} \quad (2.2.9)$$

and on the traction equation (2.2.6) with the displacement in the dual mode

$$\begin{aligned} & \sum_q \partial_\alpha \tau_{q\alpha}^e \cdot \mathbf{u}_r^{\#} c_q e_q + \sum_q \tau_{q\alpha}^e \cdot \mathbf{u}_r^{\#} \partial_\alpha (c_q e_q) \\ &= \sum_q \left(-\rho \omega^2 \mathbf{u}_r^{\#} \cdot \mathbf{u}_q^e - \mathbf{u}_r^{\#} \cdot \partial_3 \left[\mathcal{A}_{\tau u} \partial_3 \mathbf{u}_q^e \right] - \mathbf{u}_r^{\#} \cdot \partial_3 \left[\mathcal{A}_{\tau\tau}^{\alpha} \tau_{q\alpha}^e \right] \right) c_q e_q \\ & \quad + \sum_q \partial_\alpha h_{\mu\alpha} \mathbf{u}_r^{\#} \cdot [\tau_{q\alpha}^e]_{\mu-}^{\mu+} \delta(x_3 - h_\mu(\mathbf{x}_\perp)) c_q e_q, \end{aligned} \quad (2.2.10)$$

then subtract (2.2.10) from (2.2.9) and integrate over the full depth of the half-space. The resulting equations for the horizontal evolution of the modal contribution terms c_q take the form

$$\begin{aligned} & \sum_q \int_0^\infty dx_3 \left(\mathbf{u}_q^e \cdot \tau_{r\alpha}^{\#} - \mathbf{u}_r^{\#} \cdot \tau_{q\alpha}^e \right) \partial_\alpha (c_q e_q) \\ & + \sum_q \int_0^\infty dx_3 \left(\partial_\alpha \mathbf{u}_q^e \cdot \tau_{r\alpha}^{\#} - \mathbf{u}_r^{\#} \cdot \partial_\alpha \tau_{q\alpha}^e \right) c_q e_q \\ & - \sum_q \int_0^\infty dx_3 \left(\partial_\alpha h_{\mu\alpha} \mathbf{u}_r^{\#} \cdot [\tau_{q\alpha}^e]_{\mu-}^{\mu+} \right) c_q e_q \\ & = \sum_q \int_0^\infty dx_3 \left(\tau_{r\alpha}^{\#} \cdot \mathcal{A}_{uu}^{\alpha\beta} \partial_\beta \mathbf{u}_q^e + \tau_{r\alpha}^{\#} \cdot \mathcal{A}_{ut}^{\alpha\beta} \tau_{q\alpha}^e \right. \\ & \quad \left. + \rho \omega^2 \mathbf{u}_r^{\#} \cdot \mathbf{u}_q^e + \mathbf{u}_r^{\#} \cdot \partial_3 \left[\mathcal{A}_{\tau u} \partial_3 \mathbf{u}_q^e \right] + \mathbf{u}_r^{\#} \cdot \partial_3 \left[\mathcal{A}_{\tau\tau}^{\alpha} \tau_{q\alpha}^e \right] \right) c_q e_q. \end{aligned} \quad (2.2.11)$$

The orthogonality property between different modes derived in Appendix B can be written in a comparable notation as

$$i(k_{q\alpha} - k_{r\alpha}) \cdot \int_0^\infty dx_3 \left(\mathbf{u}_q^e \cdot \tau_{r\alpha}^{\#} - \mathbf{u}_r^{\#} \cdot \tau_{q\alpha}^e \right) = 0, \quad (2.2.12)$$

and the normalisation when \mathbf{k}_q is equal to \mathbf{k}_r as

$$i \int_0^\infty dx_3 \left(\mathbf{u}_q^e \cdot \tau_{q\alpha}^{\#} - \mathbf{u}_q^{\#} \cdot \tau_{q\alpha}^e \right) = k_{q\alpha} / |\mathbf{k}_q|. \quad (2.2.13)$$

The equations (2.2.11) represent the most general set of coupled equations for the modal coefficients and can be simplified somewhat by making specific assumptions about the form of the modal representation.

3 EVOLUTION EQUATIONS FOR MODAL COEFFICIENTS

3.1 Matrix equations

We can express the coupled equations (2.2.11) for the modal coefficients c_q in the form of a set of N equations for N expansion coefficients $\{c_q\}$

$$\sum_q \left[L_{rq}^{\alpha} \partial_\alpha (c_q e_q) - J_{rq} c_q e_q - H_{rq} c_q e_q \right] = \sum_q M_{rq} c_q e_q. \quad (3.1.1)$$

The matrix elements on the left hand side of (3.1.1) depend on the structural parameters for the medium purely through the functional form of the modal eigenfunctions.

$$L_{rq}^{\alpha} = \int_0^\infty dx_3 \left(\mathbf{u}_q^e \cdot \tau_{r\alpha}^{\#} - \mathbf{u}_r^{\#} \cdot \tau_{q\alpha}^e \right) \quad (3.1.2)$$

$$J_{rq} = - \int_0^\infty dx_3 \left(\mathbf{u}_q^e \cdot \partial_\alpha \tau_{r\alpha}^{\#} - \partial_\alpha \mathbf{u}_q^e \cdot \tau_{r\alpha}^{\#} \right)$$

$$H_{rq} = - \sum_\mu \left(\partial_\alpha h_{\mu\alpha} \mathbf{u}_r^{\#} \cdot [\tau_{q\alpha}^e]_{\mu-}^{\mu+} \right)$$

Whereas,

$$M_{rq} = \int_0^\infty dx_3 \left(\tau_{r\alpha}^{\#} \cdot \mathcal{A}_{uu}^{\alpha\beta} \partial_\beta \mathbf{u}_q^e + \tau_{r\alpha}^{\#} \cdot \mathcal{A}_{ut}^{\alpha\beta} \tau_{q\alpha}^e \right. \\ \left. + \rho \omega^2 \mathbf{u}_r^{\#} \cdot \mathbf{u}_q^e + \mathbf{u}_r^{\#} \cdot \partial_3 \left[\mathcal{A}_{\tau u} \partial_3 \mathbf{u}_q^e \right] + \mathbf{u}_r^{\#} \cdot \partial_3 \left[\mathcal{A}_{\tau\tau}^{\alpha} \tau_{q\alpha}^e \right] \right) \quad (3.1.3)$$

depends on the eigenfunctions, the operators \mathcal{A} , which depend explicitly on the seismic parameters (2.1.24), and their vertical derivatives.

The orthogonality relation between different modes derived in Appendix B can be expressed in terms of the matrix L_{rq} as

$$i(k_{q\alpha} - k_{r\alpha}) L_{rq}^{\alpha} = 0 \quad \text{for } r \neq q, \quad (3.1.4)$$

with the normalisation

$$i L_{qq}^{\alpha} = k_{q\alpha} / |\mathbf{k}_q|, \quad \text{no summation on } q, \quad (3.1.5)$$

for the diagonal elements.

The full set of coupled equations can then be expressed in matrix form in terms of a vector \hat{c} whose entries are composed of modal coefficients and phase terms,

$$\hat{c}_q = c_q e_q. \quad (3.1.6)$$

The phase term e_q may be alternatively written as the action of a phase matrix \mathbf{E} on a vector of modal coefficients so that

$$(\hat{c})_q = \mathbf{E} c, \quad (3.1.7)$$

where

$$\mathbf{E} = \text{diag} \{ e^{i\mathbf{k}_q \cdot \mathbf{x}_\perp} \}. \quad (3.1.8)$$

In terms of the vector \hat{c} the coupled equations for the evolution of the modal coefficients can be written in the compact form

$$\mathbf{L}^{\alpha} \partial_\alpha \hat{c} = \mathbf{J} \hat{c} + \mathbf{H} \hat{c} + \mathbf{M} [\mathcal{A}] \hat{c}, \quad (3.1.9)$$

where we have indicated the explicit dependence of the matrix \mathbf{M} on the structural operators \mathcal{A} . We will first establish the equations appropriate to a stratified medium and then use these to simplify the coupled equations in the case of three-dimensional heterogeneity.

3.2 A stratified medium

Consider now a laterally homogeneous medium for which we will denote the differential operators \mathcal{A}^0 . For such a stratified medium, the modes must propagate independently. The eigenfunctions do not depend on horizontal position so $J_{\tau q} = 0$, and the interfaces are flat so that the interface term $H_{\tau q} = 0$. The result is significant simplification of the equations (3.1.9) for this stratified case so that

$$\mathbf{L}^\alpha \partial_\alpha \hat{\mathbf{c}} = \mathbf{M}[\mathcal{A}^0] \hat{\mathbf{c}}, \quad (3.2.1)$$

A single mode

$$\mathbf{u} = \mathbf{u}_q^e(x_3) e^{ik_{q\alpha}^0 x_\perp} = \mathbf{u}_q^e e_q, \quad (3.2.2)$$

will satisfy the basic equations (3.2.1) without any need for coupling,

$$\partial_\alpha c_q = 0, \quad \partial_\alpha e_q = ik_{q\alpha}^0 e_q, \quad (3.2.3)$$

and so

$$\partial_\alpha (c_q e_q) = ik_{q\alpha}^0 (c_q e_q). \quad (3.2.4)$$

The entire contribution to $\partial_\alpha \hat{\mathbf{c}}$ will come from the phase elements e_q . Thus

$$\partial_\alpha \hat{\mathbf{c}} = ik_\alpha^0 \hat{\mathbf{c}} \quad (3.2.5)$$

where \mathbf{k}_α^0 is a diagonal matrix whose entries are the α component of the horizontal wavevectors \mathbf{k}_q^0 for the stratified medium

$$ik_\alpha^0 = \text{diag} \{ik_{q\alpha}^0\}. \quad (3.2.6)$$

For this horizontally invariant case

$$\mathbf{L}^\alpha ik_\alpha^0 \hat{\mathbf{c}} = \mathbf{M}[\mathcal{A}^0] \hat{\mathbf{c}}. \quad (3.2.7)$$

Since the modal weights are arbitrary, we can identify the contribution from the structural terms $\mathbf{M}[\mathcal{A}^0]$ with a weighted composition of the horizontal wavevectors

$$\mathbf{M}[\mathcal{A}^0] = \mathbf{L}^\alpha ik_\alpha^0. \quad (3.2.8)$$

3.3 A fixed reference structure

We consider an expansion (2.2.1) in terms of the modes of a fixed reference structure with propagation properties described by the differential operators \mathcal{A}^0 . The same set of eigenmodes \mathbf{u}^e is used throughout and so there will be no contributions from the horizontal derivatives of the modal eigenfunctions (i.e. $J = 0$).

The horizontal evolution equations for the modal coefficients are then

$$\mathbf{L}^\alpha \partial_\alpha \hat{\mathbf{c}} = [\mathbf{M}[\mathcal{A}(\mathbf{x}_\perp)] + \mathbf{H}(\mathbf{x}_\perp)] \hat{\mathbf{c}}, \quad (3.3.1)$$

since we have to allow for the presence of sloping boundaries through the interface term \mathbf{H} . The structural component $\mathbf{M}[\mathcal{A}]$ is linear in the differential operators \mathcal{A} and so we can recast the equation (3.3.1) in terms of perturbations from the reference structure, through differential operators of the form

$$\Delta \mathcal{A}_{\alpha\tau} = \mathcal{A}_{\alpha\tau} - \mathcal{A}_{\alpha\tau}^0, \quad (3.3.2)$$

by using the representation (3.2.8) for $\mathbf{M}[\mathcal{A}^0]$. We obtain

$$\begin{aligned} \mathbf{L}^\alpha \partial_\alpha \hat{\mathbf{c}} &= [\mathbf{L}^\alpha ik_\alpha^0 - \mathbf{M}[\mathcal{A}^0] + \mathbf{M}[\mathcal{A}(\mathbf{x}_\perp)] + \mathbf{H}(\mathbf{x}_\perp)] \hat{\mathbf{c}}, \\ &= [\mathbf{L}^\alpha ik_\alpha^0 + \mathbf{M}[\Delta \mathcal{A}(\mathbf{x}_\perp)] + \mathbf{H}(\mathbf{x}_\perp)] \hat{\mathbf{c}} \end{aligned} \quad (3.3.3)$$

where we have exploited the linearity of \mathbf{M} with respect to \mathcal{A} . The elements of the structural term have the explicit form

$$\begin{aligned} M_{\tau q}[\Delta \mathcal{A}(\mathbf{x}_\perp)] \\ = \int_0^\infty dx_3 \left(\tau_{\tau\alpha}^\# \Delta \mathcal{A}_{\alpha u}^\alpha(\mathbf{x}_\perp) \partial_3 \mathbf{u}_q^\tau + \tau_{\tau\alpha}^\# \Delta \mathcal{A}_{\alpha\tau}^{\alpha\beta}(\mathbf{x}_\perp) \tau_{q\beta}^\tau \right. \\ \left. + \rho \omega^2 \mathbf{u}_\tau^\# \mathbf{u}_q^\tau + \mathbf{u}_\tau^\# \partial_3 \left[\Delta \mathcal{A}_{\tau u}(\mathbf{x}_\perp) \partial_3 \mathbf{u}_q^\tau \right] + \mathbf{u}_\tau^\# \partial_3 \left[\Delta \mathcal{A}_{\tau\tau}^\alpha(\mathbf{x}_\perp) \tau_{q\alpha}^\tau \right] \right). \end{aligned} \quad (3.3.4)$$

The derivation above parallels the approach used by Kennett (1984) for two-dimensional structures but is rendered more complex by the restricted orthogonality properties in the three-dimensional case.

We can simplify the equation (3.3.3) for the evolution of the modal coefficients in this case of a fixed reference structure by demodulating the phase component. Following (3.1.7) we write

$$\hat{\mathbf{c}} = \mathbf{E}^0 \mathbf{c}, \quad \text{where} \quad \partial_\alpha \mathbf{E}^0 = ik_\alpha^0 \mathbf{E}^0. \quad (3.3.5)$$

Then

$$\partial_\alpha \hat{\mathbf{c}} = \partial_\alpha \mathbf{E}^0 \mathbf{c} + \mathbf{E}^0 \partial_\alpha \mathbf{c} = ik_\alpha^0 \mathbf{E}^0 \mathbf{c} + \mathbf{E}^0 \partial_\alpha \mathbf{c}, \quad (3.3.6)$$

and so

$$\begin{aligned} \mathbf{L}^\alpha \partial_\alpha \hat{\mathbf{c}} &= \mathbf{L}^\alpha ik_\alpha^0 \mathbf{E}^0 \mathbf{c} + \mathbf{L}^\alpha \mathbf{E}^0 \partial_\alpha \mathbf{c} \\ &= [\mathbf{L}^\alpha ik_\alpha^0 \mathbf{E}^0 + \mathbf{M}[\Delta \mathcal{A}(\mathbf{x}_\perp)] + \mathbf{H}(\mathbf{x}_\perp)] \mathbf{E}^0 \mathbf{c}, \end{aligned} \quad (3.3.7)$$

The modal weighting factors \mathbf{c} themselves therefore satisfy the coupled set of equations

$$\mathbf{L}^\alpha \mathbf{E}^0 \partial_\alpha \mathbf{c} = [\mathbf{M}[\Delta \mathcal{A}(\mathbf{x}_\perp)] + \mathbf{H}(\mathbf{x}_\perp)] \mathbf{E}^0 \mathbf{c}. \quad (3.3.8)$$

3.4 Local Modes

In this case, the modal field used in the representation (2.2.1) is chosen to match the properties of the structure along a vertical profile beneath each surface point. The eigenfunctions $\mathbf{u}_q^e(\mathbf{x}_\perp, x_3)$ will therefore vary with horizontal position, but their properties will be such as to annihilate any contribution from the integrals over the terms involving the differential operators.

From (3.1.9), using the local mode eigenfunctions,

$$\mathbf{L}^\alpha(\mathbf{x}_\perp)\partial_\alpha\hat{\mathbf{c}} = [\mathbf{M}[\mathcal{A}(\mathbf{x}_\perp)] + \mathbf{J}(\mathbf{x}_\perp) + \mathbf{H}(\mathbf{x}_\perp)]\hat{\mathbf{c}}. \quad (3.4.1)$$

But, since the modes employed match the vertical structure at each point we have from (3.2.8)

$$\mathbf{L}^\alpha(\mathbf{x}_\perp)\mathbf{i}\mathbf{k}_\alpha = \mathbf{M}[\mathcal{A}(\mathbf{x}_\perp)]. \quad (3.4.2)$$

This result enables us to simplify (3.4.1) to the form

$$\mathbf{L}^\alpha(\mathbf{x}_\perp)\partial_\alpha\hat{\mathbf{c}} = [\mathbf{L}^\alpha(\mathbf{x}_\perp)\mathbf{i}\mathbf{k}_\alpha + \mathbf{J}(\mathbf{x}_\perp) + \mathbf{H}(\mathbf{x}_\perp)]\hat{\mathbf{c}}, \quad (3.4.3)$$

where the term $\mathbf{J}(\mathbf{x}_\perp)$ depends on the horizontal gradients of the modal eigenfunctions, which in turn will depend on the horizontal gradients of the material properties.

3.5 Local modes for a smoothed reference structure

The direct use of the local modes approach is most effective when the heterogeneity in the medium is smooth and slowly varying so that the horizontal derivatives of the modal eigenfunctions remain small.

However, when short-scale structure is present, it is preferable to adopt a representation of the wavefield in terms of the local modes of a smoothly varying reference medium which represents the long spatial wavelengths of the heterogeneity. The smaller scale spatial variations of the seismic parameters can be included by an allowance for the departure from the reference model. This hybrid approach allows the representation of a wide range of structures.

We start from the general equations (3.1.9) for the evolution of the modal coefficients which we will write as

$$\tilde{\mathbf{L}}^\alpha(\mathbf{x}_\perp)\partial_\alpha\hat{\mathbf{c}} = [\tilde{\mathbf{M}}[\mathcal{A}(\mathbf{x}_\perp)] + \tilde{\mathbf{J}}(\mathbf{x}_\perp) + \tilde{\mathbf{H}}(\mathbf{x}_\perp)]\hat{\mathbf{c}}, \quad (3.5.1)$$

where the overbar is to indicate the use of local modes for the reference structure. These modes will satisfy an analogue of (3.2.8),

$$\tilde{\mathbf{L}}^\alpha(\mathbf{x}_\perp)\mathbf{i}\mathbf{k}_\alpha^\tau(\mathbf{x}_\perp) = \tilde{\mathbf{M}}[\mathcal{A}^\tau(\mathbf{x}_\perp)], \quad (3.5.2)$$

where \mathbf{k}_α^τ is the diagonal matrix whose entries are the local horizontal wavenumbers for the reference medium, and \mathcal{A}^τ are the differential operators corresponding to the properties of the reference structure. Thus we have

$$\begin{aligned} \tilde{\mathbf{L}}^\alpha(\mathbf{x}_\perp)\partial_\alpha\hat{\mathbf{c}} &= [\tilde{\mathbf{L}}^\alpha(\mathbf{x}_\perp)\mathbf{i}\mathbf{k}_\alpha^\tau(\mathbf{x}_\perp) + \tilde{\mathbf{J}}(\mathbf{x}_\perp) + \tilde{\mathbf{H}}(\mathbf{x}_\perp)]\hat{\mathbf{c}} \\ &= [\tilde{\mathbf{L}}^\alpha(\mathbf{x}_\perp)\mathbf{i}\mathbf{k}_\alpha^\tau(\mathbf{x}_\perp) + \tilde{\mathbf{J}}(\mathbf{x}_\perp) + \tilde{\mathbf{H}}(\mathbf{x}_\perp) + \tilde{\mathbf{M}}[\Delta\mathcal{A}^\tau(\mathbf{x}_\perp)]]\hat{\mathbf{c}} \end{aligned} \quad (3.5.3)$$

Here, once again, we have exploited the linearity of the operator $\tilde{\mathbf{M}}$ and have set

$$\Delta\mathcal{A}^\tau(\mathbf{x}_\perp) = \mathcal{A}(\mathbf{x}_\perp) - \mathcal{A}^\tau(\mathbf{x}_\perp), \quad (3.5.4)$$

which is the differential operator for the differences in structure between the actual medium and the smoothed reference structure. Equation (3.5.1) represents the

three-dimensional generalisation of the technique sketched for the two-dimensional case in the Appendix to Kennett (1984).

ACKNOWLEDGMENTS

I would like to acknowledge very useful discussions with Professor C. Thomson on the properties of surface waves in anisotropic media.

References

- Bostock, M.G., 1992. Reflection and transmission of surface waves in laterally varying media, *Geophys. J. Int.*, **109**, 411-436.
- Kennett, B.L.N., 1983. *Seismic Wave Propagation in Stratified Media*, Cambridge University Press, Cambridge.
- Kennett, B.L.N., 1984. Guided wave propagation in varying media — I. Theoretical development, *Geophys. J. R. astr. Soc.*, **79**, 235-255.
- Maupin, V., 1988. Surface waves across 2-D structures: a method based on coupled local modes, *Geophys. J. Int.*, **93**, 173-185.
- Maupin, V., 1992. Modelling of laterally trapped surface waves with application to Rayleigh waves in the Hawaiian swell, *Geophys. J. Int.*, **110**, 553-570.
- Maupin, V. & Kennett, B.L.N., 1987. On the use of truncated modal expansions in laterally varying media, *Geophys. J. R. astr. Soc.*, **91**, 837-851.
- Park, J., 1987. Asymptotic coupled-mode expressions for multiplet amplitude anomalies and frequency shifts on an aspherical earth, *Geophys. J. R. astr. Soc.*, **90**, 129-169.
- Romanowicz, R., 1987. Multiplet-multiplet coupling due to lateral heterogeneity: asymptotic effects on the amplitude and frequency of the Earth's normal modes, *Geophys. J. R. astr. Soc.*, **90**, 75-100.
- Snieder, R., 1986a. 3D scattering of surface waves and a formalism for surface wave holography, *Geophys. J. R. astr. Soc.*, **84**, 581-605.
- Snieder, R., 1986b. The influence of topography on the propagation and scattering of surface waves, *Phys. Earth Planet. Inter.*, **44**, 226-241.
- Snieder, R. & Nolet, G., 1987. Linearised scattering of surface waves on a spherical earth, *J. Geophys.*, **61**, 55-63.
- Tanimoto, T., 1990. Modelling curved surface wave paths: membrane surface wave synthetics, *Geophys. J. Int.*, **102**, 89-100.
- Tromp, J., 1994. A coupled local-mode analysis of surface-wave propagation in a laterally heterogeneous waveguide, *Geophys. J. Int.*, **117**, 153-161.
- Tsuboi, S. & Geller, R.J., 1989. Coupling between the multiplets of laterally heterogeneous Earth models, *Geophys. J. Int.*, **96**, 371-380.
- Woodhouse, J.H., 1974. Surface waves in a laterally varying layered structure, *Geophys. J. R. astr. Soc.*, **37**, 461-490.
- Woodhouse, J.H. & Wong, Y.K., 1986. Amplitude, phase and path anomalies of mantle waves, *Geophys. J. R. astr. Soc.*, **87**, 753-774.
- Yu, Y. & Park, J., 1993. Upper mantle anisotropy and coupled-mode long-period surface waves, *Geophys. J. Int.*, **114**, 473-489.

APPENDIX A: A PROPAGATION INVARIANT FOR SURFACE WAVES

Tromp (1994, Appendix B) has demonstrated in an important property of trapped wavefields in a three-dimensional model using a dyadic notation. Tromp's analysis was restricted to perfectly elastic models and was interpreted as a consequence of conservation of energy. We will show that this result can be extended to attenuative anisotropic structures.

Consider a half space $x_3 \geq 0$ with two displacement fields \mathbf{u}, \mathbf{v} with associated stress tensors τ_{ij} , σ_{ij} in a source free zone. For the first field we express the equation of motion in a form which isolates the dependence on horizontal coordinates

$$\partial_\alpha \tau_{\alpha j} + \partial_3 \tau_{3j} = -\rho \omega^2 u_j, \quad (\text{A.1})$$

where, as in the body of the text, we have used the summation convention with greek subscripts confined to the values 1,2. We have an equivalent equation for the second field

$$\partial_\alpha \sigma_{\alpha j} + \partial_3 \sigma_{3j} = -\rho \omega^2 v_j. \quad (\text{A.2})$$

We now contract (A.1) with \mathbf{v} and (A.2) with \mathbf{u} and subtract to obtain

$$\nu_j \partial_\alpha \tau_{\alpha j} - u_j \partial_\alpha \sigma_{\alpha j} + \nu_j \partial_3 \tau_{3j} - u_j \partial_3 \sigma_{3j} = 0. \quad (\text{A.3})$$

A consequence of the $i, j \rightarrow kl$ symmetry of the full anisotropic elastic moduli is that

$$\partial_l \nu_j \tau_{ij} - \partial_l u_j \sigma_{ij} = c_{ijkl} \partial_j \nu_k u_l - c_{ijkl} \partial_l u_j \partial_k \nu_l = 0. \quad (\text{A.4})$$

This property is sustained for the complex moduli in the presence of attenuation. We may use (A.4) to recast (A.3) in the form of horizontal and vertical derivatives of products of displacement and traction, and then when we integrate over a vertical profile in the halfspace we find

$$\int_0^\infty dx_3 \left\{ \partial_\alpha [\nu_j \tau_{\alpha j} - u_j \sigma_{\alpha j}] + \partial_3 [\nu_j \tau_{3j} - u_j \sigma_{3j}] \right\} = 0. \quad (\text{A.5})$$

We now assume that both \mathbf{u}, \mathbf{v} are surface wave fields such that

$$\mathbf{u}, \mathbf{v}, \tau_{ij}, \sigma_{ij} \rightarrow 0 \quad \text{as} \quad x_3 \rightarrow \infty, \quad \tau_{ij} n_j = \sigma_{ij} n_j = 0 \quad \text{at the free surface}, \quad (\text{A.6})$$

where \mathbf{n} is the normal to the free surface. We integrate (A.5) by parts with respect to x_3 to produce

$$\int_0^\infty dx_3 \left\{ \partial_\alpha [\nu_j \tau_{\alpha j} - u_j \sigma_{\alpha j}] \right\} + \sum_j [\nu_j \tau_{3j} - u_j \sigma_{3j}]_{\mu=0}^{\mu+} = 0. \quad (\text{A.7})$$

where the summation arises from any inclined boundaries, at which the displacement and the normal traction must be continuous. If the equation of an inclined boundary is $x_3 = h_\mu(\mathbf{x}_\perp)$, the normal vector

$$\mathbf{n} = (\partial_\alpha h_\mu, -1) [1 + \partial_\alpha h_\mu \partial_\alpha h_\mu]^{-1/2}; \quad (\text{A.8})$$

so that the interface condition can be written as

$$[\partial_\alpha h_\mu [\nu_j \tau_{\alpha j} - u_j \sigma_{\alpha j}] - [\nu_j \tau_{3j} - u_j \sigma_{3j}]]_{\mu=0}^{\mu+} = 0. \quad (\text{A.9})$$

We can therefore replace the summation over interfaces in (A.7) by an equivalent set of terms which depend on the gradients of the interfaces

$$\int_0^\infty dx_3 \left\{ \partial_\alpha [\nu_j \tau_{\alpha j} - u_j \sigma_{\alpha j}] \right\} + \sum_\mu \partial_\alpha h_\mu [\nu_j \tau_{\alpha j} - u_j \sigma_{\alpha j}]_{\mu=0}^{\mu+} = 0. \quad (\text{A.10})$$

We can now recognise the left hand side of (A.10) as the horizontal gradient of the vertical integral of a composition of displacement and horizontal traction terms

$$\partial_\alpha \left\{ \int_0^\infty dx_3 [\nu_j \tau_{\alpha j} - u_j \sigma_{\alpha j}] \right\} = 0. \quad (\text{A.11})$$

In terms of the horizontal tractions τ_α we can recast (A.11) in the form

$$\partial_\alpha \left\{ \int_0^\infty dx_3 [\mathbf{v} \cdot \boldsymbol{\tau}_\alpha(\mathbf{u}) - \mathbf{u} \cdot \boldsymbol{\tau}_\alpha(\mathbf{v})] \right\} = 0. \quad (\text{A.12})$$

The equivalent forms (A.11), (A.12) represent a constraint on the horizontal variation of the composition of displacement and horizontal traction terms, which in some circumstances can be interpreted as having a relation to energy transport (cf. Tromp 1994). The result is valid for surface wave fields in an arbitrary anisotropic and anelastic halfspace subject to the boundary conditions (A.6).

The final result is very similar to propagation invariants in the form of surface integrals established by Kennett (1984b) for a quasi-stratified medium with horizontal variations superimposed on a dominant x_3 dependence. For these propagation invariants we have a two-dimensional integral with a one-dimensional invariance property. The invariants have proved to be very useful for establishing calculation schemes for laterally varying media (see e.g. Koketsu et al 1990). In contrast, for the surface wave case we have a one-dimensional constraint on the wavefield with a two-dimensional invariance property for fields of surface waves.

APPENDIX B: ORTHOGONALITY BETWEEN SURFACE WAVE MODES IN ATTENUATIVE ANISOTROPIC STRUCTURES

We can use the results of Appendix A to derive an orthogonality condition between eigenmodes for a horizontally stratified model. We will denote the eigenstates by using upper case subscripts, and choose the first surface-wave displacement field as

$$\mathbf{u} = \mathbf{u}_p^s(\mathbf{k}_p, x_3) e^{ik_p x_\perp}, \quad (\text{B.1})$$

where \mathbf{u}_p^s represents the displacement eigenfunction and \mathbf{k}_p is the horizontal wavevector. We take the second displacement field to be the dual field with a reversed wavevector

$$\mathbf{v} = \mathbf{u}_q^s(-\mathbf{k}_q, x_3) e^{-ik_q x_\perp}, \quad (\text{B.2})$$

exploiting the point symmetry in the horizontal wavevector for an arbitrary anisotropic medium.

Now, using the conservation property (A.12) with these definitions of \mathbf{u}, \mathbf{v} we obtain

$$\partial_\alpha \left\{ \int_0^\infty dx_3 [\mathbf{u}_p^s(\mathbf{k}_p, x_3) \cdot \boldsymbol{\tau}_\alpha^s(-\mathbf{k}_q, x_3) - \mathbf{u}_q^s(-\mathbf{k}_q, x_3) \cdot \boldsymbol{\tau}_\alpha^s(\mathbf{k}_p, x_3)] e^{i(k_{pq} - k_{qp})x_\perp} \right\} = 0.$$

(B.3)

The only part of the integral in (B.3) that depends on the horizontal coordinates is the exponential and so (B.3) can be written as

$$i(\mathbf{k}_P - \mathbf{k}_Q) \cdot \left\{ \int_0^\infty dx_3 [\mathbf{u}_P^e(\mathbf{k}_P, x_3) \cdot \boldsymbol{\tau}_{\alpha Q}^e(-\mathbf{k}_Q, x_3) - \mathbf{u}_Q^e(-\mathbf{k}_Q, x_3) \cdot \boldsymbol{\tau}_{\alpha P}^e(\mathbf{k}_P, x_3)] \right\} = 0. \quad (\text{B.4})$$

representing an orthogonality relation between different modes for an anisotropic and attenuative halfspace. For a perfectly elastic medium we can recover the form used by Tromp (1994) in which the complex conjugate of the eigenstate replaces the dual eigenstate.

The three-dimensional orthogonality relation (B.4) includes the form derived by Maupin (1988) for oblique propagation in a two-dimensional medium for which the 2-component of the wavenumber is common to both modal fields, when the vectorial relation reduces to just an orthogonality relation for the 1-components.

For a single mode i.e. $\mathbf{k}_P = \mathbf{k}_Q$ we can adopt a normalisation

$$i \int_0^\infty dx_3 [\mathbf{u}_P^e(\mathbf{k}_P, x_3) \cdot \boldsymbol{\tau}_{\alpha P}^e(-\mathbf{k}_P, x_3) - \mathbf{u}_P^e(-\mathbf{k}_P, x_3) \cdot \boldsymbol{\tau}_{\alpha P}^e(\mathbf{k}_P, x_3)] = k_{PA}/|\mathbf{k}_P|. \quad (\text{B.5})$$

which is equivalent to that employed by Kennett (1984) for two-dimensional problems including attenuation.

Part IV: A regionalized upper-mantle (RUM) model.

Submitted to *Journal of Geophysical Research*, 1997.

A Regionalized Upper-Mantle (RUM) Model

Ólafur Gudmundsson and Malcolm Sambridge

Research School of Earth Sciences, Australian National University, Canberra

Abstract

Seismic velocity heterogeneity in the Earth's mantle is strongly concentrated near its top. The shallow heterogeneity of the mantle correlates strongly with surface tectonics. We use these observations as constraints of a tomographic experiment aimed at building a regionalized upper-mantle (RUM) reference model. We use a select set of teleseismic travel times to minimize the mapping of mislocation into structure. The data selection emphasizes the robustness of individual picks. The form of the RUM model is a set of velocity profiles as functions of depth through the upper mantle for each of the different tectonic provinces of Earth. Together the profiles constitute a three-dimensional model which incorporates considerable structural detail, but is described by only 90 parameters and has only about 22 degrees of freedom. This is achieved by irregularly sampling a detailed regionalization of the globe, by detailed mapping of subducted lithosphere in the mantle as defined by seismicity, and by combining these structures in an irregular grid in which book keeping is efficiently handled. The resulting RUM model includes subducting slabs as sharp fast features in the upper mantle. Old continents are fast, young oceans are slow. Models have been derived for both compressional and shear velocity. The RUM model is designed to represent as much of upper-mantle heterogeneity as seen by body wave travel times as possible with a simple model. It can be useful as a reference model for individual tectonic regions. Travel times are efficiently generated for the RUM model. Mislocations of explosions of known location are significantly reduced when corrections for the RUM model are applied to travel-time residuals for a spherically symmetrical Earth model.

1. Introduction

Global models of seismic velocity heterogeneity have emerged in the past decade which show significant deviations from spherical symmetry in Earth's structure. Most of the models for the upper mantle are primarily derived from surface waves and yield information about shear-velocity structure [e.g. *Woodhouse and Dziewonski*, 1984, *Zhang and Tanimoto*, 1993]. As the quality of data and their coverage increases more detail is included in the models. Global models currently claim to resolve structures as small as 1000 km in lateral extent [*Zhang and Lay*, 1996], although some authors give a more conservative resolution estimate [*Trampert and Woodhouse*, 1995]. Regional models, on the other hand, resolve structures to considerably smaller scales, i.e. hundreds of kilometres [e.g. *Zielhuis and Nolet*, 1994, *Debayle and Leveque*, 1997]. The strength of heterogeneity in the models increases as more detail is included. The global model RG5.5 of *Zhang and Tanimoto* [1993] has about $\pm 3\%$ variation at 110 km depth while the regional model of *Zielhuis and Nolet* [1994] has about $\pm 6\%$ variation at the same depth.

The strength of heterogeneity in global models falls off rapidly below a few hundred km depth. Typically the heterogeneity is $\pm 3\%$ around 100 km depth, but less than $\pm 1\%$ in the transition zone. Using travel times, which potentially offer higher resolution, *Gudmundsson et al.* [1990] found that the level of heterogeneity at large and intermediate scales (scale > 400 km) drops by about a factor of two at a depth of 300 km. They also concluded that smaller-scale heterogeneity is concentrated even more strongly near the Earth's surface.

One important source of information about the structure of the upper mantle are regional refraction profiles (of length > 2500 km) and body-wave travel times and waveforms from earthquakes which can be aligned along a profile of comparable length and interpreted as a refraction profile [e.g. *Helmberger and Wiggins*, 1971, *Grand and Helmberger*, 1984, *Walck*, 1984, *Mechie et al.*, 1993, *Kennett et al.*, 1994]. A comprehensive summary of the one-dimensional models which result from this approach can be found in *Nolet et al.* [1994]. After comparing a large number of models from varied tectonic environments they conclude that there is clear evidence for lateral heterogeneity which correlates with surface tectonics. The model differences persist to 300-400 km depth. They also point out that local studies generally produce

larger velocity anomalies than are found in global surface-wave models. This suggests that global models provide only a partially complete picture of the upper mantle, with intermediate-scale features filtered out and larger-scale features damped.

Regional tomography based on travel times has revealed important aspects of subducted slab structures in the mantle [e.g. *Spakman et al.*, 1988, *Zhou and Clayton*, 1990, *van der Hilst et al.*, 1991, *Zhao et al.*, 1992]. Slabs appear as fast anomalies which display a variation of morphology, particularly at depth. In some instances evidence for necking and detachment is seen, some slabs appear to be driven through the phase transition at 660 km depth while others pile up in the transition zone. While it is clear that slab morphology is complex some of the conclusions from regional delay-time tomography would be strengthened by rigorous hypothesis testing. The most reliable slab images are based on compressional waves. The strength of the anomalies for compressional velocity is as high as $\pm 5\%$, fast velocities defining the slab while the slower velocities are generally found in the shallow mantle wedge.

The picture that has emerged of the upper mantle has shear velocity vary by $\pm 3\%$ on large scales (> 1000 km) and another $\pm 3\%$ on intermediate scales (400 - 1000 km). Significant heterogeneity persists at scales smaller yet. Variations of compressional velocity are less well known, but are probably comparable while somewhat less than the variations of shear velocity. Subducting lithosphere possesses an anomaly of about 5%. Clearly, such strong heterogeneity will significantly affect the travel times of body-wave phases, including those most commonly used in earthquake location. Accounting for the effect of lateral heterogeneity can therefore significantly improve the quality of event location. *Fujita et al.* [1981] estimate that the structure of a slab may affect the location of earthquakes within it by as much as 40 km. For teleseismic P waves that translates into a time effect of about 4 seconds.

It is evident from even the first generation of global models and from a comparison of early one-dimensional models from different tectonic regions that the large-scale features of shallow upper-mantle structure correlate well with surface tectonics [*Romanowicz*, 1991, *Nolet et al.*, 1994]. Old continental cores have deep fast roots extending into the upper mantle and spreading centers are underlain by slow mantle rocks, although the depth extent is subject to debate. *Nataf and Ricard* [1996] attach much signifi-

cance to the correlation of tomographic models for the upper mantle with surface tectonics when they suggest a velocity model (3SMAC) for the upper mantle based on a tectonic, crustal thickness and sedimentary thickness regionalization, geophysical modeling and constraints from other fields of earth sciences than seismology. Their approach is justified by *Ricard et al.* [1996] who show that the 3SMAC model accounts well for normal-mode frequencies and phase-velocity observations world wide.

Like *Nataf and Ricard* [1996] we regard the strong correlation of surface tectonics and velocity heterogeneity at shallow depths in the mantle, where the heterogeneity is strongest, as a potential constraint on global tomography. In this paper we apply a regionalization as a constraint to upper-mantle structure derived from travel times. We seek a simple model (few model parameters) to account for as much of upper-mantle heterogeneity as possible. Our objective is to build a regionalized reference model for travel-time corrections.

2. Strategy

Accounting for the effects of velocity heterogeneity on travel times and thus event location must include the main features of the velocity structure and remain a simple procedure in order to be efficient. We attempt to meet these prerequisites with the following strategy:

We use the high level of correlation of global velocity models with surface tectonics to define the main features of Earth structure. A detailed regionalization defines irregularly shaped bodies on the Earth's surface which in turn define discrete model parameters. With irregular sampling of the regionalization we can represent irregular bodies with a large range of length scales. The sampling is dense where needed (i.e. at continental margins, island arcs and within tectonic continents), and sparse elsewhere (e.g. intraregional, oceanic).

Delaunay and Voronoi tessellation are recipes for connecting nodes in an irregular grid. In both cases the tessellation is uniquely defined and automatically generated given an arbitrary set of nodes. The Delaunay tessellation generates a space-filling set of tetrahedra with nodes at their vertices. The Voronoi tessellation defines a polyhedron around each node with faces on the median bisectors between the node in question and its natural neighbours. [*Okabe et al.*, 1992]. Delaunay tetrahedra are suitable to define the

volume of an object which surface has been sampled. Voronoi polyhedra are suitable to define the volume associated with a discrete sample of a varying field. We use a combination of a Delaunay tessellation and a Voronoi tessellation to define discrete regions belonging to the various tectonic types [*Sambridge and Gudmundsson*, 1997]. This allows us to significantly reduce the number of parameters needed to represent the complex regions compared to a regular grid for example. Efficient algorithms are available for navigation and book keeping in irregular grids composed of Delaunay tetrahedra or three-dimensional Voronoi cells [*Sambridge et al.*, 1995].

We use a select data set of travel times from well located events and nuclear explosions in order to alleviate the mapping of mislocation into structure. We invert these data for an irregularly parameterised, regionalised upper-mantle (RUM) model. Our objective is not to find the best possible model, but to find the simplest model that still contains enough information about structure to be useful for generating corrections to travel times used in event location.

Teleseismic travel times can then be corrected for this model by a relatively simple and efficient ray-tracing procedure.

3. Method

3.1. Regionalization

Figure 1 shows the regionalisation. It is based on maps published by *Sclater et al.* [1980] and *Jordan's* [1981] GRT1 regionalization. Eight tectonic regions are defined. The ocean is divided into three age provinces, the same as the GRT1 regionalization, except at a resolution of two degrees compared to five degrees in GRT1. The continents are divided into 5 regions according to age, four regions of low volcanic and earthquake activity, in addition to a region termed tectonic continent where seismic and volcanic activity is high. We have termed the regions Young Continent, Intermediate-age Continent, Old Continent and Ancient Continent as their separation in time does not strictly correspond to boundaries between geological eras. The age boundaries are listed in Figure 1 and were selected by comparing the age zonation of the continents with tomographic images of the upper mantle [e.g. *Woodhouse and Dziewonski*, 1984]. The regionalization is very similar to the regionalization used by *Nataf and Ricard* 1996 to generate the 3SMAC model. We have perhaps unconventionally termed the Iceland-Faeroe-Greenland Ridge

continental because of its highly anomalous crustal thickness for oceanic crust (25-35 km according to *Bott and Gunnarsson* [1980]). We have also defined the ridges of the Tasman Sea as continental. A future improvement of the regionalization would include all oceanic ridges and plateaus as a separate oceanic region(s). This regionalization has obvious limitations. Parts of the age mapping involve significant interpolation of geochronological data. Details are left out where limited by the resolution. For the purposes of global seismology much more detail is not justified because teleseismic delay times or surface-wave dispersion will not be able to resolve it.

The regionalization is initially represented by 16200 parameters. Roughly a quarter of these are then selected to parameterise the boundaries between the regions (4100 parameters) (see Figure 1b). The boundaries are all parameterised with a two-degree resolution except the boundaries between oceanic regions. Thus, the density of parameterisation is high where we expect potentially sharp contrasts, i.e. at continental margins and boundaries between tectonic and atectonic regions, and low where we don't, i.e. within the oceans. Figure 1b shows the boundaries of the Voronoi cells around the selected samples of the regionalization. The figure contains about 4100 Voronoi cells. Figure 1c shows how the original regionalization is reproduced by the 4100 selected cells. The full complexity of Figure 1a is reproduced in Figure 1c with only about a quarter of the number of parameters in the original. Each Voronoi cell is taken to encompass a region of uniform velocity at each depth. The regionalization is extended from the surface to a depth of 660 km to span the whole of the upper mantle.

This regionalization is not taken to be a complete description of velocity heterogeneity. We ignore lower-mantle heterogeneity because extrapolation of surface tectonics into the lower mantle would not be warranted and because the strength of heterogeneity decays rapidly with depth in the upper mantle. Shallow small-scale structure internal to tectonic regions is not accounted for by this regionalisation. In island arc regions such structures are modelled as subducting slabs. In continental regions such structures are accounted for by station corrections.

3.2. Subducting slabs

Subducting slabs are significant structures in the upper mantle which are clearly oblique and cannot be included in a two-dimensional regionalization as above. Most of Earth's seismicity occurs in or around

subducting slabs. Slabs do affect travel times significantly and their presence can, if not accounted for, cause a systematic mislocation of island-arc earthquakes by as much as 40 km [*Fujita et al.*, 1981]. We have included oblique slab structures in our parameterization of the upper mantle as the ninth region. First we contoured slab-related seismicity world wide. A total of 24 separate slab bodies were defined (see Figure 2a). Examples of slab contours are presented in Figure 2b for the slabs of the northwest Pacific. The contours are drawn at fifty km depth intervals and such that they lie near the top of the seismogenic region. We used the relocated catalog of *Engdahl et al.* [1997] as well as a filtered version of the ISC catalog (based on location quality) to define the seismicity. Neither catalog is complete and both contain significant gaps which are difficult to interpret. These gaps were not interpolated if they exceed a few hundred km in size. The slab contours obviously do not define a slab where there is no seismicity. It is difficult to envisage the thermal anomaly of subducting lithosphere to terminate as abruptly as the seismicity in many places. Thus our model of slabs is likely to be incomplete. However, slabs are defined where we most need them, i.e. where the earthquakes occur and for which travel-time corrections are needed.

The slab contours define a surface which we take to define the top of the slab (or what used to be the top of the oceanic lithosphere before subduction). We then define a complementary surface assuming that the slab is 200 km thick. This is a simplification of slab geometry, particularly at depth. No necking or slab detachment is allowed for, while it is possible that that type of morphology is associated with gaps in seismicity [*Widiyantoro and van der Hilst*, 1996]. Slabs are not allowed to pile up in the transition zone as appears to be the case for e.g. the Izu-Bonin slab [*van der Hilst et al.*, 1993].

Projecting the original surface 200 km along its local normal occasionally results in the folding of the original surface. Such folds were simply edited out interactively with a graphics tool. We sample the contours using nodes placed at a lateral spacing of about 10 km. These nodes are not internal to the slabs as we define them, but on their surface. In this case constant-velocity Voronoi cells as were used in the surface parameterization are not suitable to describe their complex geometry, because these cells surround each node and would necessarily extend the slab and change its volume. Instead we place the nodes of the slabs in a global coordinate system and

construct the three-dimensional Delaunay tessellation for the approximately 23,000 slab samples for all 24 individual slab structures. Those Delaunay tetrahedra which join the two surfaces of the same slab structure then define the volume of slabs in the upper mantle. The Delaunay tetrahedral representation of the slabs of the northwest Pacific is shown in perspective in Figure 2b as an example. These are some of the larger and deeper slabs which display significant complexity in shape.

3.3. Summary of parameterization

In summary the parameterization of the upper mantle consists of two distinct elements: Delaunay tetrahedra to define slabs and a two-dimensional grid of Voronoi cells extended uniformly to a depth of 660 km to define tectonic regions. The slabs are overlaid on the regionalization. To determine which type of environment a given point (along a ray) is in we first detect if it is within a slab. If it is not, its position in the regionalization is determined. Thus we represent complex structures efficiently and economic algorithms are available to locate any arbitrary point in either irregular grid [see *Sambridge and Gudmundsson, 1997*]. The parameterisation includes fine spatial features in subduction zones on a scale of 10 km and also tectonic age provinces a few thousand kilometers across. Its dynamic range is thus two to three orders of magnitude.

3.4. Data selection

We use a select data set of travel times from well located events and nuclear explosions in order to alleviate the mapping of mislocation into structure. This is of particular importance in building a reference Earth model because observed biases in earthquake location can be significant and can inject artificial structural signal into travel times on the order of seconds. The events we use are the 105 events of the test-data set used by *Kennett and Engdahl [1991]* supplemented with 92 large earthquakes to get a more even sampling of the globe and the 9 tectonic regions. The criterion for the selection of these events was that they be recorded by a large number of globally distributed stations. Their locations are taken from nuclear agencies, local and regional networks, and if neither of the above is available from the relocated catalog of *Engdahl et al. [1997]*. They reassociated ISC data, included pP and pwP phases in the location, used IASP91 [*Kennett and Engdahl, 1991*] and subjected locations to stringent fitness criteria. We use

only teleseismic P and PKIKP arrivals (first arrivals) for the compressional-velocity model and teleseismic S arrivals for the shear-velocity structure. We use only picks reported to the ISC as impulsive to insure a high degree of robustness of individual picks.

All the data have been corrected for the Earth's ellipticity [*Kennett and Gudmundsson, 1996*], for station elevation, and for surface topography/bathymetry in the case of phases reflecting off the Earth's surface. We have prepared data from other phases such as pP, PP, PcP, PKP, sS, SS, ScS, and SKS from the 197 events in this select data set.

Figure 3 shows a map of the 197 events used together with the regionalization. The events are grouped into three categories. First there are 21 nuclear and chemical explosions (displayed as white stars in the figure). Their locations will be taken to be fixed. Then there are 39 earthquakes which are well located with local observations in a local velocity model. They are displayed as white dots. Their locations are also assumed fixed. The remaining 137 events (shown as black dots) are located using teleseismic observations and are allowed to vary in their origin time and depth.

We reference travel-time residuals to the AK135 model [*Kennett et al., 1995*] and reassociate all impulsive picks reported to the ISC for the above events. We find a surprising number of events with a significant mean residual. This is surprising because AK135 is almost identical in the mantle to IASP91 which *Engdahl et al. [1997]* used for their locations. The explanation must lie in a difference in data selection. We for example include PKIKP and not pP. We do not associate pwP. The large number of events with a significant apparent origin-time shift led us to allow origin time to be a free parameter in our inversion for regionalized structure. Allowing origin time to vary independently for P and S is equivalent to allowing for a relocation in source depth and origin time. We find 14291 P and PKIKP picks and 2608 S picks which satisfy our selection criteria.

4. Inversion - data reduction

We solve a linearized inverse problem. A higher order approach is not warranted because ray bending critically depends on velocity gradients which are artificially represented by our parameterization. We sample depth ten times at 66 km spacing and seek 9 independent velocity profiles, one for each of the eight tectonic regions as well as slabs. We use a

standard damped-least-squares inversion procedure. In regions with limited depth distribution of sources teleseismic rays give limited depth resolution in the upper mantle. We cannot well resolve ten independent parameters except in subducting slabs, where there is a distribution of events in depth. Since the level of heterogeneity in the upper mantle is strongly concentrated near the surface [e.g. *Gudmundsson et al.*, 1990], in the top 300-400 km, we have projected the depth profiles on to a set of four Gaussian basis functions which are not allowed to put structure in the lower half of the upper mantle. In effect we are implementing depth-dependent damping. We argue that this is in line with our general approach of applying stringent geometrical constraints to the inversion based on a priori information. The basis functions are not orthogonal in themselves but decompose into a fourfold orthogonal basis. The model for subducted lithosphere is allowed to vary throughout the upper mantle. The results we present are moderately damped. The trade off employed to select the damping was that of variance reduction versus damping coefficient (which varies monotonically with resolution). The damping was selected where it started to significantly affect the variance reduction (lowered by 10 – 20%). The relocation component of the inverse problem is scaled to allow for virtually full removal of average residuals for each event.

For the P-wave data origin-time shifts of 137 events out of 192 account for about 55% variance reduction (see Table 1). An undamped inversion allowing for 10 independent depth parameters in each region achieves a 19% variance reduction. Limiting the degrees of freedom to four per region via the Gaussian basis reduces the variance reduction to 16%. We have damped the solution to yield a variance reduction of 14%. For the S-wave data the pattern is similar, with the damped model achieving a 10% variance reduction. For the S-waves the variance is considerably higher than for the P-waves and the relative variance reduction achieved by origin time shift is much less than for the P-wave data.

We find that none of the minor data sets consisting of the compressional pP, PP, PcP, and PKP phases or the shear sS, SS, ScS, and SKS phases improve resolution significantly nor are they consistent with the major data sets of P, PKIKP, or S phases. The RUM model does not significantly reduce the variance of the minor data sets.

As a final step in the data reduction we estimate station corrections to be applied after correction for

the RUM model. We evaluate a correction only for stations with more than 4 picks reported. The station correction is simply the average residual for each station after correction for the RUM model. This step achieves a further variance reduction of 16% and 11% for the P waves and S waves, respectively. Table 1 summarizes the reduction of the mean and variance of the P- and S-wave data by the individual steps of the data reduction. Figure 4 shows a histogram of time residuals before and after data reduction. We note that the quoted variance reduction applies to individual picks, not summary rays. We also note that the remaining variance in the data is comparable to, but slightly higher than the estimates of noise variance in the ISC data for teleseismic P and S waves by *Gudmundsson et al.* [1990] and *Davies et al.* [1992].

5. Results

The results of the inversion are shown in Figure 5 and Table 2. In Figure 5 each function of depth represents a velocity perturbation for a given tectonic region. Figure 5a shows the results for P waves, Figure 5b for S waves. The results are plotted as a relative velocity perturbation (in percent) with one standard deviation error bars assuming that the error variance is as given by *Gudmundsson et al.* [1990] for the teleseismic P-wave data, i.e. $1s^2$, and by *Davies et al.* [1992] for teleseismic S-wave data, i.e. $4s^2$. Table 2 also list the results as relative velocity perturbations.

The results for compressional velocity are encouraging. Slabs appear as a continuous fast anomaly throughout the upper mantle except at the top where we have tectonic crust rather than a true slab and where the result is probably affected by the slow mantle wedge. The amplitude of the slab structure is 2-3% velocity perturbation. This is assumed to be uniform over a thickness of 200 km. The subducting lithosphere is probably not that thick at shallow depths, but the associated thermal anomaly diffuses with time or depth. Furthermore, it would peak above its average level. The 2-3% level of perturbation in the slabs would thus be consistent with a somewhat higher peak perturbation in the core of the slabs, possibly as high as 5%. This is a reasonable level of perturbation compared to predictions on the basis of thermal modeling. Other features of the results are also encouraging. The oceans are slow with old oceans developing a fast lithosphere. Tectonic continent and young continent are also slow and essentially indistinguishable. This is of interest because, e.g.

Nataf and Ricard [1996] do not make a distinction between those regions in their regionalization. That decision appears to have been justified. Currently active continental margins and island arcs are not clearly distinguishable from other Mesozoic continental regions. Intermediate-age continents have developed a fast lithosphere while their asthenosphere looks much like that of young continental regions. There is no resolvable structure underneath old continents suggesting that AK135 (and IASP91) are representative of continents in that age range. This is interesting and not surprising because the AK135 and IASP91 models were not designed to represent average Earth structure but rather as effective reference models for travel time prediction deliberately biased according to the distribution of stations. Ancient continents are fast, but not to a great depth, only about 200 km. Note, however, that depth resolution is limited. It should be noted that we have not corrected for crustal structure so the model should be interpreted to include crustal signature. The number of degrees of freedom in the compressional model is 22 (trace of resolution matrix).

The RUM model is best compared to individual one-dimensional models by comparing the integral travel-time anomaly at vertical incidence. The RUM model gives a range from -0.25 to 1.16 seconds relative to AK135. The negative (fast) extreme corresponds to ancient continent while the positive (slow) extreme corresponds to young ocean. Shield models such as *S25* of *Lefevre and Helmberger* [1989] for the Laurentian shield, *quartzn* of *Mechie et al.* [1993] for the Fennorussian shield, and *flsb* of *Kennett et al.* [1994] for the Australian shield, have an average travel-time anomaly of about -1 second. The tectonic models *t7* and *t9* of *Burdick and Helmberger* [1978] and *Burdick* [1981] average at about 0.6 seconds. Tectonic continent in RUM has an anomaly of about 0.5 seconds. The oceanic models *gca* and *cjf* of *Walck* [1984, 1985] average at 0.2 seconds. The range is the same for the elements of RUM and the one-dimensional models, i.e. about 1.5 seconds. The time anomaly for tectonic continent is similar in RUM as in tectonic one-dimensional models, but for shield models and oceanic models there is a shift of about 1 second. We suggest a few potential explanations of this discrepancy. Stations and events are co-located in tectonic regions. Therefore, one-dimensional refraction type studies enjoy good constraints on shallow structure. This is not the case in shield regions or oceanic regions. The stations are removed from the seismicity.

Therefore, the shallow constraint is poor and/or the paths tectonically mixed at short distance. From Figure 3 it is evident that we do not have any events in young oceanic regions that are constrained by local observations. Neither do we have such events in shield regions. The RUM model may therefore suffer from a lack of absolute reference in those regions. On the other hand stations in shield regions record many of the locally constrained events which adds absolute constraint to the shields. The RUM model represents an average property for all regions of the same tectonic type. Station corrections (discussed below) indicate that considerable variability exists among regions of the same type. It is possible that published one-dimensional, regional models are not representative of their regions.

The results for the shear velocity are less well constrained and more poorly resolved. This is because of fewer and poorer data. In order to render the result interpretable in the sense of suppressing noise sufficiently so that model exceeds uncertainty in amplitude, we have had to damp the S-wave model more heavily than the P-wave model. The number of degrees of freedom in the shear-velocity model is only 11. Still subducted lithosphere extends as a fast anomaly of reasonable amplitude throughout the upper mantle, old continental cores are fast and oceans are slow. The absence of a lithosphere in the oceans may be ascribed to lower resolution. The reduced level of coherency in the transition from young ocean to ancient continent can be understood in terms of poorer constraint. The range of the predicted vertical travel-time anomaly for RUM-S is -2.1 seconds for ancient continents, which is comparable to the *sna* model of *Grand and Helmberger* [1984] and the *njpb* model of *Kennett et al.* [1994] for the North-American and Australian shields, respectively, to about 2 seconds in the oceans. The vertical time delay for the tectonic regions of RUM-S is only about 1 second while the *tna* model of *Grand and Helmberger* [1984] has a 7.5 second delay. Here the agreement in the tectonic region is of the same sense but poor in amplitude.

We refrain from interpreting the results beyond pointing out that despite strict geometrical constraints on the lateral extent of anomalies the level of velocity perturbation is reasonable. Any comparison between the results for P waves and S waves would have to take into account the difference in the damping of the two models. The S-wave model is more heavily damped than the P-wave model, which qualitatively explains why the modeled perturbation in shear velocity does

not clearly exceed the perturbation of compressional velocity (we would expect the former to exceed the latter by 50 – 100%). Surface waves may be better suited to study the shear-velocity heterogeneity of the upper mantle than delay times.

Our confidence in the results is much higher for compressional velocity than shear velocity. It is interesting to display the model in its full three-dimensionality. Figure 6 shows a pair of cross sections through the RUM-P model. In Figure 6a the section cuts through the Tongan slab, the Banda Sea slab near its sharp bend, through some shallow slabs in the Philippines, and through the Andean slab. It also grazes through the Hellenic slab. In Figure 6b the cross section cuts through the Sumateran slab, shallow slabs in the Philippines and the slabs of the northwestern Pacific along strike. Subducting lithosphere constitutes a major feature of the RUM model at the extremity of fast perturbations. Their geometry is imposed. This may render the estimate of their overall velocity perturbation more robust than in less constrained delay-time models of slab regions. The velocity perturbations in the upper mantle range between $\pm 2.5\%$, which is similar to what one might expect on the basis of estimates of $\nu = \partial \ln V_s / \partial \ln V_p$ and the heterogeneity pattern as modeled from surface-wave data.

Figure 7 shows the station corrections for P-wave residuals. A corresponding map for S-wave residuals is not presented because of its sparseness and how poorly constrained we regard the shear-velocity model. Clearly a significant signal is left in the data after inversion for regionalized structure. Note for example that a fast anomaly remains within the Laurentian craton. On the other hand the African cratons are left with slow anomalies. This is in agreement with results of global, surface-wave tomography which has the African cratons show up much less clearly than e.g. the Laurentian, Fennorussian and Australian cratons. Some tectonic regions are left with systematically fast residuals while others are slow. Considerable scatter is evident within some regions. Clearly all regions of the same type are not the same. Furthermore, small-scale structure within individual regions is not modeled, but instead absorbed in station corrections.

6. Locating known events

To test the success of the RUM model as a reference for teleseismic travel times we relocate 19 of the 21 explosions in the data set. The locations of

those 19 explosions can be regarded as known [Kennett and Engdahl, 1991]. We compare relocations using teleseismic P residuals which are referenced to the AK135 model, to the RUM-P model, and to the RUM-P model as well as station corrections. We relocate only the epicenter, i.e. the depth is fixed at the reported depth. Many of the earlier events in particular have a very unevenly distributed sampling. The locations become much more robust by evening this distribution or declustering it. For each event we construct a kernel matrix which is $n \times 3$, where n is the number of observations. The three elements of each row are the sensitivity to relocation in latitude, longitude, and origin time (the last is always -1). We bin the first and second columns of the kernel matrix four times each. After removing outliers (residuals more than 5 seconds away from mean of bin) we calculate an average residual for each of the sixteen bins downweighting emergent picks. This procedure has a similar effect in improving the robustness of location to the weighting scheme employed by Smith and Ekström [1995]. We use only P residuals in the teleseismic range. Finally, we solve a linearized relocation problem giving all bins equal weight. In effect we are declustering the sampling of the focal sphere as seen from the event to minimize biases in the relocation. The procedure of the relocation is the same for all events and for all levels of data reduction. The results of the relocations are listed in Table 4 as misfit in origin time (seconds) and length of the horizontal mislocation vector (kilometers) and summarized at the bottom as the root-mean-square (rms) misfit in time and horizontally. The mislocations of individual events using AK135 for reference are similar to the mislocations reported by Kennett and Engdahl [1991]. In other words the level of robustness of the location procedure is similar although the procedures differ. After correction of residuals for the RUM three-dimensional model the mislocations are significantly improved, i.e. by about 20%. Applying the RUM station corrections reduces the rms misfit by a further 33%. While it is tempting to compare the rms misfit to that achieved by Smith and Ekström [1995] in absolute terms that would have limited meaning because the location procedure is not the same.

A significant level of reduction of mislocation is related to the application of station corrections. The RUM model's usefulness for travel-time corrections lies in the fact that the corrections are derived from a model and that it effectively implements corrections for near-source structure, event corrections. Where

a stations history does not allow for a robust station correction the model provides a reasonable means of predicting that station correction to first order.

7. Conclusions

We have described upper-mantle structure with 22 degrees of freedom (compressional velocity) and 11 degrees of freedom (shear velocity) and managed to explain a significant portion of the apparent structural variance in travel-time data. The data are individual, not summary-ray data. S-wave residuals give results similar to the P-wave velocity variations, but less well constrained. Our parameterization in effect imposes complex spatial constraints on this inversion for upper-mantle structure which we can think of as a priori information, i.e. the presumption that the upper mantle can be regionalized as we have done. The success of the inversion justifies those constraints. The remaining station residuals point to the fact that this regionalized description is not complete, however, and that on order of half the structural signal in the data is explained by it. The RUM model is derived as a regionalized reference model for the upper mantle. It should prove useful for correcting travel times for upper-mantle heterogeneity to first order. Improvements in the location misfit of known explosions demonstrates the models success. The RUM model can also be used as a starting point for tomography, an initial starting model.

The RUM model is tabulated in Table 2. We have also prepared a home page on the world-wide web at <http://rses.anu.edu.au/RUM/rum.html> containing graphical information, software and software description. The software includes codes to calculate travel-time corrections for the RUM model for a variety of phases including other first order effects such as due to the Earth's topography.

Acknowledgments. We are indebted to Ken Creager for many useful discussions about slab morphology and for teaching us to use his interactive contouring routines for MATLAB. We acknowledge useful discussions with Brian Kennett. This work was supported in part by a grant from the U.S. Air Force Office of Scientific Research F49620-94-1-0022, F49620-94-1-0110.

References

- Bott, M.H.P. and K. Gunnarsson, Crustal structure of the Iceland-Faeroe Ridge, *J. Geophys.*, **47**, 221-227, 1980.
- Burdick, L.J. and D.V. Helmberger, The upper-mantle P-velocity structure of the western United States, *J. Geophys. Res.*, **83**, 1699-1712, 1978.
- Burdick, L.J., A comparison of the upper-mantle structure beneath North America and Europe, *J. Geophys. Res.*, **86**, 5926-5936, 1981.
- Davies, J.H., Ó. Gudmundsson, and R.W. Clayton, Spectra of mantle shear velocity structure, *Geophys. J. Int.*, **108**, 865-882, 1992.
- Debayle, E. and J.J. Leveque, Upper mantle heterogeneities in the Indian Ocean from waveform inversion, *Geophys. Res. Lett.*, , in press, 1997.
- Engdahl, E.R., R. van der Hilst, and R. Buland, *J. Geophys. Res.*, in press, 1997.
- Fijita, K., E.R. Engdahl, and N.H. Sleep, Subduction-zone calibration and teleseismic relocation of thrust-zone events in the central Aleutian Islands, *Bull. Seism. Soc. Am.*, **71**, 1805-1828, 1981.
- Grand, S. and D.V. Helmberger, Upper-mantle shear structure of North America, *Geophys. J. R. Astron. Soc.*, **76**, 399-438, 1984.
- Gudmundsson, Ó., J.H. Davies, and R.W. Clayton, Stochastic analysis of global travel time data: Mantle heterogeneity and errors in the ISC data, *Geophys. J. Int.*, **102**, 25-43, 1990.
- Helmberger, D.V. and R.A. Wiggins, Upper-mantle structure of the midwestern United States, *J. Geophys. Res.*, **76**, 3229-3245, 1971.
- Jordan, T., Global tectonic regionalisation for seismological data analysis, *Bull. Seism. Soc. Am.*, **71**, 1131-1141, 1981.
- Kennett, B.L.N. and E.R. Engdahl, Traveltimes for global earthquake location and phase identification, *Geophys. J. Int.*, **105**, 429-465, 1991.
- Kennett, B.L.N., Ó. Gudmundsson, and C. Tong, The upper mantle S and P velocity structure beneath northern Australia from broad-band observations, *Phys. Earth Planet. Inter.*, **86**, 85-98, 1994.
- Kennett, B.L.N., E.R. Engdahl, and R. Buland, Travel times for global earthquake location and phase association, *Geophys. J. Int.*, **122**, 108-124, 1995.
- Kennett, B.L.N. and Ó. Gudmundsson, Ellipticity corrections for seismic phases, *Geophys. J. Int.*, **127**, 40-48, 1996.
- Mechie, J., A.V. Egorkin, K. Fuchs, T. Ryberg, L. Solodilov, and F. Wenzel, P-wave mantle velocity structure beneath northern Eurasia from long range recordings along the profile Quartz, *Phys. Earth Planet. Inter.*, **79**, 269-286, 1993.
- Lefevre, L.V. and D.V. Helmberger, Upper mantle P-velocity structure of the Canadian shield, *J. Geophys. Res.*, **94**, 17,749-17,765, 1989. velocities and anisotropies, *J. Geophys. Res.*, **96**, 20,337-20,351, 1991.
- Nataf, H.-C. and Y. Ricard, 3SMAC: an a priori tomographic model of the upper mantle based on geophysical modeling, *Phys. Earth Planet. Inter.*, **95**, 101-122, 1996.
- Nolet, G., S.P. Grand, and B.L.N. Kennett, Seismic het-

- erogeneity in the upper mantle, *J. Geophys. Res.*, **99**, 23,753-23,766, 1994.
- Okabe, A., B. Boots, and K. Sugihara, *Spatial-tessellation concepts and applications of Voronoi diagrams*, xxx pp., J. Wiley Sons, Chichester, 1992.
- Ricard, Y., H.-C. Nataf, and J.-P. Montagner, The tree-dimensional seismological model a priori constrained: Confrontation with seismic data, *J. Geophys. Res.*, **101**, 8457-8472, 1996.
- Romanowicz, B., Seismic tomography of the Earth's mantle, *Annu. Rev. Earth Planet. Sci.*, **19**, 77-99, 1991.
- Sambridge, M., J. Braun, and H. McQueen, Geophysical parameterisation and interpolation of irregular data using natural neighbours, *Geophys. J. Int.*, **122**, 837-857, 1995.
- Sambridge, M., and Ó. Gudmundsson, Tomography with irregular cells, *J. Geophys. Res.*, submitted, Jan. 1997.
- Sclater J.G., C. Jaupart, and D. Galson, The heat flow through oceanic and continental crust and the heat loss of the Earth, *Rev. Geophys.*, **18**, 269-311, 1980.
- Smith, G.P. and G. Ekström, Improving teleseismic event locations using a three-dimensional Earth model, *Bull. Seism. Soc. Am.*, **86**, 788-796, 1996.
- Spakman, W., M.J.R. Wortel, and N.J. Vlaar, The Hellenic subduction zone: a tomographic image and its geodynamic implications, *Geophys. Res. Lett.*, **15**, 60-63, 1988.
- Trampert, J. and J.H. Woodhouse, Global phase velocity maps of Love and Rayleigh waves between 40 and 150 seconds, *Geophys. J. Int.*, **122**, 675-690, 1995.
- van der Hilst, R., R. Engdahl, W. Spakman, and G. Nolet, Tomographic imaging of subducted lithosphere below northwest Pacific island arcs, *Nature*, **353**, 37-43, 1991.
- van der Hilst, R., E.R. Engdahl, and W. Spakman, Tomographic inversion of P and pP data for aspherical structure below the northwest Pacific region, *Geophys. J. Int.*, **115**, 264-302, 1993.
- Walck, M.C., The P-wave upper mantle structure beneath an active spreading center: The Gulf of California, *Geophys. J. R. Astron. Soc.*, **76**, 697-723, 1984.
- Walck, M.C., The upper mantle beneath the north-east Pacific rim: a comparison with the Gulf of California, *Geophys. J. R. Astron. Soc.*, **81**, 243-276, 1985.
- Widiyantoro, S. and R. van der Hilst, Structure and evolution of lithospheric slab beneath the Sunda arc, Indonesia, *Science*, **271**, 1566-1570, 1996.
- Woodhouse, J.H. and A. Dziewonski, Mapping the upper mantle: Three-dimensional modeling of Earth structure by inversion of seismic waveforms, *J. Geophys. Res.*, **89**, 5953-5986, 1984.
- Woodhouse, J.H. and J. Trampert, New geodynamical constraints from seismic tomography, *Earth Planet. Sci. Lett.*, submitted, 1996.
- Zhang, Y.-S. and T. Tanimoto, High-resolution global upper mantle structure and plate tectonics, *J. Geophys. Res.*, **98**, 9793-9823, 1993.
- Zhang, Y.-S. and T. Lay, Global surface wave phase velocity variations, *J. Geophys. Res.*, **101**, 8415-8436, 1996.
- Zhao, D.-P., A. Hasegawa, and S. Horiuchi, Tomographic imaging of P and S wave velocity structure beneath northeastern Japan, *J. Geophys. Res.*, **97**, 19,909-19,928, 1992.
- Zhou, H.-W. and R.W. Clayton, P and S travel time inversions for subducting slab under the island arcs of the northwest Pacific, *J. Geophys. Res.*, **95**, 6829-6851, 1990.
- Zielhuis, A. and G. Nolet, Shear-wave velocity variations in the upper mantle beneath central Europe, *Geophys. J. Int.*, **117**, 695-715, 1994.

Ó. Gudmundsson and M. Sambridge, Research School of Earth Sciences, The Australian National University, Canberra, ACT 0200, Australia. e-mail: oli@rses.anu.edu.au, malcolm@rses.anu.edu.au)

March XX, 1997; revised XX XX, 1997; accepted XX XX, 1997.

Figure 1. Tectonic regionalization and its reproduction using Voronoi cells. a) the regionalization as designed on a 2x2 degree grid using 16200 parameters, b) boundaries of Voronoi cells around 4100 nodes selected to sample the details of the regionalization, c) the regionalization as represented by 4100 Voronoi cells.

Figure 2. a) Contoured subducting slabs with topographic/bathymetric map shown for reference. b) Contours of slabs of the northwest Pacific with topographic/bathymetric map for reference. c) A perspective view of the slabs of the northwest Pacific from above and the southwest. The edges of individual Delaunay tetrahedra are shown in black.

Figure 3. Epicenters of the 197 events used in this study with regionalization for reference. White stars represent artificial explosions, white dots represent events located within a regional network of stations, and black dots represent events located using global observations.

Figure 4. Histograms show distribution of time residuals before and after inversion/data reduction. a) P-wave residuals, b) S-wave residuals.

Figure 5. The RUM velocity model presented as percentile velocity perturbation from the AK135 model. a) For compressional velocity. b) For shear velocity. The shaded area represents the range $\pm\sigma$, where σ is one standard deviation.

Figure 6. Two cross sections through the three-dimensional RUM model showing the range of velocity perturbations and demonstrating the types of bodies included in the model. Note that this global model contains clear slabs in the upper mantle.

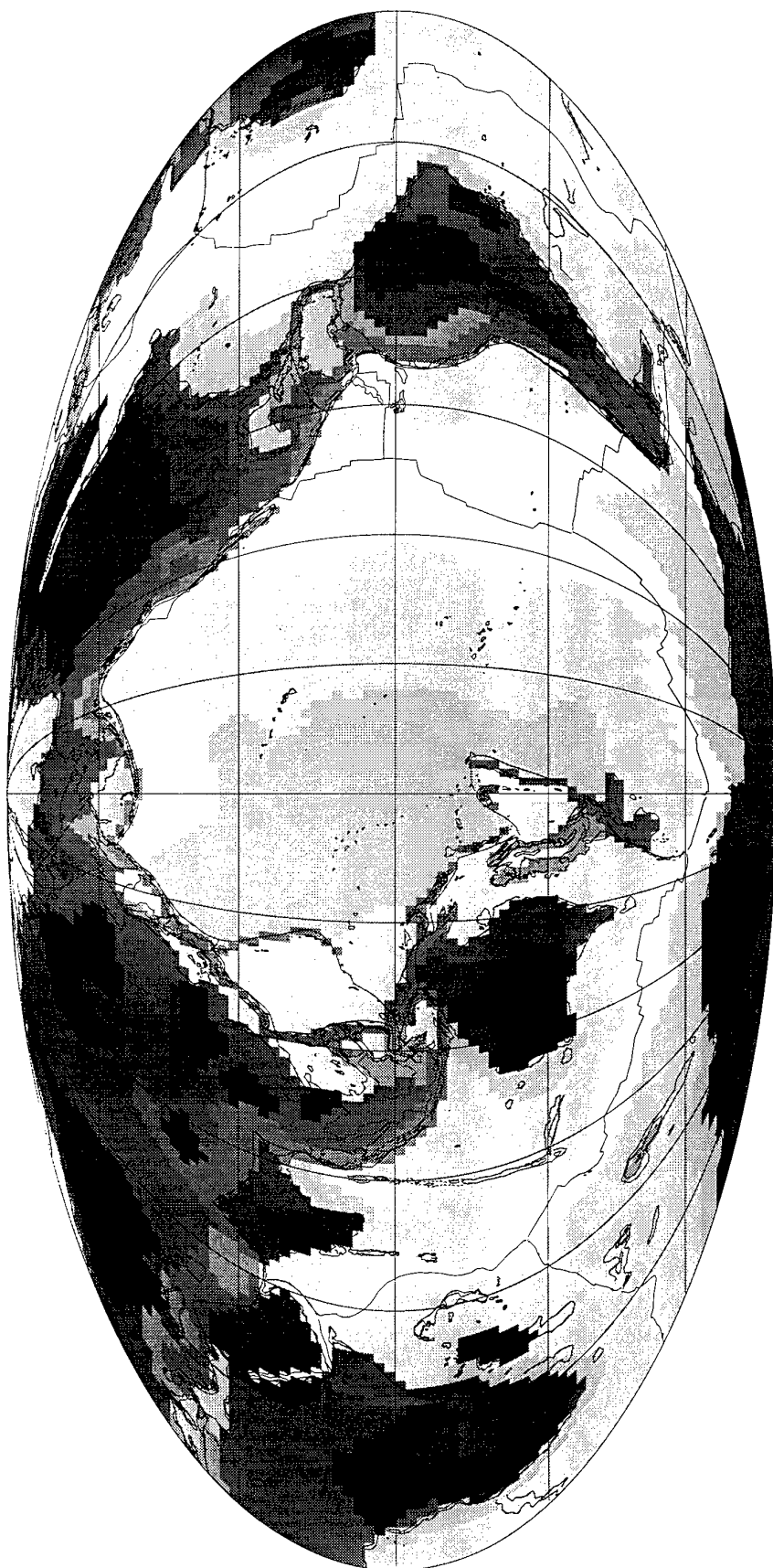
Figure 7. Station corrections for P-wave residuals after correction for the RUM model. White squares represent negative corrections (fast), black triangles represent positive corrections (slow). The symbol area is proportional to the amplitude of the correction with 1 second corrections given in legend for reference.

Table 1. Mean and variance reduction after the different steps of inversion/data reduction. Upper for P residuals, lower for S residuals.

Table 2. The RUM model as a percentile slowness perturbation relative to AK135. The labeling of the regions is as in Figure 5. Upper for compressional velocity, lower for shear velocity.

Table 3. Mislocation of explosions of known location after correction for the RUM model and the associated station corrections. Only teleseismic residuals were used.

Tectonic Regionalization



- Young ocean [< 25 Myrs]
- ▤ Intermediate ocean [25-100 Myrs]
- ▥ Old ocean [> 100 Myrs]
- Tectonic continent
- Young continent [< 250 Myrs]
- Intermediate continent [250-800 Myrs]
- Old continent [800-1700 Myrs]
- Ancient continent [> 1700 Myrs]

Figure 1

Figure 1 b)

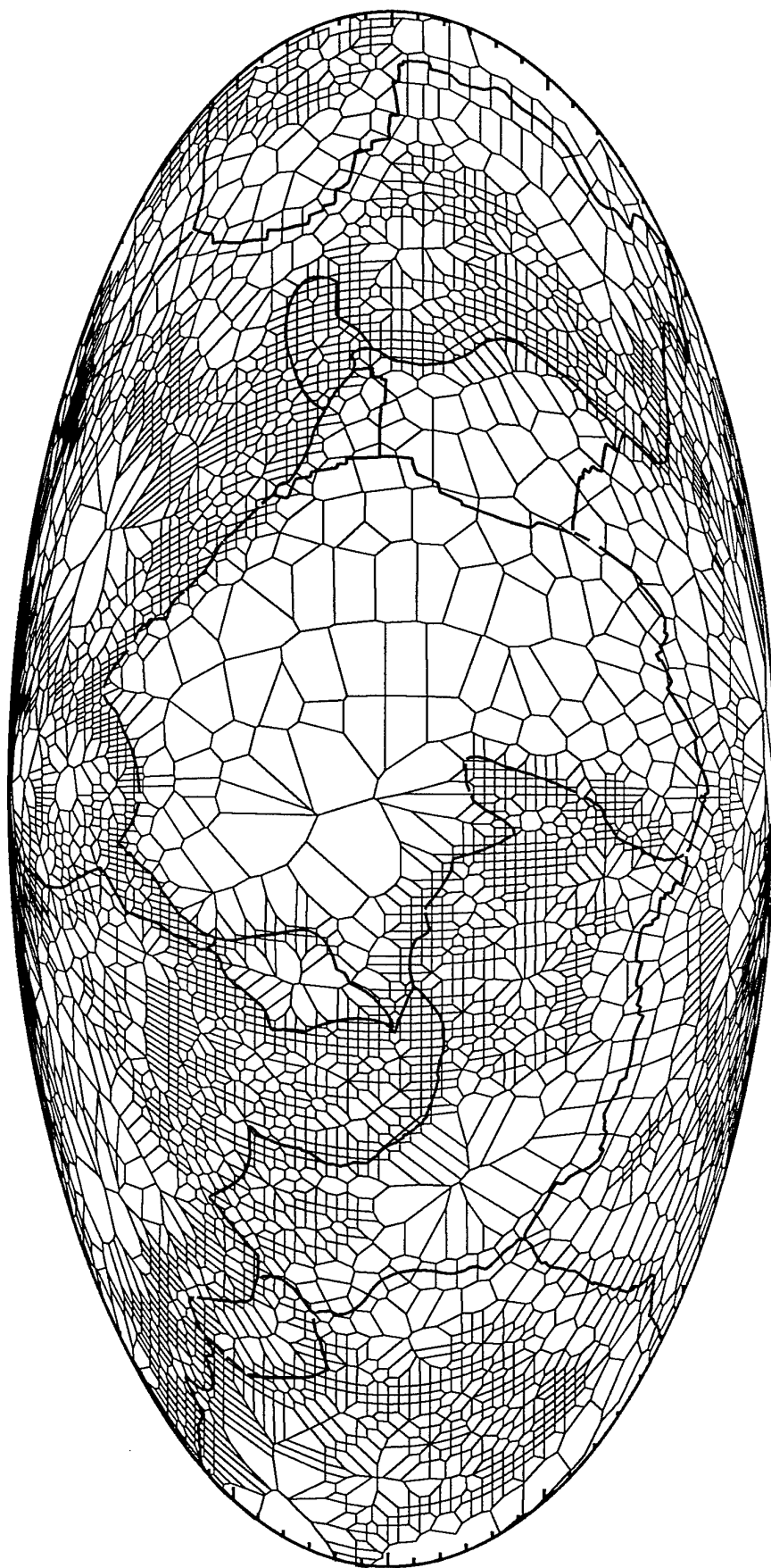


Figure 1 c)



Figure 2



Figure 2 b)

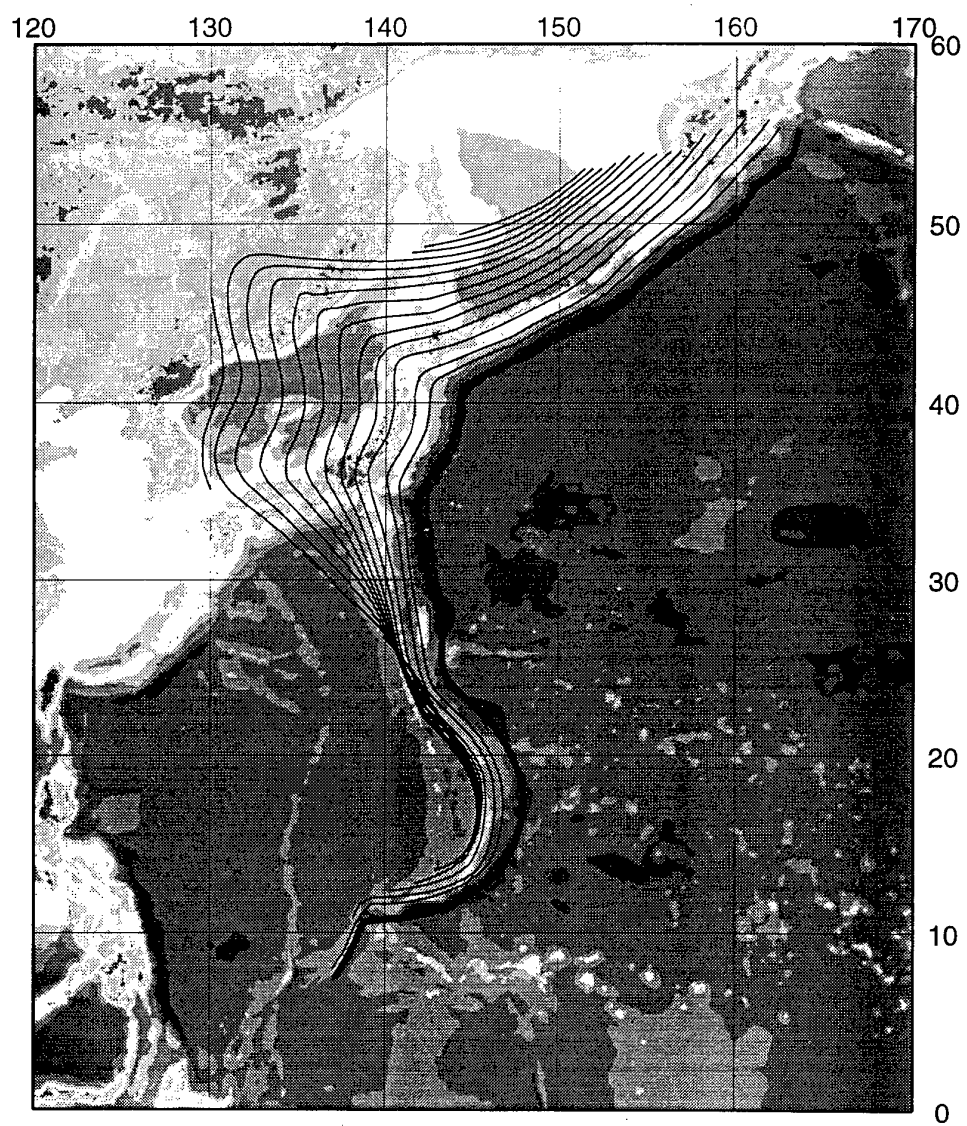


Figure 2 c)

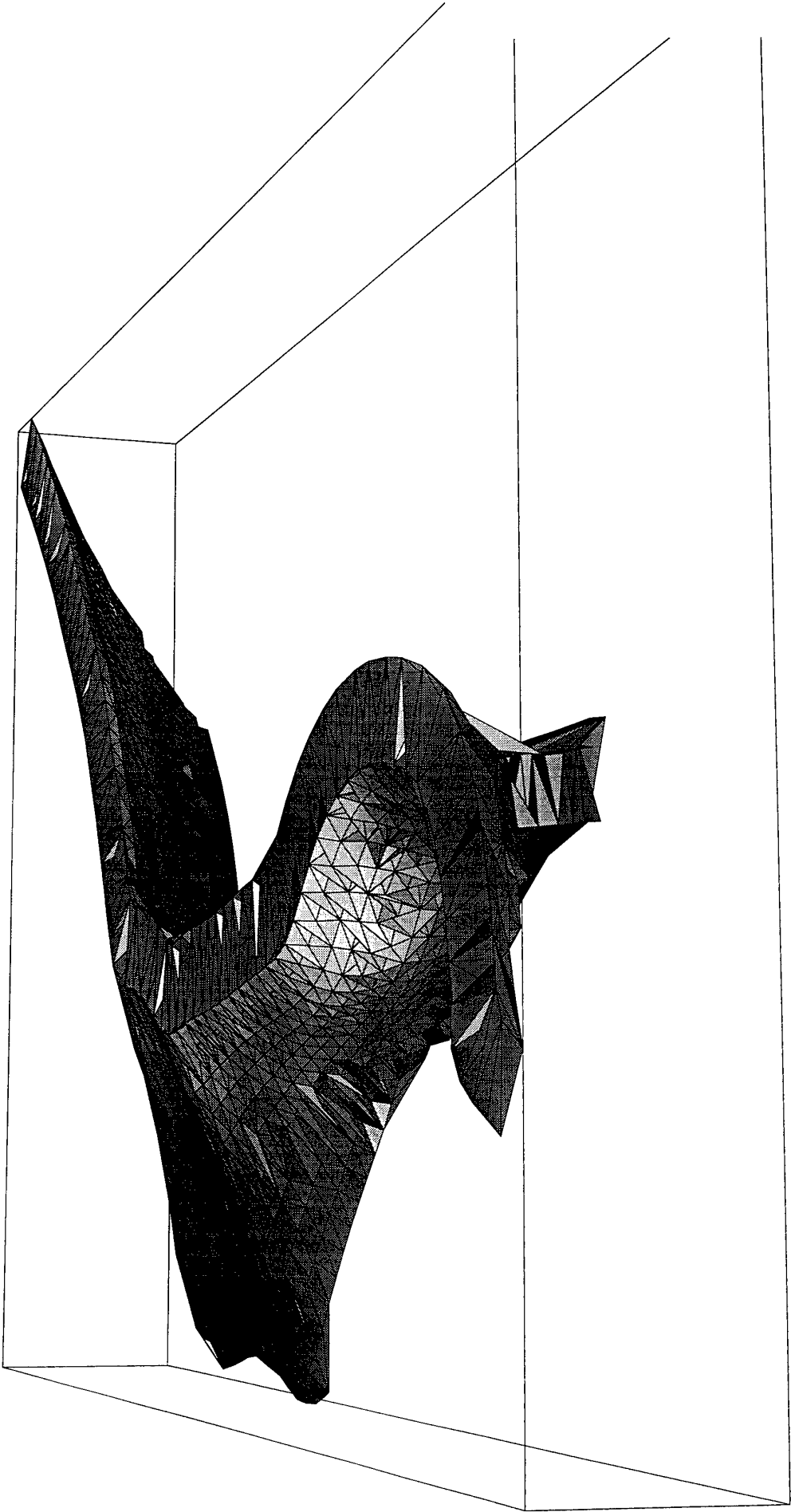
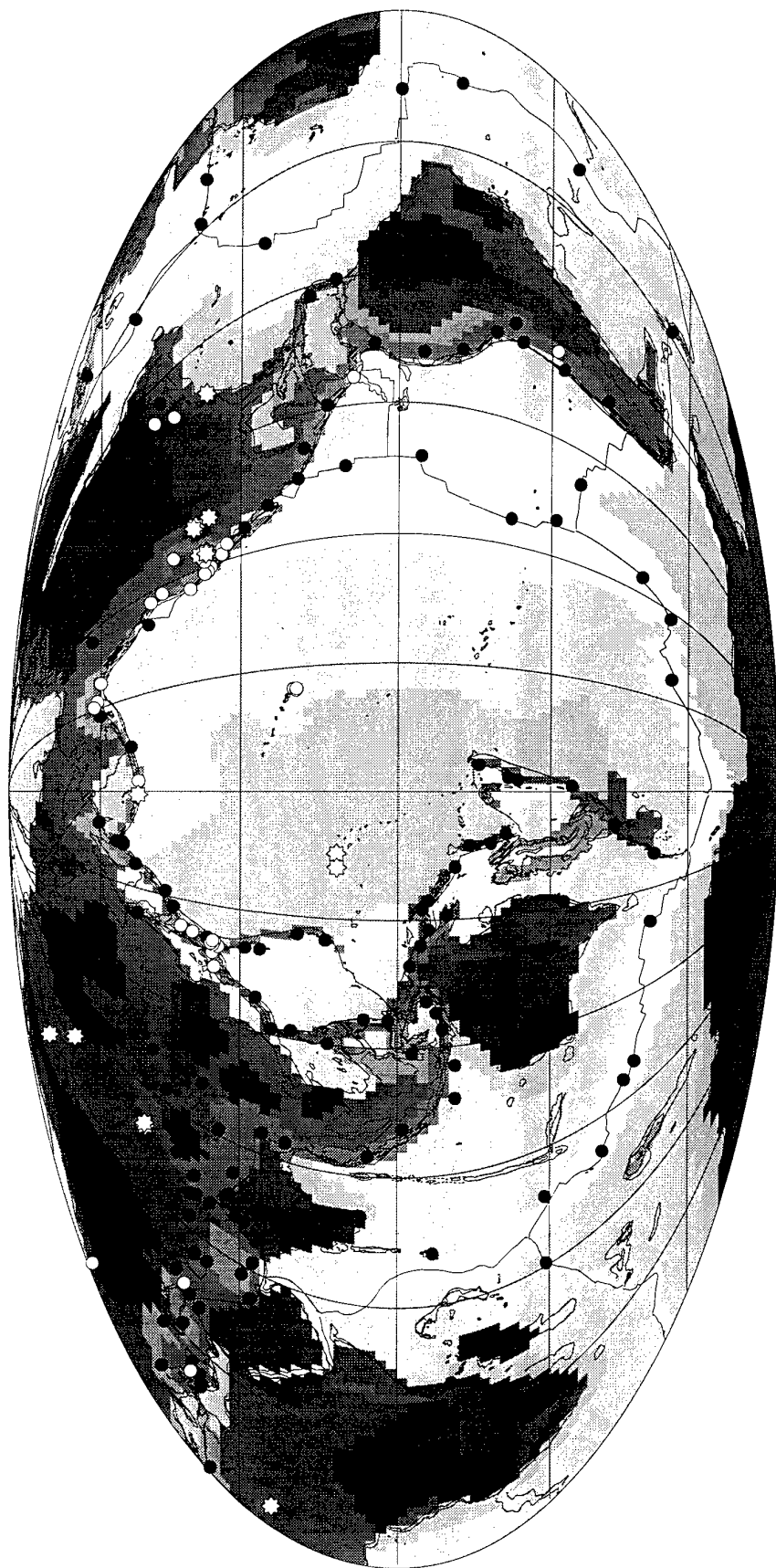


Figure 3



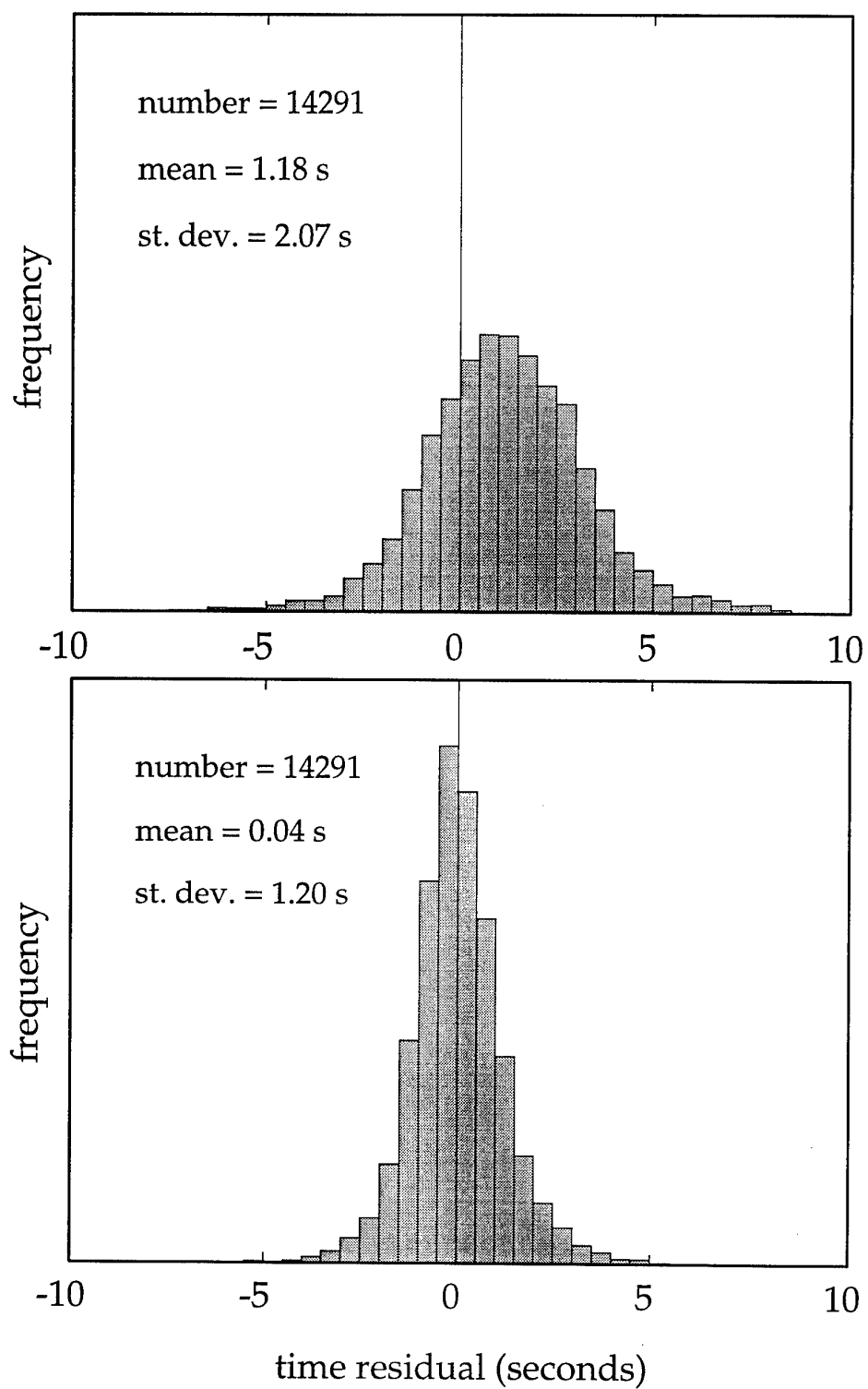


Figure 4 a)

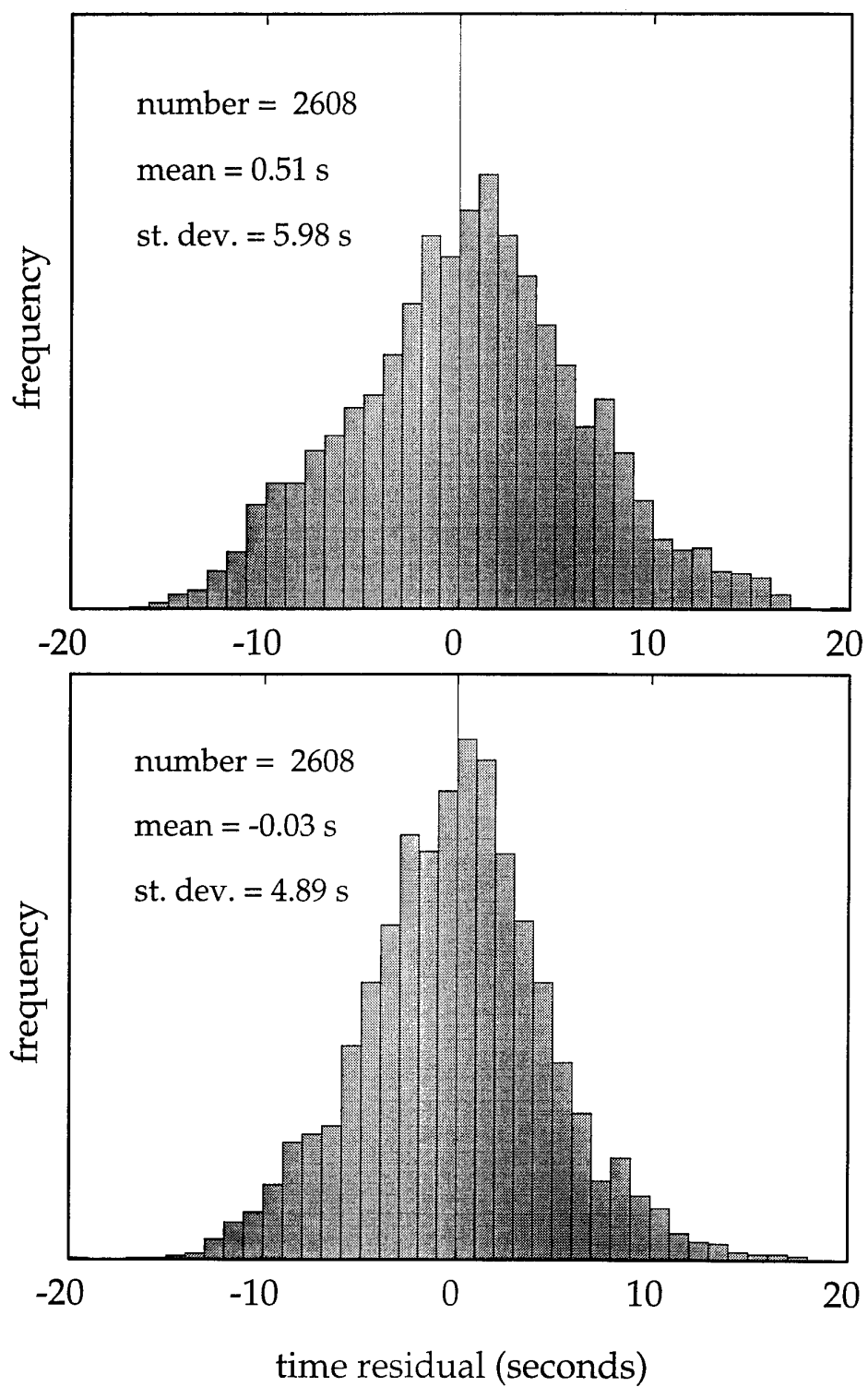
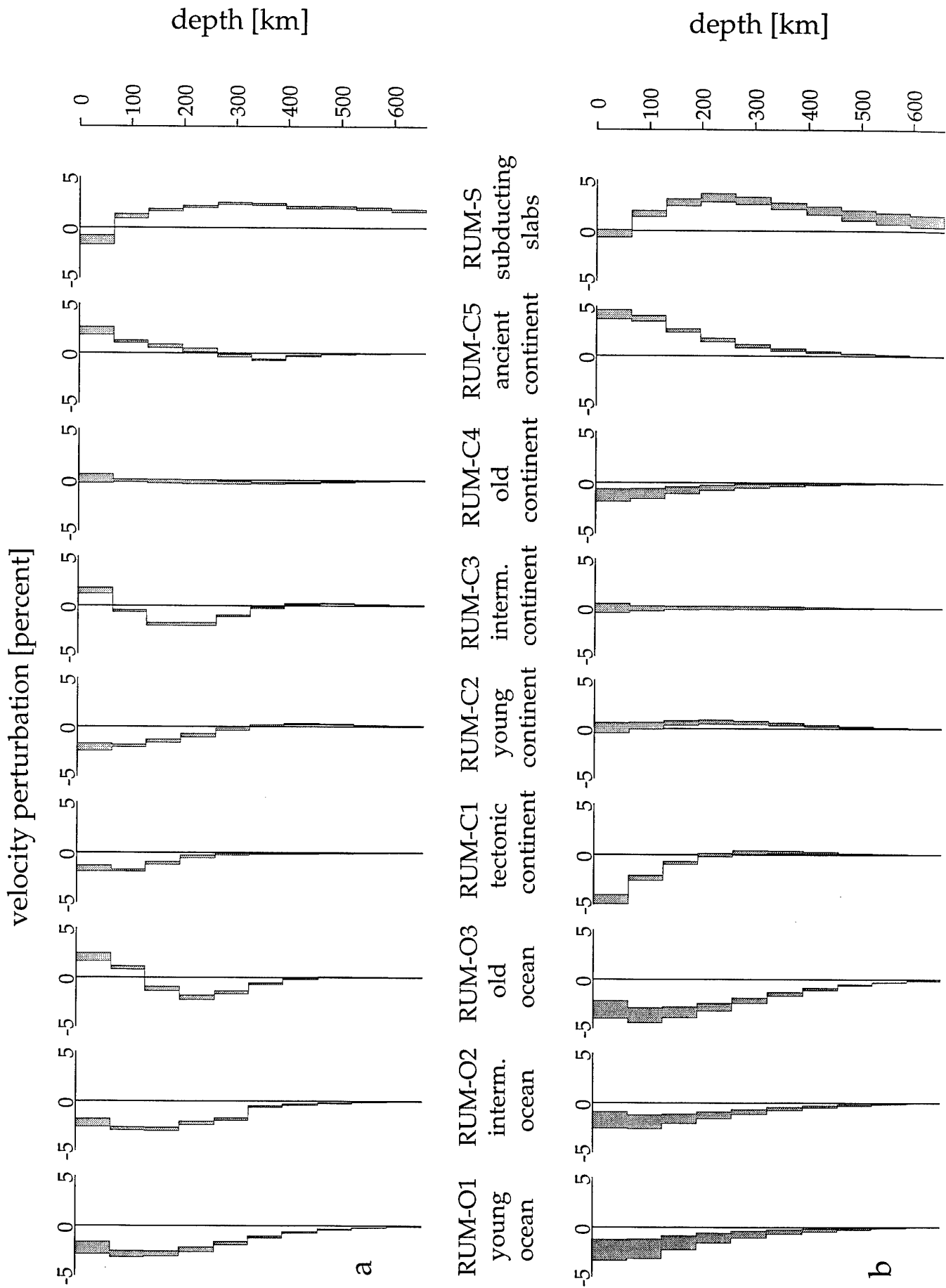


Figure 4 b)

Figure 5



RUM cross section [-150.0,56.67]

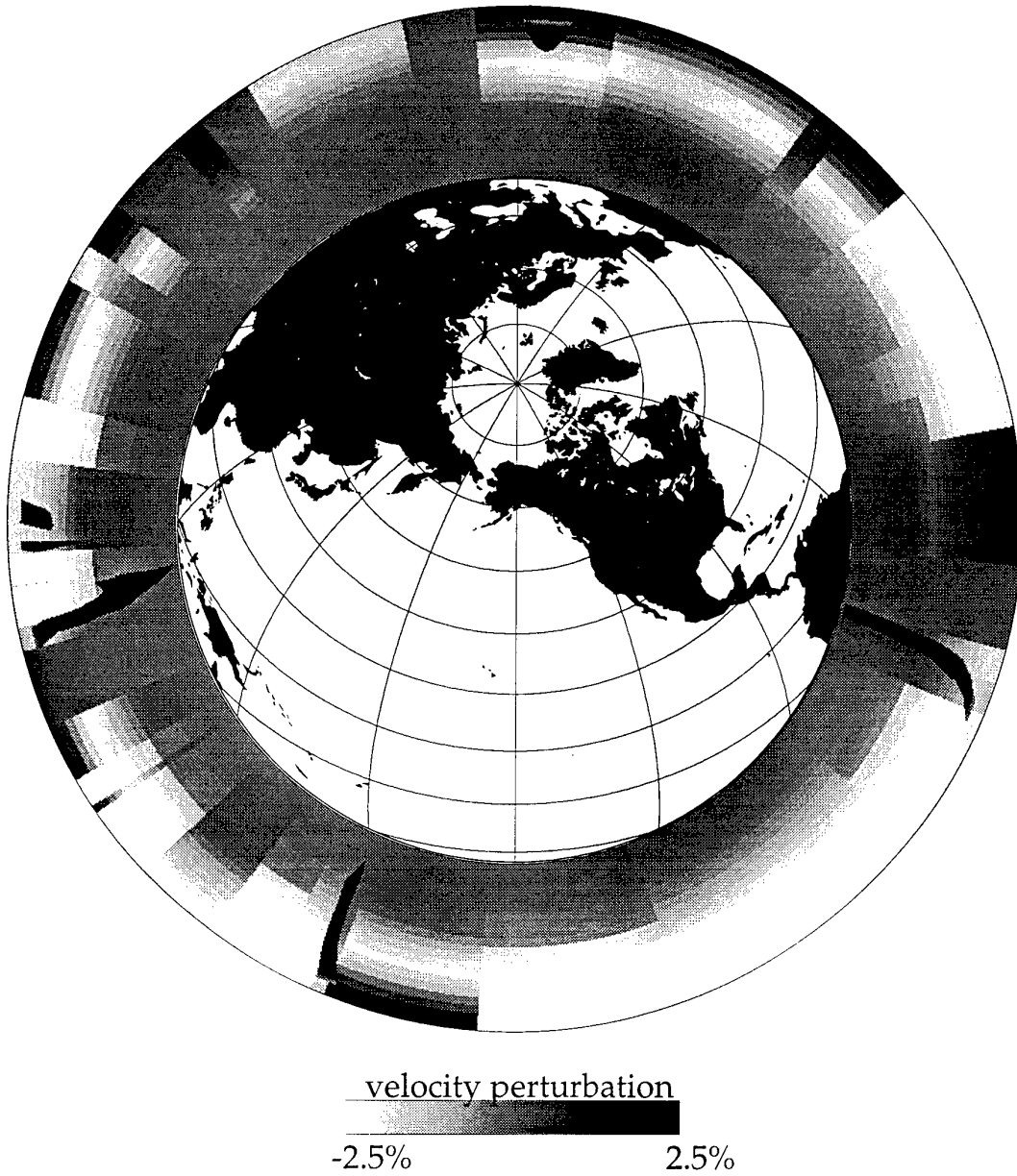


Figure 7

RUM cross section [-30.0,-17.85]

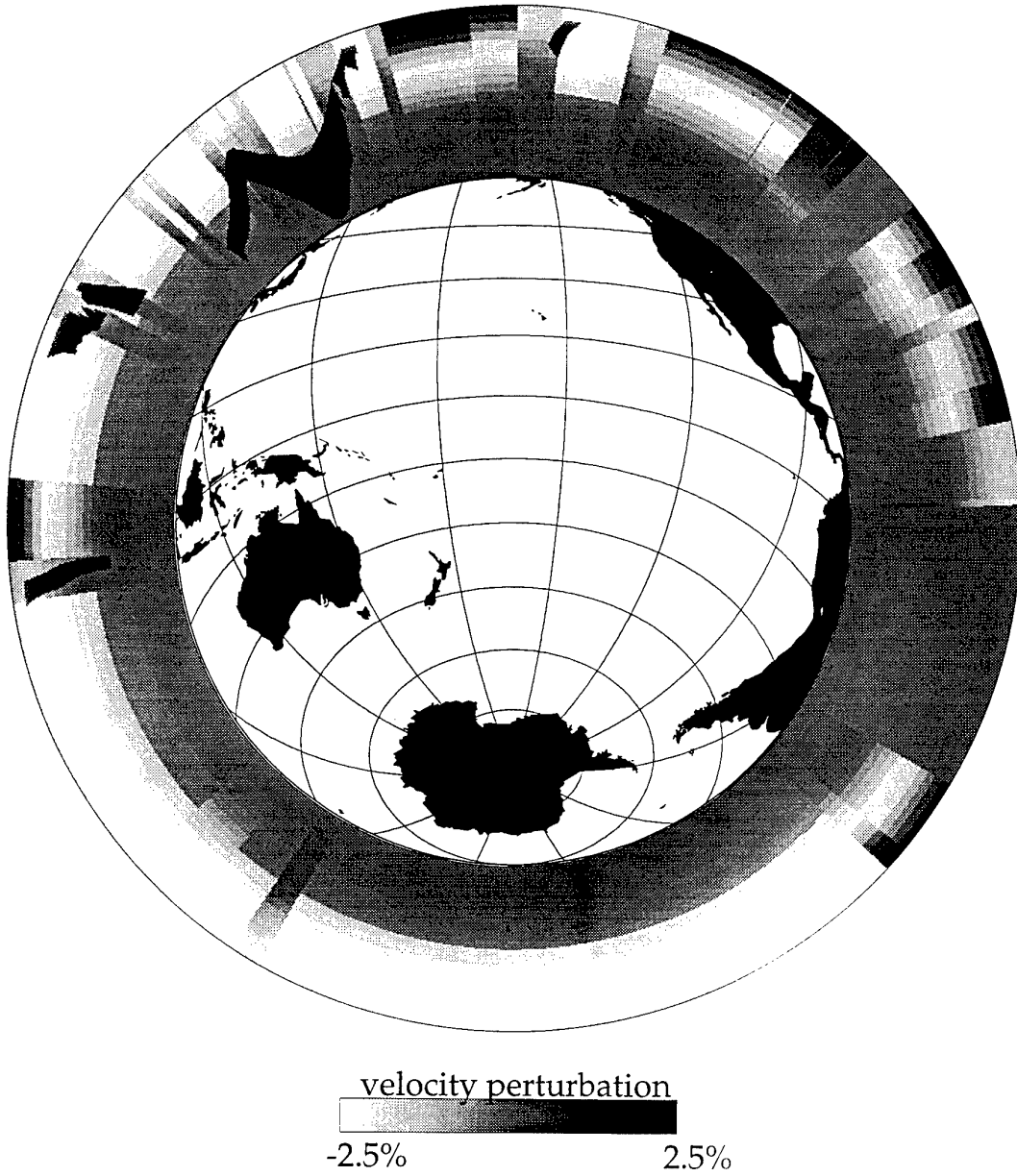


Figure 6 *b*

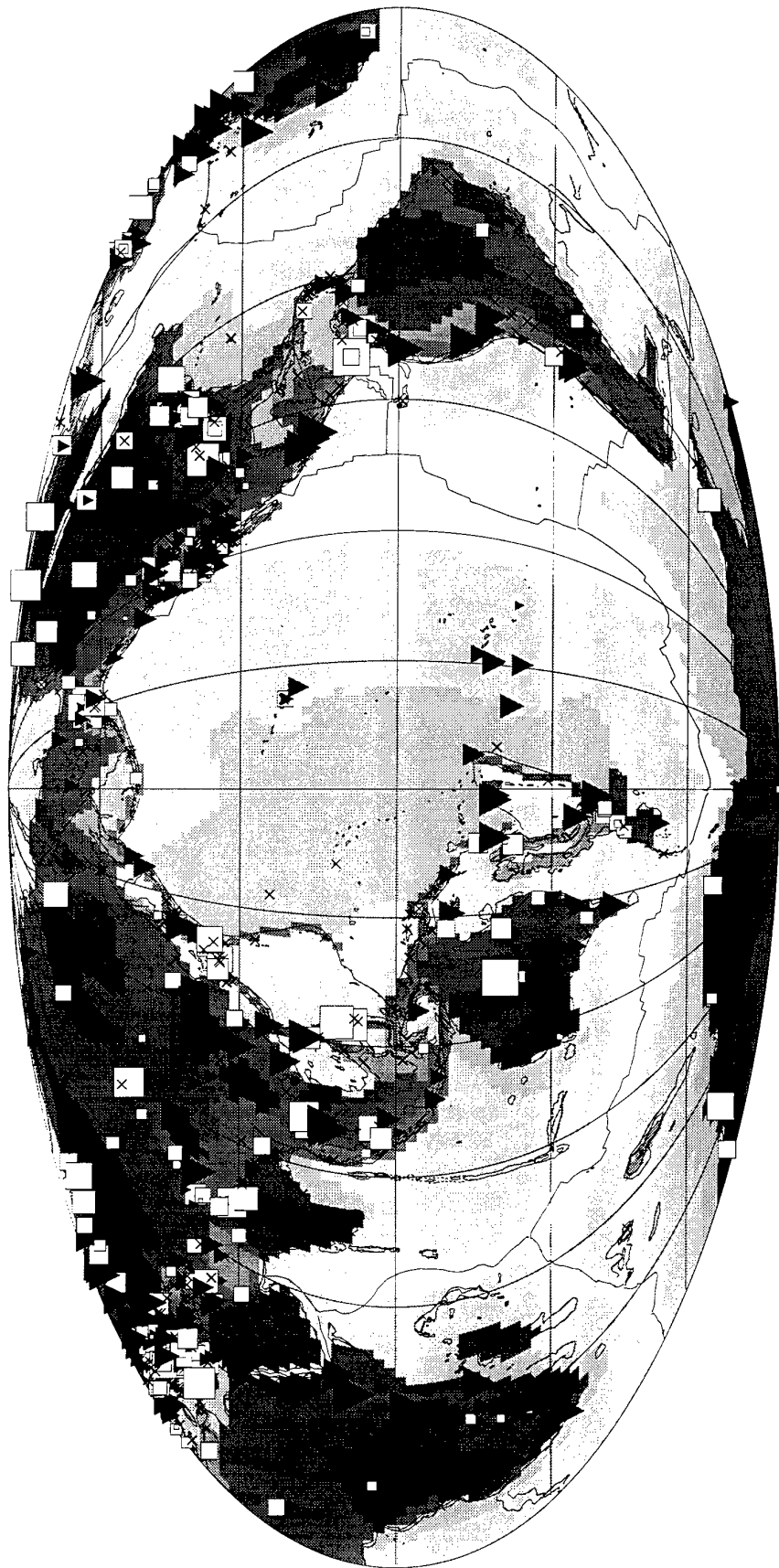


figure 7

	mean (s)	variance (s ²)	variance reduction
Initial - P residuals	1.18	4.30	
After relocation	0.69	1.99	54%
After velocity perturbation	0.19	1.71	14%
After station corrections	0.04	1.44	16%
Initial - S residuals	0.51	5.98	
After relocation	-0.17	5.48	16%
After velocity perturbation	0.01	5.19	10%
After station corrections	-0.03	4.89	11%

Table 1

depth (km)	RUM O1	RUM O2	RUM O3	RUM C1	RUM C2	RUM C3	RUM C4	RUM C5	RUM S
33	2.23	2.19	-2.03	2.08	1.58	-1.53	-0.14	-2.24	1.23
99	2.84	2.78	-0.96	1.94	1.77	0.54	0.07	-1.16	-1.12
165	2.81	2.84	1.14	1.45	1.04	1.91	0.13	-0.71	-1.73
231	2.41	2.23	2.04	0.89	0.42	1.90	0.17	-0.31	-2.06
297	1.76	1.84	1.52	0.27	0.17	1.05	0.26	0.25	-2.38
363	1.13	0.56	0.65	-0.13	0.11	0.20	0.29	0.65	-2.29
429	0.68	0.37	0.13	-0.27	0.09	-0.20	0.26	0.26	-2.00
495	0.38	0.22	-0.04	-0.23	0.06	-0.24	0.18	0.09	-2.01
561	0.20	0.12	-0.05	-0.14	0.04	-0.16	0.10	0.03	-1.89
627	0.10	0.06	-0.03	-0.07	0.02	-0.09	0.05	0.01	-1.70

depth (km)	RUM O1	RUM O2	RUM O3	RUM C1	RUM C2	RUM C3	RUM C4	RUM C5	RUM S
33	2.29	1.73	3.08	-0.08	4.46	-0.00	1.24	-4.15	0.29
99	2.18	1.93	3.65	-0.29	2.32	0.04	1.09	-3.75	-1.68
165	1.58	1.61	3.36	-0.57	0.82	-0.00	0.75	-2.55	-2.79
231	1.07	1.25	2.84	-0.68	0.03	-0.03	0.50	-1.61	-3.25
297	0.71	0.91	2.17	-0.60	-0.25	-0.04	0.32	-1.00	-2.96
363	0.46	0.62	1.51	-0.45	-0.26	-0.03	0.21	-0.63	-2.44
429	0.30	0.40	0.99	-0.30	-0.18	-0.02	0.13	-0.40	-2.00
495	0.17	0.24	0.58	-0.18	-0.11	-0.01	0.08	-0.23	-1.54
561	0.09	0.13	0.32	-0.10	-0.06	-0.01	0.04	-0.13	-1.23
627	0.05	0.06	0.16	-0.05	-0.03	-0.00	0.02	-0.06	-0.98

Table 2

	AK135		AK135 + RUM		AK135 + RUM + st. corr.	
	σ_t s	σ_h km	σ_t s	σ_h km	σ_t s	σ_h km
Castle Bravo	-0.13	14.03	0.48	11.85	0.40	10.85
Castle Yankee	-0.22	9.43	0.42	6.84	0.36	5.28
Oak	-0.10	8.27	0.45	6.04	0.46	4.71
Bilby	-0.18	6.20	0.78	5.54	0.75	5.93
Sahara 20/10 '63	-0.07	8.72	0.35	9.19	0.73	5.89
Sahara 27/02 '65	-0.27	11.09	0.10	10.61	0.61	5.12
Chase	-1.11	8.41	-0.46	4.29	-0.39	1.55
Commodore	-0.90	16.18	0.16	9.39	0.34	4.75
Gasbuggy	-0.81	2.79	-0.56	1.67	-0.54	4.06
Faultless	-0.58	9.48	0.46	3.33	0.59	6.03
Boxcar	-0.49	8.46	0.52	2.75	0.65	4.84
Rulison	-0.86	13.32	-0.53	15.19	-0.24	6.22
Kazakh 30/11 '69	0.78	7.59	1.14	8.10	1.04	2.39
Kazakh 25/04 '71	0.55	10.72	0.90	11.18	0.80	5.53
Cannikin	1.55	22.32	1.88	14.28	1.90	11.60
Kazakh 16/08 '72	0.85	11.79	1.21	12.06	0.89	4.72
Kazakh 02/11 '72	0.79	9.71	1.11	9.49	1.25	3.86
Rio Blanco	-0.60	9.24	-0.26	11.19	-0.31	8.80
Alamo	-0.59	11.73	0.34	5.33	0.38	6.21
RMS	0.71	11.23	0.77	9.16	0.77	6.19

Table 3